Lattice-Boltzman simulation of viscoelastic contact lines

Hulikal Chakrapani, T.

Award date:
2017

Lattice-Boltzmann simulation of viscoelastic contact lines

T.HULIKAL CHAKRAPANI
0979294

A thesis presented for the degree of
Master of Science
In
Applied Physics

Under supervision of:
Prof.dr. F.Toschi
Prof.dr. J.H.Snoeijer

August 2, 2017

Turbulence and Vortex Dynamics
Department of Applied Physics
Eindhoven University of Technology

Contents

Nomenclature

$\boldsymbol{g}_\xi$	Total force experienced by a component ξ [lbu]
$\boldsymbol{n}_s$	Normal vector at the interface
$\boldsymbol{t}_s$	Tangential vector at the interface
χ	Viscosity ratio
Δt	Lattice Boltzmann time step [lbu]
Δ	Smoothing parameter [lbu]
$\dot{\epsilon}$	Elongational rate
$\dot{\gamma}$	Shear rate $[\frac{1}{\mathrm{s}}]$
η	Dynamic viscosity $[\frac{\mathrm{kg}}{\mathrm{ms}}]$
η_P	Polymeric viscosity [lbu]
γ	Surface tension $[\frac{\mathrm{kg}}{\mathrm{s}^2}]$
κ	Curvature $[\frac{1}{\mathrm{m}}]$
Λ	Non dimensional shear rate
Λ_e	Non dimensional elongation rate
λ_s	Scale separation parameter
$\boldsymbol{\mathcal{R}}$	Director vector from one bead to another bead in a FENE-P model
$\mathcal{D}$	Steady state deformation of a viscoelastic (Newtonian) droplet inside a Newtonian (viscoelastic) matrix
$\mathcal{G}$	Interaction parameter controlling the strength of interaction between the components of a multicomponent system [lbu]
$\mathcal{N}$	First normal stress difference $[\frac{\mathrm{kg}}{\mathrm{ms}^2}]$
$\mathcal{S}$	Polymeric shear stress in the fluid $[\frac{\mathrm{kg}}{\mathrm{ms}^2}]$
ν	Kinematic viscosity $[\frac{\mathrm{m}^2}{\mathrm{s}}]$
ϕ	Wedge angle in Huh-Scriven model
Ψ_1	Normal stress coefficient
ρ	Density of a LB fluid [lbu]
τ	BGK collision time [lbu]
τ	Relaxation time [s]

τ_P Polymer relaxation time [lbu]

$\underline{\underline{\boldsymbol{\sigma}}}_P$ Polymeric stress tensor

$\underline{\underline{\boldsymbol{C}}}$ Polymer conformation tensor

$\underline{\underline{\boldsymbol{P}}}$ Total pressure tensor of a LB fluid [lbu]

θ Steady state orientation angle of a viscoelastic (Newtonian) droplet inside a Newtonian (viscoelastic) matrix

θ_{ap} Dynamic contact angle [rad]

$\theta_{\mathrm{m},A}$ Microscopic wetting angle for Fluid A at the bottom wall in the Couette flow geometry [rad]

$\theta_{\mathrm{m},B}$ Microscopic wetting angle for Fluid B at the top wall in the Couette flow geometry [rad]

θ_{M} Dynamic contact angle measured at the center of the Couette flow geometry [rad]

θ_{m} Microscopic wetting angle [rad]

ξ An index to represent the components of a multicomponent system

a Major axis of a viscoelastic (Newtonian) droplet inside a Newtonian (viscoelastic) matrix

b Minor axis of a viscoelastic (Newtonian) droplet inside a Newtonian (viscoelastic) matrix

c_i Lattice speed in the i^{th} direction [lbu]

c_s Lattice speed of sound [lbu]

Ca Capillary number

Ca_{cr} Critical capillary number

$d\dot{E}$ Differential viscous dissipation $[\frac{\mathrm{kgm}}{\mathrm{s}^3}]$

De Deborah number

ds Arc length parameter $[\mathrm{m}]$

$f(r_P)$ Potential of the spring connecting two beads in a FENE-P model

f_i Single particle distribution function in the i^{th} direction [lbu]

f_i^{eq} Equilibrium single particle distribution function in the i^{th} direction [lbu]

G'' Loss modulus of a viscoelastic material

G' Storage modulus of a viscoelastic material

H Distance between top and bottom walls in Couette flow geometry $[\mathrm{m}]$

$h(x)$ or $y(x)$ Interface profile

k Spring constant in the spring-dashpot model $[\frac{\mathrm{kg}}{\mathrm{s}^2}]$

L^2 Maximum extensible length of a FENE-P polymer [lbu]

L_f Typical flow length scale [m]

l_s Slip length $[\mathrm{m}]$

p Pressure field $[\frac{\mathrm{kg}}{\mathrm{ms}^2}]$

R Effective radius of a viscoelastic (Newtonian) droplet inside a Newtonian (viscoelastic) matrix

U	Velocity scale [$\frac{\mathrm{m}}{\mathrm{s}}$]
$u(x, y)$	Velocity field [$\frac{\mathrm{m}}{\mathrm{s}}$]
w_i	Lattice weight for the i^{th} direction [lbu]
Wi	Weissenberg number
$\mathcal{G}_{\mathrm{wall},\xi}$	Interaction parameter between a fluid component and wall nodes [lbu]
lbu	Lattice Boltzmann units

Chapter 1

Introduction

1.1 Background & Motivation

Lot of instances arise where the interface between solid, liquid, and vapor co-exist, for example: a water droplet resting on a solid surface. The interface along which the solid, liquid and vapor phases co-exist is referred to as the three phase contact line, or just contact line. Based on their state of motion the contact lines can be classified into (a) static and (b) dynamic contact lines. The example of a stationary droplet resting on top of a solid constitutes a static contact line.

Moving contact lines are ubiquitous in nature. A closer look at our surroundings will reveal several instances of moving contact lines. For instance, drops sliding on/off a window pane is a typical example of a moving contact line, see Figure (1.1). Apart from its ubiquitous appearance in nature, the physics near a contact line is rich, and, it is multiscale in nature. For example, the macroscopic splash patterns vary significantly when two balls having distinct surface textures impact a pool of liquid. As shown in Figure (1.2), the macroscopic splash due a hydrophobic ball, whose surface is covered by a nanometric coating, is significantly different when compared to the splash caused due to a hydrophilic ball [1]. The hydrophilic and the hydrophobic balls differ only in their micropscopic wettability towards the liquid. Through aforementioned example illustrates that the *hydrodynamics* at the smallest scales affect the flow characteristics at a much larger scale.

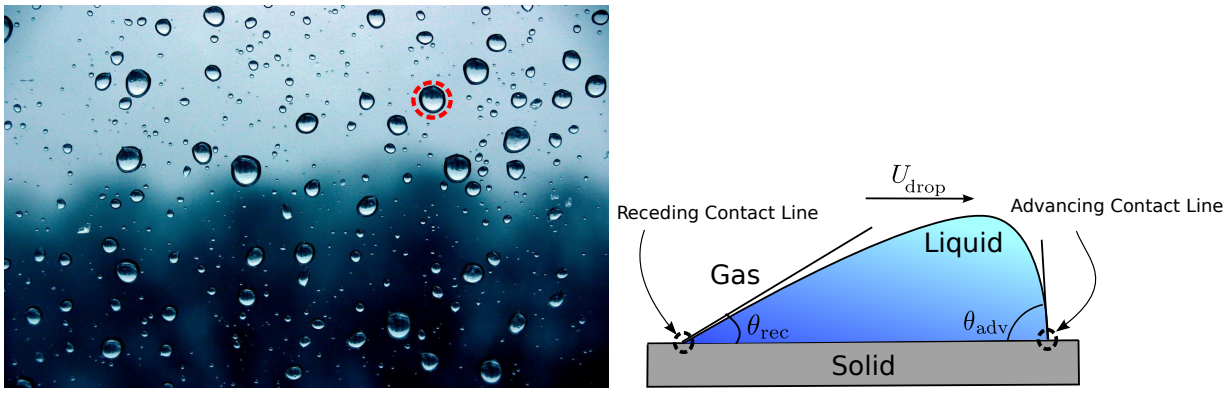

(a) Rain drops on a window pane

(b) Schematic of a sliding rain droplet

Figure 1.1: Figure (a) shows a photograph capturing the sliding of rain drops on a window pane (the figure has been taken from *https://www.shutterstock.com*. The droplet highlighted using red dotted lines is schematically represented in (b). The window pane is represented as a solid and the liquid droplet is moving on the solid with a velocity U_{drop}. The moving droplet constitutes an advancing and a receding contact line, as highlighted in the figure. The apparent contact angle at the *advancing* end and at the *receding* end of the droplet is different and is given by the value: θ_{adv} and θ_{rec}.

For a long time the research efforts have been focused on understanding static situations. However, the interest in moving (dynamic) contact lines has significantly increased over the years because it caters to a

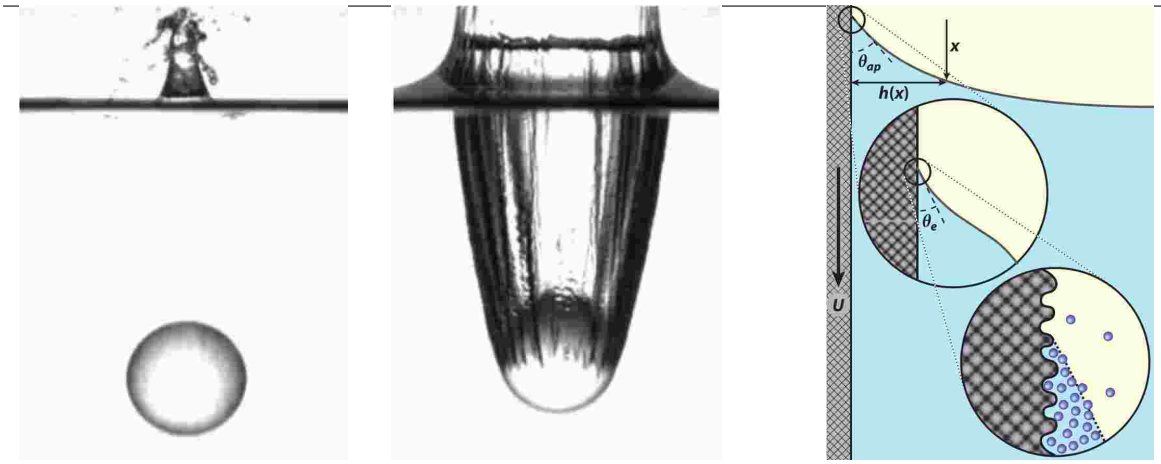

(a) Hydrophilic (b) Hydrophobic (c) Advancing contact line

Figure 1.2: Impacting of spheres on a water surface for two kinds of sphere surfaces is shown:(a) hydrophilic, (b) hydrophobic. In (c) the multiscale nature of a moving contact line problem is depicted by an advancing contact line. The presence of an apparent dynamic contact angle is represented by the symbol θ_{ap}. On further zooming into the contact line region the equilibrium or the static contact angle is represented by the symbol θ_e. Finally, on the smallest length scales of less than $10\mathrm{nm}$, the molecular picture of the fluid becomes important. Figures (a), (b), (c) are adopted from [2].

wide range of industrial applications. For instance, coating industries are interested in understanding and controlling the thickness of adhesives or paints deposited on substrates [3–5]. Industries related to immersion lithography use water as a lens to achieve higher optical resolutions when focusing light on substrates [6, 7]. The typical questions that arise while understanding the moving contact line problem are: (a) what is the critical velocity U_{cr} attainable before which one fluid is entrained or engulfed into the other fluid?, (b) what are the physical mechanisms responsible for such an entrainment?, (c) how does U_{cr} respond to minute changes in physical parameters like viscosity and surface tension?.

Traditionally, scientific communities have invested and devoted efforts to investigate the contact line problem for the case of Newtonian liquids. Through this effort, it is a well established that high magnitudes of shear rates are established near a contact line. On the other hand, a certain type of fluids called non-Newtonian fluids are known to exhibit strange and fascinating phenomena when subjected to normal flow conditions. A typical example of this is the **rod climbing effect**, also called the **Weissenberg effect**, see Figure (1.3a). In addition, a daily life experience with a ketchup bottle can tell us that the ketchup is easily dispensed from the plastic container when subjected to shaking of the bottle. Or, when dealing with paints, it is seen that when a roller is used to apply paint on the wall the paint "flows easily" and allows a uniform application on the wall. This effect is called the **shear thinning effect**, see Figure (1.3b), where the effective viscosity of the fluid decreases in response to stresses. Interestingly, these effects are manifested in these fluids mainly due to the presence of polymers or particles inside these fluids. In fact, the responses stated above: (a) **rod-climbing effect**, (b) **shear-thinning effect** mainly arise due to the response of these polymers to shear stresses and shear rates.

Therefore, juxtaposing the above two phenomenon: (a) notoriously high shear rates near the contact line, (b) exhibition of shear rate dependent phenomenon in non-Newtonian fluids like the rod-climbing and the shear thinning effect, gives rise to the problem of *non-Newtonian contact lines*. The typical questions that arise in such a scenario are the following: (a) how do the notoriously high shear rates near the contact line affect the polymers or particles in the fluid , and as a feedback, (b) how do the stretched or elongated polymers affect the motion of fluid close to the contact line?

The number of articles addressing the problem of moving contact lines for the case of non-Newtonian fluids have investigated two aspects. The first aspect is the effect of viscoelasticity on the contact line motion, and, the second aspect is the influence of shear thinning on the contact line motion. The approach and efforts to investigate these two aspects have been through experimental, theoretical and numerical simulations. Spaid and Homsy [8–10] investigated the influence of viscoelasticity on the moving contact line problem encountered

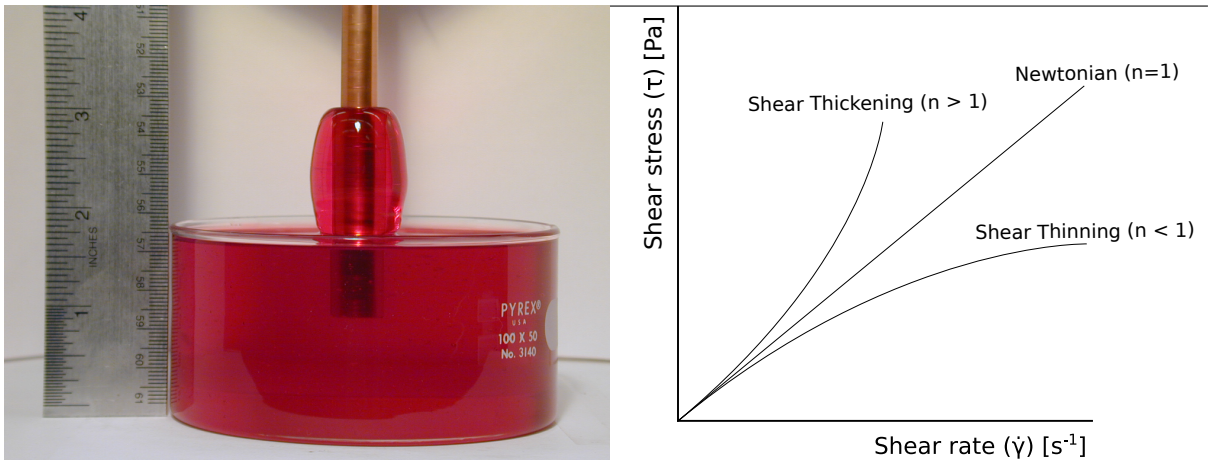

(a) Rod Climbing (b) Shear Thinning

Figure 1.3: (a) In this figure a rod is rotated with its end immersed inside the polymeric solute inside a Newtonian solvent. In the case of a Newtonian fluid the inertia would dominate and the fluid would move to the edges of the container,away from the rod. Here however the elastic forces generated by the rotation of the rod (and the consequent stretching of the polymer chains) result in a positive normal force and hence the fluid rises up the rod. The figure has been adopted from *https://http://web.mit.edu/nnf/research/phenomena/rod_climb _highres.jpg* (b) The typical shear stress σ in a non-Newtonian fluid as a function of the applied shear rate $\dot{\gamma}$ is shown. Shear thinning fluids are compared against Newtonian fluids and shear thickening.

during the process of spin coating using viscoelastic fluids, both experimentally and theoretically. Y. Wei *et al.* [11] investigated the viscoelastic aspects of contact line motion in viscous Newtonian and non-Newtonian liquids. In a subsequent paper they experimentally and theoretically investigated the influence of shear thinning on the moving contact line problem [12]. The contact line problem in the case non-Newtonian fluids has also been addressed through other interesting phenomena. Boudaoud theoretically investigated the normal stress effects on the dynamics of thin films on a horizontal solid substrate [13]. The framework was applied to the motion of an advancing contact line. Further, Rafai *et al.* [14] studied the spreading of non-Newtonian fluids on hydrophilic surfaces focusing on both: (a) normal stresses (viscoelasticity) and (b) shear thinning. In another interesting experiment on the dynamics of non-Newtonian droplets , Bartolo *et al.* [15] studied the spectacular rebound of non-Newtonian droplets and quantified the rebound velocity by calculating the normal stresses generated near the contact line.

In this thesis we wish to resolve the flow near a contact line for non-Newtonian fluids using numerical simulations. This can provide new insights regarding the magnitudes of the polymeric stresses stresses during the course of an experiment. In addition, resolving the flow features associated with the experiment can provide additional insight into the problem and can help in a better correlation of observations with a given hypothesis. Therefore, in this thesis, we aim to observe and understand the influence of viscoelasticity on a moving contact line using the lattice Boltzmann method coupled with finite difference equations to solve for dynamics of the polymers. To study this we adopt a simple Couette flow geometry in a multi-component simulation setup.

1.2 Thesis outline

The thesis is organized as follows:
In **Chapter 2**, the relevant theory for understanding the contact line motion is presented. The famous Huh-Scriven model is introduced and the assumptions leading to the hydrodynamic singularities are identified. Following this, the Cox-Voinov law is introduced which alleviates the singularities in the stress and pressure fields. Further, the geometry relevant to this thesis: the Couette-Flow geometry is explained along with the pertinent equations, boundary conditions and the non-dimensional numbers. A basic result is provided to qualitatively understand the model parameters. The non-Newtonian aspect of a fluid is introduced through

the Maxwell model and the emergence of an intrinsic time scale, τ, is identified. Typical non-Newtonian effects like the normal stress effects, responsible for the rod-climbing, and shear thinning effects are introduced. The chapter is concluded by relating the aforementioned non-Newtonian effects in the perspective of a contact line problem, through the non-dimensional Wiessenberg number.

In **Chapter 3**, the numerical aspects of the lattice Boltzmann formalism is discussed. The Boltzmann equation is introduced and the discretized form of the equation is presented. The types of lattice on which the equation is solved is briefly explained. The relevant boundary conditions applicable to the contact line problem are mentioned. Following this, the multicomponent formalism in lattice Boltzmann method using the *Shan-Chen* interaction force is discussed, and, the methodology to calculate the surface tension and the contact angle is discussed. Further, we discuss the FENE-P model to introduce the non-Newtonian rheology into the lattice Boltzmann formalism. Different aspects of the model like the conformation tensor and the polymeric stresses are introduced. The numerical implementation of the evolution of the conformation tensor of the polymer is discussed. Finally, we briefly the technical aspects of multicomponent viscoelastic simulations.

In **Chapter 4**, various validation cases performed for the non-Newtonian rheology are presented and the important parameters from the FENE-P model are identified. Following this, the contact line problem is discussed. Firstly, the Newtonian contact line is simulated and validated against theoretical results obtained for the Couette-flow geometry, for a given set of non-dimensional parameters. Further, the problem of the non-Newtonian contact line is discussed for two cases: (a) symmetric wetting, (b) asymmetric wetting. The observations are discussed.

Finally, in **Chapter 5**, we conclude by discussing the observations.

Chapter 2

Theoretical Background

In this chapter the necessary theoretical background for studying moving contact lines in non-Newtonian fluids is discussed. We begin by describing the Huh-Scriven model in which the moving contact line is addressed for two immiscible fluids separated by a planar interface satisfying the no-slip boundary condition. We discuss that even though such a model can reasonably describe well the velocity fields close to the contact line, diverging stresses arise when approaching the contact line due to the no-slip condition. Therefore, a microscopic regularizing mechanism like the (a) slip length or the (b) diffuse interface is required to avoid this singularity. An improvement of the Huh-Scriven model which takes into account the slip length as well as the actual shape of the interface close to the moving contact line is the Cox-Voinov model. We briefly describe the features of the Cox-Voinov model which identifies Ca as an important non-dimensional parameter close to the contact line. Further, in this thesis, we adopt the Couette flow geometry to study the moving contact line problem. Therefore, we describe the Couette flow geometry and recognize the important parameters for studying the moving contact line problem, as identified by the Cox-Voinov model. We then argue that to study the moving contact line for a non-Newtonian fluid we need to consider the polymer relaxation as an important parameter. Hence, an additional non-dimensional parameter called the Weissenber number Wi needs to be introduced. We conclude the chapter by discussing the two non-Newtonian features that are important close to the moving contact line, namely the first normal stress difference $\mathcal{N}$ and the polymeric shear stress $\mathcal{S}$, both of which depend on the shear rate.

2.1 The moving contact line problem - a closer look

2.1.1 Huh-Scriven Problem

The initial modeling of the hydrodynamics near a moving contact line was addressed by Huh and Scriven [16]. The contact line was modeled for liquid and vapor separated by a moving and planar interface profile, see Figure (2.1). The model solved for exact expressions of the velocity field under conditions of mass conservation, momentum conservation, continuity of the shear stresses at the interface between the two phases, and, most importantly, the **no-slip boundary condition** at the wall. Typical velocity fields for various wedge angles ϕ, are visualized in Figure (2.2) [16]. It can be seen from the figure that as the wedge angle ϕ is reduced the velocity vectors have to negotiate turns within smaller heights $h(x)$.

It can be seen that as the distance to the wedge tip r tends to 0, the velocity vectors will have to negotiate *extremely* sharp turns near the contact line. Viscous stresses (σ_{xy}) and the differential energy dissipation ($d\dot{E}$) which can be expressed by the scaling relations $\sigma_{xy} \sim \frac{\eta U}{r}$ and $d\dot{E} \sim \eta U^2 \frac{dr}{r}$ will diverge close to the contact line as $r \to 0$ [2]. The implication of this diverging stress field is that the force required to pull a plate out of a liquid is infinite, and hence impossible to withdraw a plate. Since, the pressure is also of similar units as that of the stress tensor σ_{xy}, it would also diverge according to the model. Comically, yet in all seriousness, Huh and Scriven referred to this deficiency in the model by stating that: *even Herakles could not sink a solid if such a model were entirely valid*, which was in direct contradiction with the everyday experience.

Hence, the continuum hydrodynamics picture offered by the Navier Stokes was suspect, in particular the no-slip boundary condition. Therefore, a microscopic picture of the processes close to the contact line was

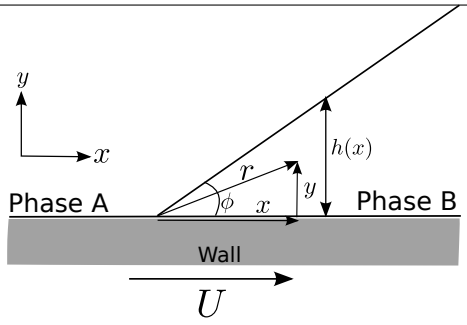

Figure 2.1: The schematic of the Huh-Scriven problem is shown in this figure. Two phases A and B are separated by a wedge whose angle is ϕ with the wall. The wall is moving with a velocity U (in either $+x$ or $-x$ directions). The viscosity ratio between the two phases is given by χ. The radial distance from the contact line is given by r which is composed of a horizontal distance x from the contact line and a vertical distance y.

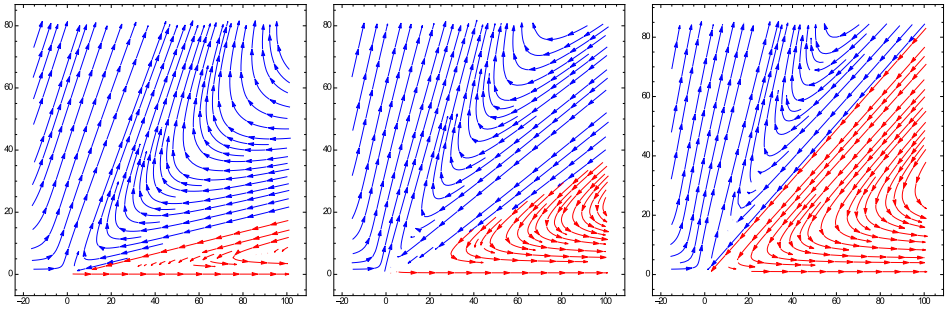

(a) ϕ=10, $\chi = 1$ (b) ϕ=20, $\chi = 1$ (c) ϕ=40, $\chi = 1$

Figure 2.2: The Huh-Scriven velocity fields inside **Phase A** (Blue) and **Phase B** (Red) are plotted for different inclination angles ϕ and viscosity ratio χ=1.0, refer to Figure (2.1). For the plots the velocity U is taken in the direction of positive x-axis. It can be seen that as the wedge angle $\phi \to 0$ the velocity vectors take sharper turns within smaller heights $h(x)$.

required which would help regularize the singularity. Several mechanisms were suggested to remove the stress, pressure singularity:

- **Slip**: A finite slip associated with the velocity at the contact line characterized by the slip length l_s [17]. This allows for a length scale l_s to be introduced which modifies the expressions for the shear stresses and the energy dissipation near the contact line as:

$$\sigma_{xy} \sim \frac{\eta U}{(r + l_s)}, \quad d\dot{E} = \eta U^2 \frac{dr}{(r + l_s)} \tag{2.1}$$

  where $d\dot{E}$ is the rate of energy dissipation in the annulus between r and $r + dr$, η is the viscosity and r is the radial distance away from the contact line, for a schematic see Figure (2.1). As can be seen from the above relations for the viscous stresses and the energy dissipation, the singularity is removed for both the cases.

- **Diffuse Interface**: A diffuse interface between the two immiscible liquids/phases characterized by an interface width ζ [18]. This allows for the co-existence of the no-slip boundary condition and the movement of the contact line is explained by the diffusion whose typical length scale is given by l_D. This is also a common approach adopted in numerical simulations of the contact line [19] [20, 21].

  Throughout this thesis, the *diffuse interface* in the Lattice Boltzmann simulations will be the mechanism by which the moving contact line singularity is regularized.

For a list of the other regularizing mechanisms and their explanations the interested reader is referred to

these excellent review articles [2, 22, 23] and the references therein.

2.1.2 The Cox-Voinov law - Improvements to the Huh-Scriven model

From the previous section we learned that the Huh-Scriven solution provides significant insight regarding the singularity encountered near a contact line as $r \to 0$, however, it *does not* provide the complete hydrodynamical description near the moving contact line. Firstly, the no-slip assumption of the model gives rise to singularities in the viscous stresses as well as the pressure fields. Secondly, it assumes that the shape of the interface is a straight wedge and has zero curvature, as depicted in Figure (2.1). However, the interface near the contact line is indeed deformable as has been observed from experiments [24].

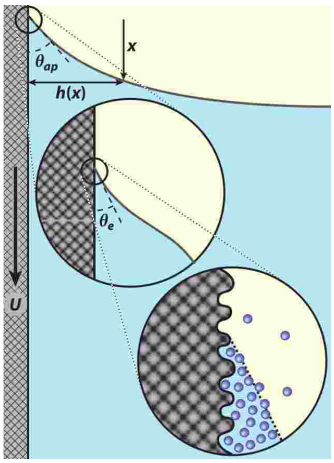

Figure 2.3: A schematic of the curved interface near a moving contact line is shown. The contact line depicted here is an advancing contact line. The microscopic wetting angle and the dynamic wetting angles are represented by θ_{e} (represented from hereon as θ_{m}) and θ_{ap}. The figure is taken from [2].

A model that overcomes the deficiencies of the Huh-Scriven model: (a) a regularizing mechanism to avoid the viscous singularity, as well as, (b) an explanation for the curved shape of interfaces observed in experiments, is the famous Cox-Voinov law [25–27]. The law takes into account a force balance between the surface tension forces and the viscous stresses, and, it describes the curved interface through the dynamic contact angle θ_{ap} as a function of position from the contact line x through the relation:

$$\theta_{\mathrm{ap}}^3 = \theta_{\mathrm{m}}^3 \pm 9Ca \log\left(\frac{x}{l}\right), \tag{2.2}$$

where θ_{m} is the microscopic wetting angle as depicted in Figure (2.1), and l is the cut-off length at the microscopic scale where the discrete nature of the fluid becomes important. Ca is a non-dimensional velocity called the capillary number defined as:

$$Ca = \frac{\eta U}{\gamma}, \tag{2.3}$$

where η, γ, U are the viscosity of the fluid, liquid/gas surface tension and typical velocity. The Ca describes a balance between the viscous and surface tensions forces.

2.1.3 Critical wetting

In the previous section the Cox-Voinov law described the shape of the interface θ_{ap} as a function of the Ca. However, the interface shape becomes unstable beyond a critical capillary number Ca_{cr} and the contact line *fails*. The contact line failure can either lead to the deposition of droplets at the receding contact line, or, it can lead to the entrainment of air bubbles at the advancing contact line. For the receding contact line Equation (2.2) predicts that the failure happens in the limit $\theta_{\mathrm{ap}} \to 0$. An estimate of the Ca_{cr} for the receding

contact line from Equation (2.2) gives:

$$Ca_{cr} \approx \left(\frac{\theta_{\mathrm{m}}}{9 \log\left(\frac{x}{l}\right)} \right)^{\frac{1}{3}}. \tag{2.4}$$

Through the above three sections the three important parameters necessary to study a moving contact line was introduced. First, the microscopic wetting angle θ_e determines the contact angle at the microscopic scales (see Figure (2.3)), second, the non-dimensional velocity Ca describes the balance between the surface tension and the viscous forces close to the contact line, and, third, the cut off length at the microscopic scales l. Since we have identified the key parameters, it is also necessary to pick a geometry in which the moving contact line can be studied. In this thesis we adopt the Couette flow geometry. The next section introduces the reader to the Couette flow geometry and derives the relevant non-dimensional parameters.

2.2 Couette flow geometry - A model to study moving contact lines

2.2.1 Introduction

In the previous sections, the basic aspects of the moving contact line were discussed. In this section, we introduce the Couette flow geometry as a model to study moving contact lines [19, 28]. In Figure (4.14) a schematic of the Couette flow geometry is shown. The geometry consists of two immiscible fluids **Fluid A** and **Fluid B** sandwiched between walls separated by height H. The lower wall moves with a velocity U_w in the positive x-direction and the top wall moves with a velocity U_w in the negative x-direction. Different microsopic wettabilities for Fluid A and Fluid B are prescribed at the top and bottom wall. Fluid A is assigned a microscopic wetting angle $\theta_{m,1}$ at the bottom wall, and, Fluid B is assigned a microscopic wetting angle $\theta_{m,2}$ at the top wall. We study the specific case where $\theta_{m,1} = \theta_{m,2}$, and, in this thesis, we refer this condition as *equal and opposite wettability* or *symmetric wetting*. The dynamic viscosities of Fluid A and B are denoted by η_l, η_r respectively. The reason for adopting the above mentioned model for studying moving contact lines is due to the following reasons [19]:

- the shape of the interface becomes symmetric with respect of the center channel. However, this advantage is strictly valid for the case of *equiviscous liquids* and *equal and opposite wettability*.
- it allows the problem to be treated using the quasi-parallel approximation (see Figure (2.4b)), which implies that the $h'(x)$ varies slowly over the channel, and hence, lubrication theory can be employed to analytically derive the velocity fields and also the shape of the interface [29].
- It is also easier to define a measure for the dynamic contact angle θ_{ap} in this channel. It is defined as the angle at the center of the channel.

Now that the Couette-flow model has been described it is important to identify the necessary parameters and non-dimensional quantities which will allow us to study the moving contact line problem as described by the Cox-Voinov model. However, we first formulate the hydrodynamical equations and the relevant boundary conditions.

2.2.2 Relevant equations and boundary conditions

We outline the governing equations and boundary conditions for the Couette flow geometry. The *steady state flow equations*, in the lubrication approximation [28, 29], to be solved for both **Fluid A** and **Fluid B** are the following:

1. **Momentum equation**:

$$0 = -\boldsymbol{\nabla} p_l + \eta_l \boldsymbol{\nabla}^2 \boldsymbol{u}_l, \quad 0 = -\boldsymbol{\nabla} p_r + \eta_r \boldsymbol{\nabla}^2 \boldsymbol{u}_r, \tag{2.5}$$

simplifies for the x-component as:

$$\eta_l \frac{\partial^2 u_{l,x}}{\partial y^2} = \frac{\partial p_l}{\partial x}, \quad \eta_r \frac{\partial^2 u_{r,x}}{\partial y^2} = \frac{\partial p_r}{\partial x}, \tag{2.6}$$

where p_l, p_r, $\boldsymbol{u}_r$ and $\boldsymbol{u}_r$ are the pressure fields and velocity fields in Fluid A and Fluid B, respectively.

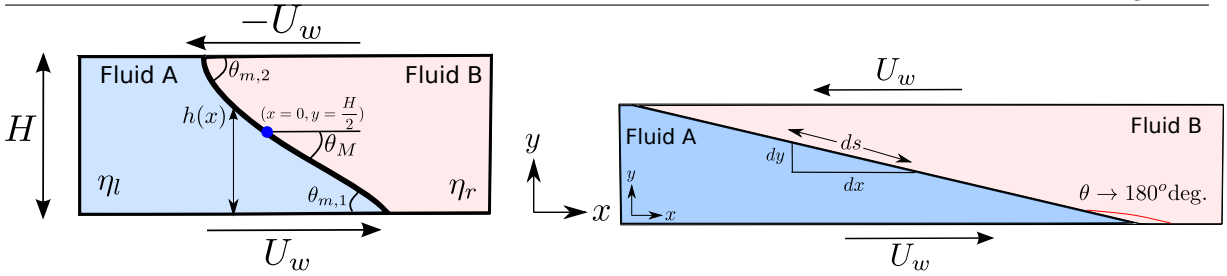

(a) Couette Flow geometry (b) Quasi parallel approximation

Figure 2.4: In (a) the schematic for the Couette flow geometry is shown. Two immiscible fluids **Fluid A** (dynamic viscosity η_l, lower wall microscopic wetting angle $\theta_{m,1}$) and **Fluid B** (dynamic viscosity η_r, upper wall microscopic wetting angle $\theta_{m,2}$) are sandwiched between the top and bottom walls, at a distance H apart, and, form an interface. The length of the channel along the x-direction is infinite. The top and bottom walls are moved in the opposite directions with a magnitude of velocity U_w due to which interface is deformed and reaches steady shape $h(x)$, where x is the distance from the contact line. The measure of the dynamic contact angle $\theta_{\rm ap}$ (as shown in Figure (2.3)) is the angle at the center of the channel θ_M. The x co-ordinate at the central blue point is 0 and the y coordinate is $H/2$. (b) The quasi-parallel approximation is depicted. Given very low microscopic wetting angles $\theta_{\rm m,1}$ and $\theta_{\rm m,2}$ every segment of the interface ds is almost parallel to the wall [19]. Therefore, an approximation $ds \approx dx$ is made.

2. **Continuity equation**:

$$\boldsymbol{\nabla} \cdot \boldsymbol{u}_l = 0, \quad \boldsymbol{\nabla} \cdot \boldsymbol{u}_r = 0,$$

simplifies to:

$$\frac{\partial u_{l,x}}{\partial x} + \frac{\partial u_{l,y}}{\partial y} = 0, \quad \frac{\partial u_{r,x}}{\partial x} + \frac{\partial u_{r,y}}{\partial y} = 0. \tag{2.7}$$

The x-component of the velocity fields in the region surrounding the interface can be obtained from Equation (2.6):

$$u_{l,x}(x,y) = \frac{1}{\eta_l}\Big(A_l + B_l y + \frac{1}{2}p_{l,x}y^2\Big), \quad u_{r,x}(x,y) = \frac{1}{\eta_r}\Big(A_r + B_r y + \frac{1}{2}p_{r,x}y^2\Big), \tag{2.8}$$

where A_l, B_l, $p_{l,x}$, A_r, B_r, $p_{r,x}$ are the 6 constants which has to be determined from the necessary boundary conditions. It can be observed that the velocity field is quadratic and resembles a Poiseuille-like profile. To evaluate the 6 constants in Equation (2.8), following 6 **boundary conditions** are applied:

- **No slip at the interface:**

$$u_{l,x}|_h = u_{r,x}|_h, \tag{2.9}$$

The velocity vector in Fluid A and B, just across the interface $(x, h(x))$ are found to be equal in direction and magnitude.

- **Continuity of viscous stresses across interface:**

$$\boldsymbol{t}_s \cdot \left(\underline{\underline{\boldsymbol{\sigma}}}|_2 - \underline{\underline{\boldsymbol{\sigma}}}|_1\right) \cdot \boldsymbol{n}_s + \boldsymbol{t}_s.\boldsymbol{\nabla}_s\gamma = 0,,$$

where $\boldsymbol{t}_s$, $\boldsymbol{n}_s$, $\underline{\underline{\boldsymbol{\sigma}}}$, γ are the tangential vector, normal vector, flow stress tensor in either fluid and the surface tension between **Fluid A** and **Fluid B**, respectively. This equation in the lubrication limit simplifies to [29]:

$$\eta_l \frac{\partial u_{l,x}}{\partial y}|_h = \eta_r \frac{\partial u_{r,x}}{\partial y}|_h, \tag{2.10}$$

where η_l and η_r are the dynamic viscosities of **Fluid A** and **Fluid B**.

- **Slip at the upper and lower walls**:
  - **Lower Wall**:

$$u_{l,x}|_{y=0} - U_w = l_s \frac{\partial u_{l,x}}{\partial y}|_{y=0}, \tag{2.11}$$

– **Upper Wall**:

$$u_{l,x}|_{y=H} + U_w = -l_s \frac{\partial u_{l,x}}{\partial y}|_{y=H}. \tag{2.12}$$

As was emphasized in Section 2.1 the most important boundary condition in solving the moving contact line problem is the microscopic mechanism of slip. In the Couette flow geometry the slip is introduced through the parameter slip length l_s. It is defined as the length/distance below the wall at which the component of velocity parallel to the wall vanishes. In general, this formulation for the slip at the wall is called the Navier-slip condition [30].

- **Zero mass flux across interface**:

$$\boldsymbol{n}_s \cdot \boldsymbol{u}_l = \boldsymbol{n}_s \cdot \boldsymbol{u}_r = 0,$$

where $\boldsymbol{n}_s$ is the unit normal at the interface. This simplifies to:

$$n_x u_{l,x} + n_y u_{l,y} = n_x u_{r,x} + n u_{r,y} = 0.$$

The above set of equations satisfy the condition that there is no mass flux of one fluid into another, across the interface. However, with the help of Equation (2.7) the condition of no-mass flux across the interface can be simplified to:

$$\int_0^{h(x)} dy\ u_{l,x} \quad = 0, \tag{2.13}$$

$$\int_{h(x)}^{H} dy\ u_{r,x} \quad = 0, \tag{2.14}$$

where $(x, h(x))$ is the steady state interface profile. This condition specifies that there is no net mass flow rate in either of the fluids.

Therefore, the 6 constants are Equation (2.8) is found using the 6 conditions described by Equation (2.9)-Equation (2.14). After the velocity fields have been determined by determining the constants $A_l, B_l, p_{l,x}, A_{r,x}, B_{r,x}, p_{r,x}$, we proceed towards determining the shape of the interface. The shape of the interface is governed by the normal stress balance [29] [1]

$$\Delta p = \gamma \boldsymbol{\nabla} \cdot \boldsymbol{n}_s, \tag{2.15}$$

where $\Delta p\ (= p_r - p_l)$ is the pressure difference across the interface, γ is the surface tension between the two fluids and the gradient of the $\boldsymbol{n}_s$ at the interface gives the curvature κ. This is the well known *Laplace equation*. We differentiate Equation (2.15) with respect to x to obtain the following equation:

$$p_{r,x} - p_{l,x} = \gamma \frac{d\kappa}{dx}, \tag{2.16}$$

where $p_{l,x} = \frac{dp_l}{dx}$, $p_{r,x} = \frac{dp_r}{dx}$ are the pressure gradients in **Fluid A** & **Fluid B**, respectively, and the other terms retain the same meaning. The shape of the interface $(x, h(x))$ is solved under the quasi-parallel approximation where $ds \approx dx$ [19, 28]:

$$\frac{d\kappa}{ds} = \frac{1}{\gamma}(p_{r,x} - p_{l,x}) \tag{2.17}$$

$$\frac{d\theta}{ds} = -\kappa \tag{2.18}$$

$$\frac{dx}{ds} = \cos\theta \tag{2.19}$$

$$\frac{dy}{ds} = \sin\theta \tag{2.20}$$

where $\theta(x) = h'(x)$. Aforementioned equations should satisfy the following boundary conditions at the top and bottom wall:

$$\theta(s \to +\infty) = \theta_{m,1}, \quad \theta(s \to -\infty) = \theta_{m,2}, \tag{2.21}$$

[1] Here the normal stress balance simplifies in the lubrication limit to the Laplace equation. This kind of a simplification is also possible under the assumption that the outer fluid is of negligible viscosity.

where $\theta_{m,1}$ is the microscopic wetting angle for Fluid A at the bottom wall, and, $\theta_{m,2}$ is the microscopic wetting angle for Fluid B at the top wall respectively. The initial curvature κ_0 and the θ_0 are guessed, in order to solve Equation (2.20), until the boundary conditions by Equation (2.21) [19, 28]. We employ a shooting algorithm to obtain the solutions $(x, h(x))$.

In this section we outlined the relevant equations and boundary conditions for obtaining the shape of the interface $(x, h(x))$. Using the shape of the interface we can determine the dynamic contact angle $\theta_{\mathrm{ap}}(x)$ and study it's dependence on the microscopic wetting angle $\theta_{m,1},\ \theta_{m,2}$, wall velocity U_w and the microscopic slip length l_s. In the next section, the physical parameters introduced in the current section can be reduced to a set of non-dimensional parameters and be used to study the critical wetting behavior.

2.2.3 Non-dimensional parameters for critical wetting

In this section we list the non-dimensional parameters that arise from Equation (2.9)-Equation (2.20). The non-dimensional parameters are:

1. **Capillary number**: It is the non-dimensional velocity defined with respect to Fluid A:

$$Ca = \frac{\eta_l U_w}{\gamma}, \tag{2.22}$$

   where η_l is the dynamic viscosity of Fluid A, U_w is the shear velocity and γ is the surface tension between Fluid A and B. As was seen in the Cox-Voinov model Ca characterizes the balance between the viscous stresses and the surface tension forces near the contact line.

2. **Viscosity ratio** χ between Fluid A and Fluid B is given by:

$$\chi = \frac{\eta_r}{\eta_l}, \tag{2.23}$$

   where $\eta_r,\ \eta_l$ are the dynamic viscosities of Fluid B and Fluid A, respectively. See Figure (2.4a).

3. **Scale separation parameter**: λ_s is the ratio of the smallest length scale l_s, where the discrete nature of the fluid becomes important, to the largest length scale in the system, which is given by:

$$\lambda_s = \frac{l_s}{H}, \tag{2.24}$$

   where l_s is the slip length and H is the height of the channel, which is the only external length scale in the problem.

4. **Microscopic wetting angle**: θ_m is the microscopic wetting angle which controls the wettability of one fluid with a wall.

Using the above four parameters the Couette flow geometry can be used to understand the critical wetting behavior of the moving contact lines. This model allows us to probe the nature of moving contact lines under the influence of the aforementioned parameters. For a comprehensive and complete study the interested reader is referred to [28]. Here, the central angle θ_M as a function of the Ca is plotted for four different microscopic wetting angles θ_m. The viscosity ratio $\chi = 1.0$ and scale separation parameter $\lambda_s = 10^{-5}$. The θ_M vs Ca is shown in Figure (2.5). As can be seen from Figure (2.5) the Ca_{cr} decreases as the microscopic angle θ_m decreases, or the affinity towards the wall decreases. This is understandable since a higher volume of fluid tends to get entrained with the wall as the wetting increases, or this is tantamount to a smaller microscopic wetting angle (see Figure (2.4a)). Another interesting feature is that the angle θ_M for which the interface fails and gets entrained into the other fluid is different from zero. Therefore, the interface does not become parallel when reaching the Ca_{cr}, rather it fails at a higher angle. Therefore, the Ca_{cr} as predicted in Equation (2.4) is not entirely accurate [19]. In Chapter 4 we revisit this section in order to validate the moving contact lines in the Newtonian case by comparing θ_M vs Ca obtained through Lattice Boltmann with the theory used here. Through this exercise we obtain an estimate for the scale separation parameter λ_s for the LB method.

In this section we described the geometry, used in this thesis, to study the moving contact line problem. Four important parameters used to study the moving contact line were identified: χ (viscosity ratio), Ca

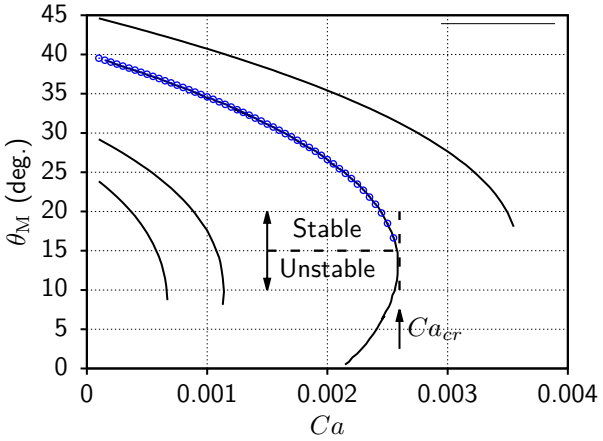

Figure 2.5: The stable branch of the central channel angle θ_M (in deg.) is plotted as a function of Ca for different microscopic wetting angles θ_m, viscosity ratio $\chi = 1.0$ and scale separation ratio $\lambda = 10^{-5}$. The microscopic wetting angles satisfy the opposite wettability criteria. In the figure the blue circles correspond to the data obtained by solving the eqn's Equation (2.18)- Equation (2.21) for $\theta_m = 40^o$ and it is compared against the data obtained from figure 2(a) in [28]. The critical Capillary number Ca_{cr} is pointed for the case of $\theta_m = 40^o$. The points above the Ca_{cr} correspond to stable equilibrium interfaces, whereas, the points below the Ca_{cr} correspond to the unstable equilibrium interfaces. Unstable equilibrium interfaces correspond to strongly bent interfaces near the wall.

(capillary number), λ_s (scale separation parameter) and θ_m (microscopic contact angle). The aforementioned parameters describe the moving contact line problem for Newtonian fluids.

However, the goal of this thesis is to study the moving contact line problem in non-Newtonian fluids. It is well known that non-Newtonian fluids are composed of polymers dissolved in solvents [31]. It is also known that polymers exhibit their own dynamics on a typical time scale τ_P (polymer relaxation time) [32]. Hence, in addition to the time scale of the flow field, an additional time scale due to the polymer relaxation time (τ_P) needs to be accounted for. In the next section, to address these competing time scales in our problem an additional non-dimensional parameter called the Weissenberg number Wi is defined.

2.3 Modeling the non-Newtonian behavior

The focus of this thesis is to investigate moving contact lines for the case of non-Newtonian fluids. Firstly, an introduction to some of the basic concepts of non-Newtonian flow rheology will be discussed. Basically, in addition to the already present non-dimensional numbers (previously discussed), an additional non-dimensional number due to the relaxation time scale of the polymer in the flow (τ_P), called the *Weissenberg number* (Wi) is introduced [33]. This section is ended by introducing the relevance of Wi in a contact line problem.

2.3.1 Introduction - The Maxwell model

Modeling the behavior of polymers in fluids from the concepts of kinetic theory have been successful in capturing their macroscopic response to different stress fields [34]. From the microscopic predictions, one of the most fascinating properties common to all the complex fluids is the presence of viscoelasticity [32, 35]. The Maxwell model schematically describes the viscoelastic nature of liquids as a series combination of a Hookean spring and a dashpot, see Figure (2.6). The displacement of a Hookean spring is linear under the influence of an externally applied force, and, the dashpot is linear to the rate of change of displacement of the piston inside it. In a series connection of the spring and dashpot the stresses across both the elements are equal to the stress applied at the ends. Whereas, the total deformation ϵ of the spring dashpot element

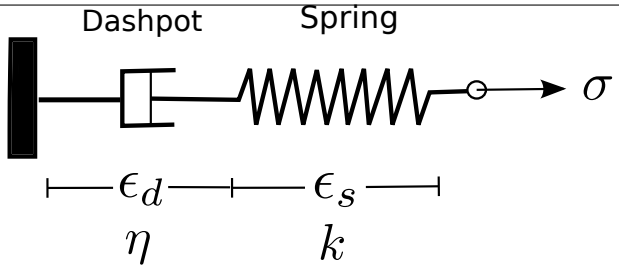

Figure 2.6: The Maxwell model

under a given load σ is equal to the sum of the individual deformations:

$$\sigma = \sigma_s = \sigma_d, \tag{2.25}$$
$$\epsilon = \epsilon_s + \epsilon_d, \tag{2.26}$$
$$\tag{2.27}$$

where subscripts s and d represent the spring and the dashpot. Now, a connection between the stress σ and the strain ϵ is made by the following:

$$\dot{\epsilon} = \dot{\epsilon}_s + \dot{\epsilon}_d = \frac{\dot{\sigma}}{k} + \frac{\sigma}{\eta}, \tag{2.28}$$

where k is the spring stiffness and η is the dissipative constant in the dashpot. It can be seen that the dimension of $\frac{\eta}{k}$ is that of time $[s]$, and hence, the quantity $\frac{\eta}{k}$ is called the relaxation time τ. Therefore, the time evolution of the stress obeys the following equation:

$$k\dot{\epsilon} = \dot{\sigma} + \frac{1}{\tau}\sigma. \tag{2.29}$$

Equation (2.29) is a first order ordinary differential equation and is popularly called the Maxwell model for a linear viscoelastic liquid. From equation Equation (2.29) it can be seen that the model predicts a relaxation of stress with a time scale τ when subjected to a constant strain field. This is consistent in modeling polymers in a flow. However, the model predicts a linear relation between strain and time for the case when the stress σ is constant, when actually it is observed through experiments that the strain increases with a specific time scale.

2.3.1.1 The relaxation and loss modulus for a viscoelatic material

The behavior of a viscoelastic fluid under a periodic stress signal best illustrates the concept of a *solid* and a *fluid* like behavior associated with a viscoelastic fluid. This can also be realized through the Maxwell model.

Suppose an oscillatory strain $\epsilon(t)$ is applied to a viscoelastic fluid, whose form can be given by:

$$\epsilon(t) = \epsilon_0 \sin(\omega t),\ \dot{\epsilon}(t) = \epsilon_0 \omega \cos(\omega t), \tag{2.30}$$

where ϵ_0 is the amplitude of the strain signal, ω is the angular frequency of the signal, t is the time, and $\dot{\epsilon}(t)$ is the time derivative of the strain signal. The corresponding stress response $\sigma(t)$ of the viscoelastic fluid can be assumed to be:

$$\sigma(t) = \sigma_0(\omega)\sin(\omega t + \delta(\omega)) = \epsilon_0(\underbrace{G'(\omega)\sin(\omega t)}_{\text{Signal in-phase}} + \underbrace{G''(\omega)\cos(\omega t)}_{\text{Signal out-of-phase}}), \tag{2.31}$$

where σ_0 is the amplitude of the stress, δ is a phase lag introduced between the strain and stress signal, $G' = \frac{\sigma_0}{\epsilon_0}\cos(\delta) = \frac{\omega^2\tau^2}{1+\omega^2\tau^2}$, $G'' = \frac{\sigma_0}{\epsilon_0}\sin(\delta) = \frac{\omega\tau}{1+\omega^2\tau^2}$ are the *elastic (storage)* and the *loss (viscous)* modulus. The signal in phase corresponds to the in phase response of the viscoelastic liquid which is analogous to a Hookean solid. The out of phase response is characteristic response of a viscous liquid since the stresses in a liquid are proportional to the shear rate, see Figure (2.7). At very low frequencies ω , such that $\omega\tau \ll 1$, G'' dominates G' and the viscoelastic substance behaves more like a liquid. However, after the crossover frequency ($\omega\tau > 1$, see Figure (2.7)) G' dominates G'' and the solid essentially behaves like a solid. This kind

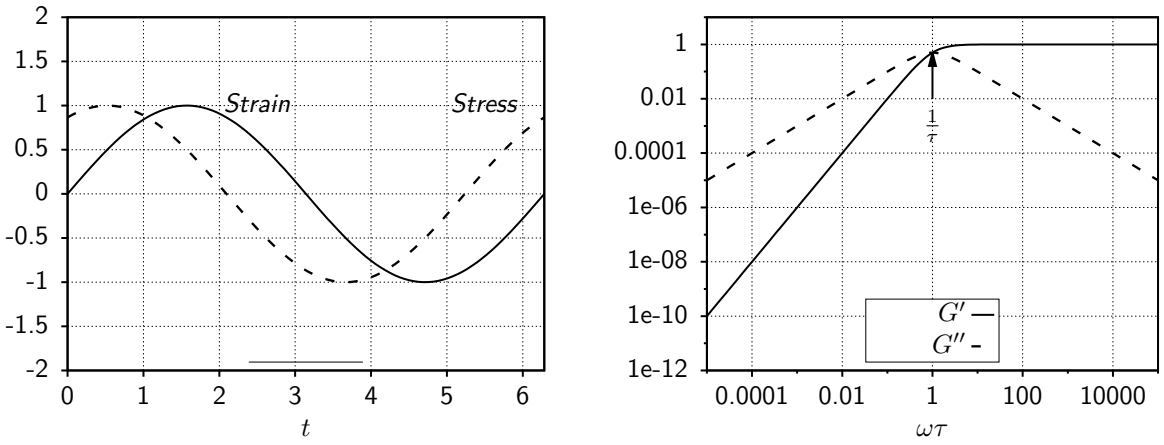

Figure 2.7: The applied strain and the recovered stress signal for a typical viscoelastic fluid is plotted in (a). The stress signal lags behind the strain by a phase δ. In (b) the storage (G') and the loss modulus (G'') for a viscoelastic material is plotted as a function of the non-dimensionalized frequency. There is a crossover at $\omega\tau = 1$ which corresponds to the ratio $1/$relaxation time.

of a behavior is observable in a silly putty. A silly putty when left without any disturbance starts to flow on long time scales, hence behaving like a fluid. However, when the silly putty is thrown towards a solid surface, it bounces back showing a behavior characteristic of solid objects.

Hence, through this basic introduction it was highlighted that a viscoelastic fluid has characteristics of both a solid as well as fluid. The stresses in such a material decay with a certain time scale which is representative of the relaxation time of the polymers in the fluid. A model which successfully captures some of the behavior of viscoelastic fluids is the Maxwell model. The Maxwell model was used to calculate the storage and loss modulus for the case of dynamic strain condition. An introduction to some of the more fundamental bead-spring models of polymers will be dealt extensively in Chapter 3. In the next section, some of the commonly observed non-Newtonian effects will be discussed.

2.3.2 Typical non-Newtonian effects

In the previous section the Maxwell model was introduced which could predict the presence of both a solid-like and liquid-like behavior in viscoelastic liquids. However, apart from the solid and liquid like behavior, viscoelastic liquids exhibit interesting (and fascinating) phenomena when subjected to flow conditions similar to that of Newtonian fluids. In this section, two such phenomena, namely: (a) **rod-climbing effect** and (b) **shear thinning effect** will be discussed. A brief explanation on the underlying mechanisms behind these fascinating phenomena, namely: (a) shear thinning and (b) normal stresses will be discussed.

2.3.2.1 Shear thinning effects

The shear thinning effect is characterized by a decrease in the viscosity of the liquid under high flow rates or higher pressure drops [31]. The shear stress of the fluid $\mathcal{S}$ and the viscosity η follow the constitutive laws given by:

$$\mathcal{S} \propto \dot{\gamma}^n, \tag{2.32}$$

$$\eta = \eta_0 \dot{\gamma}^{n-1}, \tag{2.33}$$

where $\mathcal{S}$ is the shear stress in the fluid, $\dot{\gamma}$ is the continuous shear rate, η_0 is the *zero shear rate viscosity* and n is a positive exponent whose value helps describe the material of the shear stress as a function of the shear rate. $n = 1$ corresponds to a Newtonian fluid, $n > 1$ for a shear thickening fluid, and finally, $n < 1$ for a shear thinning fluid. In Equation (2.33) the equation holds for values of $\dot{\gamma} > \dot{\gamma}_c$, where $\dot{\gamma}_c$ is the critical shear rate after which thinning is observed. The shear thinning behavior is usually a characteristic nature of solution containing polymeric molecules which at high shear rates start to align with the direction of flow, and hence,

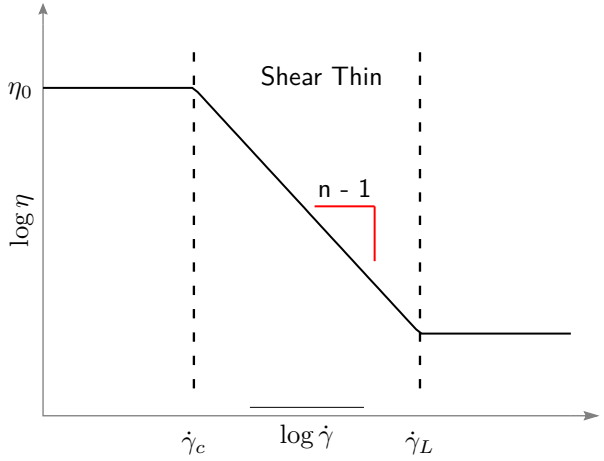

Figure 2.8: The viscosity η of shear thinning fluids in response to a shear rate $\dot{\gamma}$ is plotted. At very low shear rates : $\dot{\gamma} \to 0$, the viscosity plateaus and is assigned a *zero shear rate viscosity* η_0. Beyond a *critical shear rate* $\dot{\gamma}_c$ the viscosity η has a power law dependence on the shear rate $\dot{\gamma}$, characterized by an positive exponent n. Some special class of fluids called *superfluids* show a second plateau in the viscosity η at a *second critical shear rate* $\dot{\gamma}_L$. The figure has been adopted from [12].

reduce the viscosity of the solution. However, it should also be mentioned that at the highest shear rates the viscosity will reduce towards that of the Newtonian solvent.

2.3.2.2 Normal stress effects

Our common experience with Newtonian fluids has been that when a rod immersed inside a fluid and continuously rotated the fluid is flung outwards (due to inertia) towards the edge of the walls. However, surprisingly, when non-Newtonian fluids are subjected to a similar kind of flow they start climbing the rod, see Figure (1.3a). The rod climbing effect is also the called the Weissenberg effect for non-Newtonian fluids [31]. The Weissenberg effect in non-Newtonian fluids is observed due to the presence of anisotropy of stresses in the stress tensor. The measure of this anisotropy is called the normal stress $\mathcal{N}$ and can be defined as (see Figure (2.9)):

$$\mathcal{N} = \sigma_{x_1} - \sigma_{x_2} \tag{2.34}$$

where σ_{x_1}, σ_{x_2} represents the stresses in the direction x_1 where x_2 is the direction of shear and x_2 is the direction normal to it. In the case of the rod-climbing phenomena, the rotation of the rods creates a corresponding shear stress inside the fluid and this stretches the polymers in the solution. Hence, the polymer reacts back on the fluid by inducing normal stresses (*elastic stresses*) which leads to the rod climbing effect [36].

In addition to the definition of the normal stress $\mathcal{N}$, typically a normal stress coeffecient Ψ_1 can be defined as the following [11]:

$$\Psi_1 \equiv \frac{2G'}{\omega^2}, \tag{2.35}$$

where G' is the storage modulus measured from an oscillatory shear experiment and ω is the associated frequency, see Figure (2.10). From previous section we learned that a viscoelastic fluid can have a (a) fluid like behavior characterized by G'' , and, (b) a solid like behavior characterized by an elastic modulus G'. Figure (2.10) represents the dynamic viscosity ($\equiv \frac{G''}{\omega}$, where G'' is the viscous modulus) and the first normal stress difference coefficient Ψ_1' ($\equiv \frac{2G'}{\omega^2}$, where G' is the elastic modulus), over a wide range of frequencies [11]. For a typical elastic fluid, with no shear thinning characteristics over the probed range of $\dot{\gamma}$, the dynamic viscosity is constant like a Newtonian fluid, however, unlike the Newtonian fluid, the first normal stress difference coefficient is non-zero. Further, as the shear rates are decreased to very low values $\Psi_1 \to \Psi_{10}$. According to the Oldroyd model [37] [2] a typical relaxation time can be defined by the following

[2] The Oldroyd model is a special case of the FENE-P model which is explained in Chapter 3. Here, the purpose of the Oldroyd model should be thought of as a theory for purely elastic fluids which do not exhibit shear thinning in the range of $\dot{\gamma}$ probed.

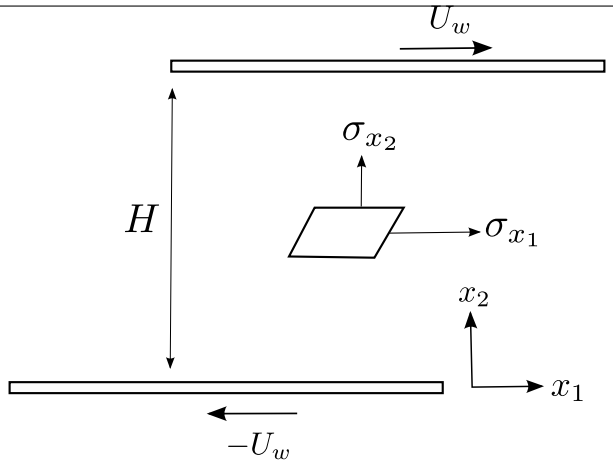

Figure 2.9: A simple shear in the direction x_1 is depicted where the non-Newtonian fluid in between the two plates is sheared with a shear $\dot{\gamma}$. The stress on a representative fluid element is portrayed. The non-zero stress difference σ_{x_1}-σ_{x_2}: between the stress along the direction x_1 and x_2 gives rise to the *first normal stress difference* $\mathcal{N}$. The first normal stress difference for small shear rates $\dot{\gamma}$ is proportional to $\dot{\gamma}$.

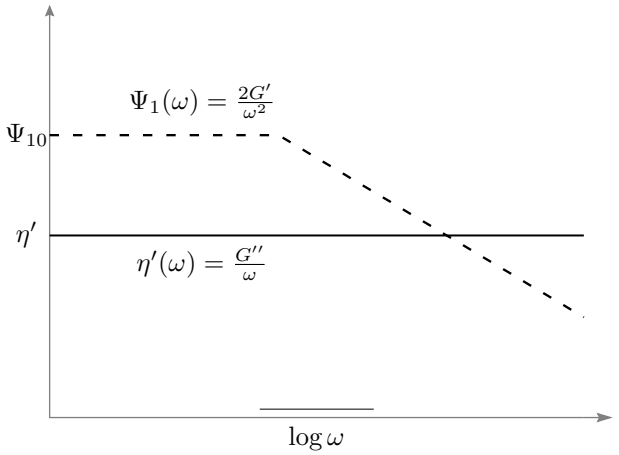

Figure 2.10: Schematic of the rheology of an elastic fluid with no shear thinning. Solid line represents the shear-rate-independent viscosity. Dashed line represents the first normal stress difference coefficient Ψ.

relation:

$$\tau = \frac{\Psi_{10}}{2\eta_0}, \tag{2.36}$$

where η_0 is the *zero shear rate viscosity* and τ is the relaxation time of the polymers in the fluid. However, this does not represent the complete picture, since we have assumed that the viscoelastic liquid is made of only a single type of polymer, hence a single characteristic relaxation time τ. Whereas, in reality, the makeup of viscolelastic liquids can be complicated with a spectrum of relaxation times τ_k, where k corresponds to the different kinds of polymers.

2.4 Non-Newtonian effects in moving contact lines - The Weissenberg number

Finally, the above mentioned non-Newtonian effects are linked to the moving contact line problem. As was discussed in the previous sections the shear rates near the contact line attain very high values due to the sharp turns in the velocity fields within a very small height $h(x)$. As a consequence both the non-Newtonian

effects: (a) shear thinning, (b) normal stress effects become relevant as per the following set of equations:

$$\mathcal{S} \propto \dot{\gamma}^n \tag{2.37}$$
$$\mathcal{N} \propto \dot{\gamma}^2. \tag{2.38}$$

where $\dot{\gamma}$ is the shear rate, $\mathcal{S}$ corresponds to the shear stress of the fluid and $\mathcal{N}$ corresponds to the normal stress measured in the fluid, both of which were discussed in the previous sections. However, it should be remembered that to understand the non-Newtonian effects on the contact line it is beneficial to separately treat *shear thinning* and *normal stress* effects. For example, in experimental studies a special class of fluids called the Boger fluids exhibit only elastic effects [37, 38], without shear thinning. Whereas, another class of solutions, called the Xanthan gum (commonly called as XG solutions) exhibit purely shear thinning effects (without elastic effects below some shear rate) [11]. Based on the intrinsic relaxation time scale τ, derived in Equation (2.36), the *Weissenberg* number can be defined as:

$$Wi = \frac{\tau U}{L_f}, \tag{2.39}$$

where U and L_f are the typical velocity and length scales in the system. Therefore, for the contact line, the length scale L_f approaches 0 and the shear rates $\dot{\gamma}$ approach very large magnitudes. Therefore, according to eqns Equation (2.37)-Equation (2.38), the values of the normal stresses reach very high magnitudes and the effects of shear thinning start cannot be neglected. Hence, it is very interesting to see the effects that normal stresses and the shear thinning have on the contact line motion. However, in this thesis we are primarily concerned with the effects of viscoelasticity on the contact line motion. This topic will be dealt with in Chapter 4.

2.5 Conclusion

In this chapter the theoretical background necessary to understand a moving contact line problem was introduced. Firstly, the Huh-Scriven problem was introduced and the singularity arising in the shear stress, energy dissipation and also the pressure gradients was highlighted. As a result two regularizing mechanisms were introduced to alleviate the problem of singularity near the contact line. The most commonly used regularizing microscopic mechanism at the contact line is the Navier slip condition which introduces a slip length and hence also removes the singularity in the shear stress and the energy dissipation. Another assumption from the Huh-Scriven solution, that of a straight and planar interface, fails close to the moving contact line and the interface is actually found to have finite curvature. Further, the interface has to be curved due to the balance between the viscous stresses and the surface tension forces. This aspect was taken care by the Cox-Voinov solution which related the slope of the interface to the equilibrium contact angle and also the Ca. We introduced the Couette flow geometry which is the geometry adopted in this thesis to study the moving contact line problem. The key non-dimensional parameters were identified required for the studying the moving contact line problem.

The goal of this thesis is to investigate the non-Newtonian aspects of a contact line. Introduction of a non-Newtonian fluid gives rise to another non-dimensional parameter called the Weissenberg number which compares the relaxation time of the polymers with the time scale of the flow. Therefore, we dedicated the rest of the chapter to introduce some basic aspects of non-Newtonian rheology. We began by describing the Maxwell model (spring dashpot model) for viscoelastic liquids through which a relaxation time scale τ $(=\frac{\eta}{k})$ is defined, which defines the time scale on which stresses relax in a viscoelastic liquid. As a result, both liquid-like and solid-like characteristics can be attributed to viscoelastic liquids through the elastic (G') and loss modulus (G''). Following this the elastic and shear thinning effects were introduced and their dependence on the shear rate was highlighted. Finally, the relevance of shear thinning and the normal stress effects in a moving contact line problem was identified through the non-dimensional quantity Weissenberg number (Wi).

Chapter 3

LBM for dilute non-Newtonian rheology

In this chapter, the Lattice Boltzmann formalism for simulating non-Newtonian flow is discussed. Firstly, the discetized Boltzmann equation is introduced, and, we discuss the methodology to solve it on lattices. The lattice implementation of the discretized Boltzmann equation requires the modeling of boundary conditions to accurately simulate fluid behavior, therefore, we present the relevant boundary conditions required for simulating the moving contact line problem. The three phase contact line investigated in this thesis involves multiple fluids. Therefore, we introduce the Shan-Chen model to simulate the physics related to multicomponent fluids. Further, our interest lies in simulating viscoelastic contact lines. Therefore, it is necessary to integrate the dynamics of polymers into the fluid to simulate the non-Newtonian rheology. However, we need a model to represent the dynamics of polymers. In this thesis we have adopted the FENE-P model. We introduce the basic elements of the FENE-P model including the concept of a conformation tensor $\underline{\underline{\boldsymbol{C}}}$, the FENE-P potential $f(r_P)$ and the polmer stress tensor $\underline{\underline{\boldsymbol{\sigma}}}_P$. In addition, we introduce the parameters belonging to the FENE-P model, namely: τ_P (polymer relaxation time), η_P (polymeric viscosity) and L^2 (the maximum extensible length square), which will be used extensively in Chapter 4 to investigate viscoelastic contact lines. Finally, we end the chapter by explaining how the dynamics of the polymer is integrated to the fluid flow equations (solved by the LB) formalism

3.1 Lattice Boltzmann method for fluid flows

3.1.1 Lattice Boltzmann: the discretized Boltzmann equation

The Boltzmann equation describes the conservation equation for the distribution function $f(\boldsymbol{r}, \boldsymbol{v}, t)$ in both space and time and is given as [39, 40]:

$$\frac{\partial f}{\partial t} + (\vec{v} \cdot \nabla_{\vec{r}}) f = Q(f), \tag{3.1}$$

where $f(\boldsymbol{r}, \boldsymbol{v}, t)$ is the distribution function which is defined as the number of molecules residing per unit volume in phase space, $\nabla_{\vec{r}}$ is the gradient in space and $Q(f)$ is the collision operator. In equilibrium, the distribution function approaches a space-and-time-independent function:

$$\lim_{t \to \infty} f(\boldsymbol{r}, \boldsymbol{v}, t) \to f^{\mathrm{eq}}(\boldsymbol{v}), \tag{3.2}$$

where the system becomes homogeneous at any location $\boldsymbol{r}$ and becomes only a function $\boldsymbol{v}$. The equilibrium distribution function $f_0(\boldsymbol{v})$ can be determined by using the assumption of *molecular* chaos and using the conservation of the total number n, momentum $m\boldsymbol{v}$ and energy [39]:

$$f^{\mathrm{eq}}(\boldsymbol{v}) = \frac{n}{(2\pi m k_B T)^{3/2}} \exp\Big(- \frac{m(\boldsymbol{v} - \boldsymbol{u})^2}{2 k_B T} \Big). \tag{3.3}$$

Now, to discretize the Equation (3.1) we use two simplifications. Firstly, the collision operator $Q(f)$ is approximated by the BGK operator which assumes that the distribution function $f(\boldsymbol{r}, \boldsymbol{v}, t)$ relaxes back to equilibrium f^{eq} with a time equal to τ. The second assumption is that the velocity is discretized in space

to some specific directions but at the same time maintaining the isotropy of the system. Taking these assumptions into consideration the discretized form of the Boltzmann equation is given by:

$$\frac{\partial f_i}{\partial t} + (\boldsymbol{c_i} \cdot \boldsymbol{\nabla_r}) f_i = -\frac{1}{\tau}(f_i - f_i^{\mathrm{eq}}), \tag{3.4}$$

where $f_i := f(\boldsymbol{r}, \boldsymbol{c}_i, t)$ is the distribution as a function of the position vector $\boldsymbol{r}$, discretized velocity vectors $\boldsymbol{c}_i$ and time t. f_i^{eq} is the equilibrium distribution in each of the directions. When implementing Equation (3.4) on a computer the space is also discretized into a lattice consisting of nodes. Different kinds of lattices have been adopted for simulating Equation (3.4), for example: **D**2**Q**9, **D**3**Q**19, **D**3**Q**37 being some of the them [40], see Figure (3.1). **D** refers to the dimensionality of the lattice and **Q** refers to the number of discrete directions in space to which the velocity is discretized (denoted by the subscript i). The discrete velocity vectors are given

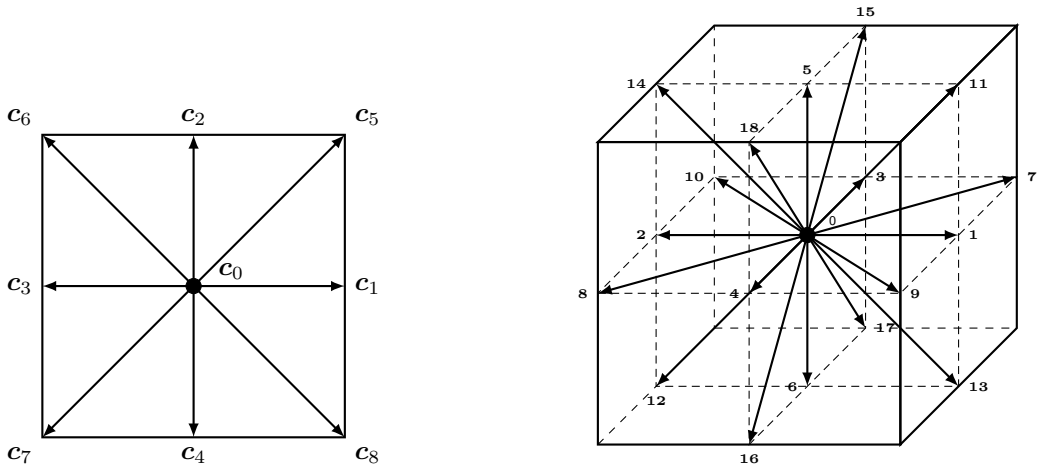

(a) D2Q9 (b) D3Q19

Figure 3.1: The D2Q9 and D3Q19 lattices for used in the discrete Boltzmann equation. The velocity c_0 corresponds to the velocity at the root. The figure is adopted from [41].

by the following:

$$c_i^{\mathrm{D2Q9}} = \begin{cases} (0,0) & i = 0, \\ (\pm 1, 0),\ (0, \pm 1) & 0 < i \leq 4 \\ (\pm 1, \pm 1) & i > 4 \end{cases} \tag{3.5}$$

$$c_i^{\mathrm{D3Q19}} = \begin{cases} (0,0,0) & i = 0, \\ (\pm 1, 0, 0),\ (0, \pm 1, 0), (0, 0, \pm 1) & 0 < i \leq 4 \\ (\pm 1, \pm 1, 0), (0, \pm 1, \pm 1), (\pm 1, 0, \pm 1) & i > 4 \end{cases} \tag{3.6}$$

Similarly, the equilibrium distribution function f_i^{eq} can also be discretized to second order using a Taylor series expansion [42]:

$$f_i^{\mathrm{eq}} = w_i \rho \Big(1 + \frac{1}{c_s^2}(\boldsymbol{c} \cdot \boldsymbol{u}) + \frac{1}{2c_s^4}(\boldsymbol{c} \cdot \boldsymbol{u})^2 + \frac{1}{c_s^2}(\boldsymbol{u} \cdot \boldsymbol{u})^2\Big), \tag{3.7}$$

$$w_i^{\mathrm{D2Q9}} = \begin{cases} \frac{4}{9} & i = 0, \\ \frac{1}{9} & 0 < i \leq 4, \\ \frac{1}{36} & i > 4, \end{cases}$$

$$w_i^{\mathrm{D3Q19}} = \begin{cases} \frac{1}{3} & i = 0, \\ \frac{1}{18} & 0 < i \leq 4, \\ \frac{1}{36} & i > 4. \end{cases}$$

where w_i are the weights associated with each direction and $c_s = \frac{1}{\sqrt{3}}$ is the lattice speed of sound. The discretization of Equation (3.4) leads to the following equation [43]:

$$f_i(\boldsymbol{r} + \boldsymbol{c}_i\Delta t, \boldsymbol{c}_i, t + \Delta t) - f_i(\boldsymbol{r}, \boldsymbol{c_i}, t) = -\frac{\Delta t}{\tau}\Big(f_i(\boldsymbol{r}, \boldsymbol{c}_i, t) - f_i^{\mathrm{eq}}(\boldsymbol{r}, \boldsymbol{c}_i, t)\Big). \tag{3.8}$$

As can be seen Equation (3.8) is the lattice discretized Boltzmann equation without any external forces. Flow quantities like the density $\rho(\boldsymbol{x}, t)$ and the velocity $\boldsymbol{u}(\boldsymbol{x}, t)$ can be calculated using the distribution functions using the following relations:

$$\rho(\boldsymbol{x}, t) = \sum_{i=0}^{i=n-1} f_i(\boldsymbol{x}, t), \boldsymbol{u}(\boldsymbol{x}, t) = \sum_{i=0}^{i=n-1} \boldsymbol{c}_i f_i(\boldsymbol{x}, t). \tag{3.9}$$

Other fundamental properties of the fluid like the kinematic viscosity ν and thermal conductivity are obtained by performing a Chapman-Enskog expansion of Equation (3.8) to yield:

$$\nu = c_s^2\Big(\tau - \frac{\Delta t}{2}\Big). \tag{3.10}$$

It can be observed that if τ is $\frac{\Delta t}{2}$ the LB method becomes unstable.

An important point to notice in all these arguments is that the ideal gas assumption is used. Therefore, there is no interaction between the populations at adjacent nodes. This also implies that there is no phase separation, and hence, an interaction term between the populations at adjacent nodes has to be added. This is dealt with in the following sections.

3.1.2 Boundary conditions

To solve Equation (3.8) it is necessary that appropriate boundary conditions are applied. In Figure (3.2), a typical LB grid is plotted where the number of nodes equals $N_x \times N_y$ where N_x represents the number of fluid nodes in the k-direction and N_y represents the number of fluid nodes in the j-direction. In addition to the fluid nodes ghost nodes are also present. These nodes are used to apply the necessary boundary conditions and they have to be initialized after every time step. Depending on the requirement of the simulation, different kinds of boundary conditions can be applied. Here, two of the commonly used boundary conditions are discussed, which are also relevant to the contact line, namely: (a) periodic boundary condition, and the (b) no-slip boundary condition [43].

3.1.2.1 Periodic boundary condition

If the flow is periodic in the k direction then ghost nodes of type $\boldsymbol{x}'_{A,j}$ and $\boldsymbol{x}'_{C,j}$ should be initialized accordingly. Therefore, before streaming at every time step it should be made sure that the populations at $\boldsymbol{x}'_{A,j}$ are equal to the populations at $\boldsymbol{x}_{C,j}$. Similarly, the populations at $\boldsymbol{x}'_{C,j}$ should be made equal to the populations at $\boldsymbol{x}_{A,j}$. This will ensure that the periodicity is maintained.

Therefore, the periodic boundary condition can be stated as:

$$\begin{aligned} f_i(\boldsymbol{x}'_{A,j}, t) &= f_i(\boldsymbol{x}_{C,j}, t) \\ f_i(\boldsymbol{x}'_{C,j}, t) &= f_i(\boldsymbol{x}_{A,j}, t) \end{aligned}$$

3.1.2.2 No slip boundary condition

The no-slip boundary condition is formulated such that the velocity vector at the wall ($j = \frac{\delta y}{2}$) is zero. This implies that the velocity components need to be individually set to zero. Therefore, the ghost nodes at $j = 0$ and $j = N_y + 1$ have to be set in such a manner that it ensures 0 velocity, see Figure (3.3).

Therefore, the ghost nodes are initialized as:

$$f_2(\boldsymbol{x}'_{B,k}, t) = f_4(\boldsymbol{x}_{B,k}, t) \tag{3.11}$$

$$f_5(\boldsymbol{x}'_{B,k-1}, t) = f_7(\boldsymbol{x}_{B,k}, t) \tag{3.12}$$

$$f_6(\boldsymbol{x}'_{B,k+1}, t) = f_8(\boldsymbol{x}_{B,k}, t). \tag{3.13}$$

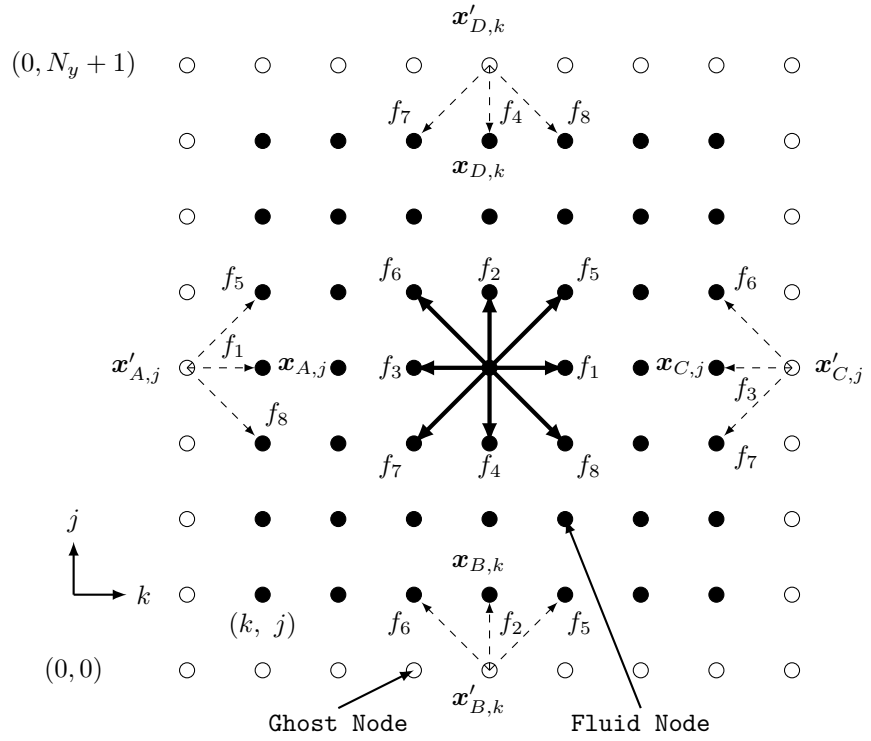

Figure 3.2: An LB D2Q9 lattice of size $N_x \times N_y$ is plotted. The fluid nodes are plotted using filled circles (position given by $\boldsymbol{x}$) whereas the ghost nodes are plotted using the hollow circles, whose positions are denoted by prime co-ordinates.

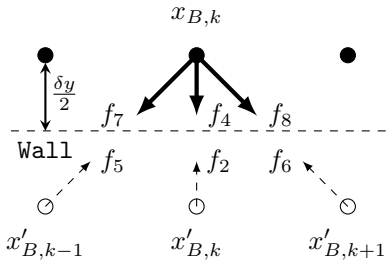

Figure 3.3: A schematic of the bounce back rule leading to a no-slip BC in a D2Q9 LB lattice. The image has been referred from [43]

The above relations ensure that the net momentum at the height $j = \frac{\delta y}{2}$ is equal to zero.

The discretized Boltzmann equation has been introduced. The relevant boundary conditions required for simulating viscoelastic contact lines has also been addressed. However, we need a simulation procedure to introduce multiple components in the fluid. This is necessary because the contact line problem involves multiple components. Therefore, in the next section the Shan-Chen model is introduced which allows us to simulate multiple components.

3.1.3 Shan-Chen multicomponent model

Systems containing fluid species which are different at the molecular level are modeled through the Shan-Chen multicomponent model. For example, an oil droplet inside water is an example of a system which can be modeled using the Shan-Chen multicomponent model. The Shan-Chen multicomponent model is used to describe the interaction between these multicomponent mixtures [44]. Let us consider (Figure (3.4)) the case of a droplet made of component α) resting on a solid, and surrounded by component β. In a multicomponent

system the discretized Boltzmann equation (Equation (3.8)) is solved for components α and β. Therefore, the discretized Boltzmann equation can be rewritten for a component $\xi \in \{\alpha, \beta\}$ as:

$$f_{\xi,i}(\boldsymbol{r} + \boldsymbol{c}_i\Delta t, \boldsymbol{c}_i, t + \Delta t) - f_{\xi,i}(\boldsymbol{x}, \boldsymbol{c}_i, t) = -\frac{\Delta t}{\tau_\xi}(f_{\xi,i}(\boldsymbol{x}, \boldsymbol{c}_i, t) - f^{\mathrm{eq}}_{\xi,i}(\boldsymbol{x}, \boldsymbol{c}_i, t)) + \Delta t \boldsymbol{g}_\xi(\boldsymbol{x}, t) \tag{3.14}$$

where the term $\boldsymbol{g}_\xi$ represents the total force experienced by the component $\xi \in \{\alpha, \beta\}$, τ_ξ is the BGK relaxation time of component $\xi \in \{\alpha, \beta\}$ and i is the index to the discretized velocities. The equilibrium distribution $f^{\mathrm{eq}}_{\xi,i}$ for component ξ is evaluated using Equation (3.7) for the following equilibrium velocity:

$$\boldsymbol{u}^{\mathrm{eq}}_\xi = \boldsymbol{u'} + \frac{\tau_\xi \boldsymbol{g}_\xi}{\rho_\xi}, \tag{3.15}$$

where $\boldsymbol{u}'$ is the common velocity calculated for the two components given by:

$$\boldsymbol{u}' = \frac{\sum_\xi \left(\sum_i \frac{\tau_\xi \boldsymbol{g}_\xi}{\rho_\xi} \right)}{\sum_\xi \frac{\rho_\xi}{\tau_\xi}}, \tag{3.16}$$

where $\boldsymbol{g}_\xi$ is the net force on the component $\xi \in \{\alpha, \beta\}$.

The force experienced by $\xi \in \{\alpha, \beta\}$ due to the other component $\xi' \in \{\alpha, \beta\}$ at location $\boldsymbol{x}$ is given by the following:

$$g_\xi(\boldsymbol{x}) = -\mathcal{G}\rho_\xi(\boldsymbol{x}) \sum_i \sum_{\xi \neq \xi'} w_i \rho_{\xi'}(\boldsymbol{x} + \boldsymbol{c}_i)\boldsymbol{c}_i, \qquad \xi = \alpha, \beta \tag{3.17}$$

where $\mathcal{G}$ is the interaction parameter that controls the strength of interaction between the two components. $i = 0, \cdots, n-1$ represents all the directions corresponding to the discrete velocity, and $\boldsymbol{c}_i$ are the discrete velocities associated with the lattice. It is seen in Equation (3.17) that the interaction is only present between different components (ξ and ξ'), and not between the same set of components. In addition, only forces due to nearest neighbors are considered.

It is important to note fluid α and fluid β become immiscible and form stable interfaces only when the magnitude of the interaction parameter $\mathcal{G}$ is above a critical value $\mathcal{G}_c$. Once the fluids are immiscible and form stable interfaces, it allows us to define a surface tension γ between the two fluids. Further, introduction of interaction parameter $\mathcal{G}$ modifies the pressure tensor. The pressure tensor which originally followed the ideal gas law is modified to [45]:

$$\underline{\underline{\boldsymbol{P}}}(\boldsymbol{x}) = \frac{1}{2}\mathcal{G}\rho_\alpha(\boldsymbol{x}) \sum_i w_i \rho_\beta(\boldsymbol{x} + \boldsymbol{c}_i)\boldsymbol{c}_i\boldsymbol{c}_i + \frac{1}{2}\mathcal{G}\rho_\beta(\boldsymbol{x}) \sum_i w_i \rho_\alpha(\boldsymbol{x} + \boldsymbol{c}_i)\boldsymbol{c}_i\boldsymbol{c}_i. \tag{3.18}$$

After a Taylor series expansion Equation (3.19) simplifies to:

$$\underline{\underline{\boldsymbol{P}}}(\boldsymbol{x}) = \left(p + c_s^2\mathcal{G}\rho_\alpha\rho_\beta + \frac{1}{4}c_s^4\mathcal{G}\rho_\alpha\Delta\rho_\beta + \frac{1}{4}c_s^4\mathcal{G}\rho_\beta\Delta\rho_\alpha\right)\mathbb{1} + \frac{1}{2}c_s^4\mathcal{G}\rho_\alpha\boldsymbol{\nabla}\boldsymbol{\nabla}\rho_\beta + \frac{1}{2}c_s^4\mathcal{G}\rho_\beta\boldsymbol{\nabla}\boldsymbol{\nabla}\rho_\alpha + \mathcal{O}(\nabla^4) \tag{3.19}$$

where $c_s = \frac{1}{\sqrt{3}}$ is the speed of sound in lattice units. The first term is comprised of the ideal gas pressure p plus terms associated with the interaction force $\mathcal{G}$, which are collectively called the bulk pressure. Hence, bulk pressure $P_b = p + c_s^2\mathcal{G}\rho_\alpha\rho_\beta$ considers the non-ideal contribution to the ideal gas pressure. The gradient terms setup the diffuse interface when stable interfaces are formed [46].

3.1.4 Contact angle (θ_{m}) and surface tension (γ)

As seen in Chapter 2 the microscopic wetting angle θ_{m} controls the shape of the interface near a contact line, and also determines the critical wetting behavior of moving contact lines. Hence, in LB it is highly necessary to be able to control the wetting properties of a fluid component when in contact with a wall. In this thesis the technique used by Huang *et al.* [47] will be used to impose a contact angle for a particular component interacting with a wall. According to the model adopted by Huang *et al.* [47] there are two interaction parameters: (a) $\mathcal{G}$ (cohesive forces between components α and β), and, (b) $\mathcal{G}_{\mathrm{wall},\xi}$ (adhesive forces between a component $\xi \in \{\alpha, \beta\}$ and the wall nodes), see Figure (3.4).

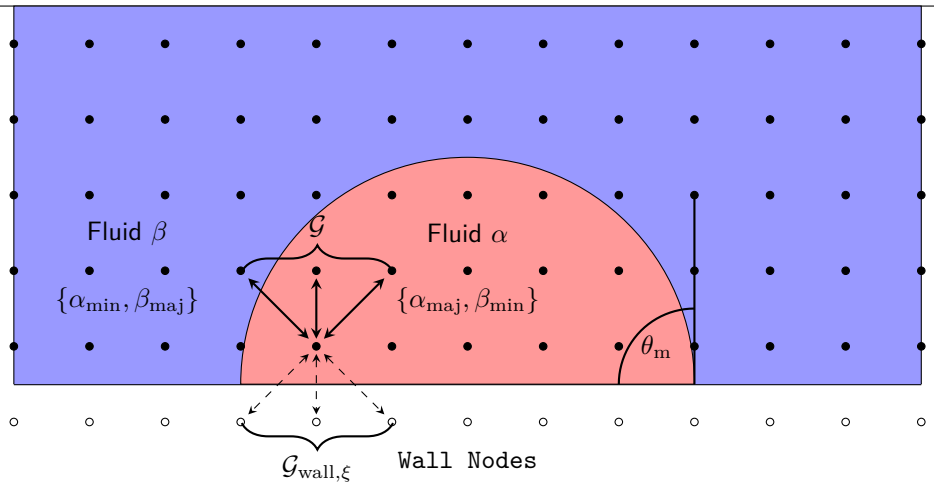

Figure 3.4: A droplet initialized on a lattice in a multicomponent LB simulation is depicted. The droplet in red is initialized with a majority of α component and a minority of β component inside it. In the region outside the droplet the density initializations for the two components are reversed such that the α component is minority and the β component is a majority. The Shan-Chen interaction parameter between the components α and β is given by $\mathcal{G}$. The interaction parameter between component $\xi \in \{\alpha, \beta\}$ and the wall nodes is given by $\mathcal{G}_{\mathrm{wall},\xi}$ ($\xi \in \{\alpha, \beta\}$). The contact angle of the droplet is denoted by θ_{m} which can be controlled using $\mathcal{G}_{\mathrm{wall},\xi}$ ($\xi \in \{\alpha, \beta\}$).

The Shan-Chen interaction force acting on the ξ^{th} component is given by:

$$\boldsymbol{g}_{\xi}(\boldsymbol{x}, t) = \mathcal{G}\rho_{\xi}(\boldsymbol{x}, t) \sum_{i} w_i \rho_{\xi'}(\boldsymbol{x} + \boldsymbol{c}_i, t)\boldsymbol{c}_i, \tag{3.20}$$

where $\xi,\ \xi' \in \{\alpha,\ \beta\}$, i denotes the discretization of the velocity directions. Similarly, the wall force is between the fluid component $\xi \in \{\alpha,\ \beta\}$ and the wall nodes which is given by:

$$\boldsymbol{g}_{\mathrm{wall},\xi}(\boldsymbol{x}, t) = \mathcal{G}_{\mathrm{wall},\xi}\rho_{\xi}(\boldsymbol{x}, t) \sum_{i} w_i s(\boldsymbol{x} + \boldsymbol{c}_i, t)\boldsymbol{c}_i, \tag{3.21}$$

where $\xi \in \{\alpha,\ \beta\}$. The definition for $s(\boldsymbol{x} + \boldsymbol{c}_i, t)$ is as follows:

$$s(\boldsymbol{x} + \boldsymbol{c}_i, t) = \begin{cases} 1 & \text{wall nodes,} \\ 0 & \text{fluid nodes,} \end{cases} \tag{3.22}$$

where the term $s(\boldsymbol{x} + \boldsymbol{c}_i, t)$ plays the role of "density". The definition of $s(\boldsymbol{x} + \boldsymbol{c}_i, t)$ ensures that the force contribution on a component ξ is entirely due to wall nodes. Using the parameter $\mathcal{G}_{\mathrm{wall},\xi}$ the wetting angle θ_{m} can be controlled between the component $\xi \in \{\alpha, \beta\}$, for a combination of the equilibrated bulk density $\rho_{\alpha} + \rho_{\beta}$. Finally, the total force at a particular node ($\sum_{\xi} \boldsymbol{g}_{\xi}$) is calculated as the sum of the internal forces and the external forces. In this case the internal force is the Shan-Chen interaction force (Equation (3.20)), and, the external force is the wall force (Equation (3.21)). The surface tension between the component α and β can also be obtained. This is explained in the context of a droplet and the surrounding (Figure (3.4)).

LB measurement of the contact angle To understand the dependence of θ_{m} as a function of the parameter $\mathcal{G}_{\mathrm{wall},\xi}$, a droplet of initial radius r_0 equal to 15 grid points, are initialized with a bulk density of $\rho_{bulk} = 2.06 = \rho_{\alpha} + \rho_{\beta}$ and relaxation time $\tau_{\alpha} = \tau_{\beta} = 1$. The interaction parameter $\mathcal{G}$ is set to a value of 0.9 and the wall wettability parameter at the lower wall is $\mathcal{G}_{\mathrm{wall},\alpha}$ ($= -\mathcal{G}_{\mathrm{wall},\beta}$) varied from -0.4 to 0.4 [1]. Theoretically the contact angle θ_{m} as a function of the wetting parameter $\mathcal{G}_{\mathrm{ads},\alpha}$ is given by the relation [47]:

$$\cos\theta_{\mathrm{m}} = \frac{\mathcal{G}_{\mathrm{wall},\beta} - \mathcal{G}_{\mathrm{wall},\alpha}}{\mathcal{G}\left(\frac{\rho_{\alpha} - \rho_{\beta}}{2}\right)}, \tag{3.23}$$

[1] A negative value of wall wettability parameter suggests a wetting fluid [47].

where $\mathcal{G}$, ρ_α, ρ_β correspond to the interaction parameter, the equilibriated densities of the 2 components, respectively. A LB simulation was performed to check how the simulation compares against the theoretical prediction of Equation (3.23), see Figure (3.5).

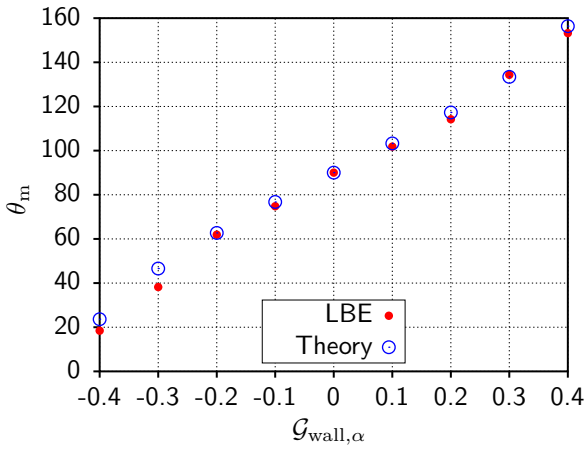

Figure 3.5: The contact angle θ_{m} of a droplet of radii 15 units initialized in a domain of size $N_x \times N_y = 60 \times 30$ with a bulk density of 2.06, $\mathcal{G} = 0.9$, $\tau_\alpha = \tau_\beta = 1.0$, is plotted as a function of the wall adsorption parameter $\mathcal{G}_{\mathrm{wall},\alpha}$. It is compared against the theoretical prediction as derived by Huang *et al.* [47].

It can be seen from Figure (3.5) that the contact angle measurements from the LB match very well with the theoretical prediction, where the error percentages are less than 10%. These values of the wall interaction parameter will be used to set the equilibrium contact angle in the Couette wetting, as was described in Chapter 2.

An important point to note here is that the contact angle has been defined as θ_{m} (micropscopic contact angle). This definition works well for the case of static droplets. However, if the droplets are spreading or moving then we are in the regime of moving contact lines. In that case the contact angle is not θ_{m} (microscopic contact angle) anymore, rather, we need to define a dynamic contact angle θ_{ap} which will be used as a measure of the contact angle.

LB measurement of the surface tension Using the same procedure as in the previous section the surface tension can be obtained for a stable droplet, using the standard Laplace test. For a given $\rho_{bulk} = \rho_\alpha + \rho_\beta$ and $\mathcal{G}$, a multicomponent droplet is initialized. Once the droplet reaches equilibrium the radius of the droplet is calculated using simple trigonometrical relations as shown in Figure (3.6). Once the radius of the drop has

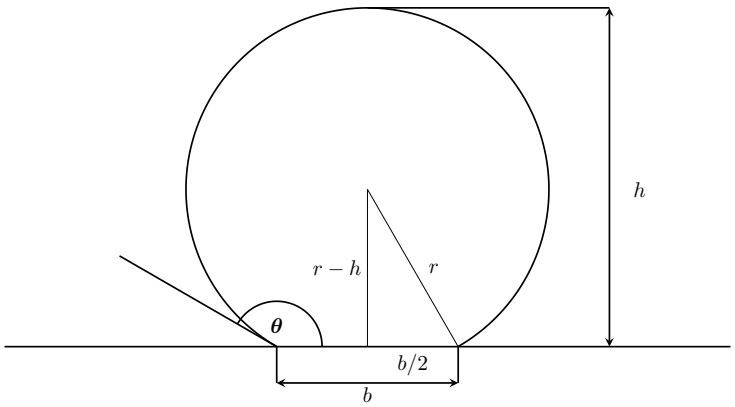

Figure 3.6: The schematic of the measurement of contact angle from a equilibrated droplet is shown in this figure. In a given simulation the base of the droplet can be measured as b and the height as h units. Using the Pythogoras theorem the radius of the droplet is given as $r = \frac{4h^2+b^2}{8h}$.

been calculated, the pressure inside and outside the droplet is calculated using the equation of state for the *Shan-Chen* model:

$$\mathbf{P}_{\text{in, out}} = c_s^2(\rho_\alpha(\boldsymbol{x}) + \rho_\beta(\boldsymbol{x})) + c_s^2\mathcal{G}\rho_\alpha(\boldsymbol{x})\rho_\beta(\boldsymbol{x}), \tag{3.24}$$

where $c_s^2 = \frac{1}{3}$ corresponds to the speed of sound in lattice. Finally, the surface tension γ is the slope of the linear fit of the data between ΔP=P($\boldsymbol{x}_{\text{in}}$)-P($\boldsymbol{x}_{\text{out}}$) and $\frac{1}{R}$. The result of the Laplace test for the surface tension measurement of a multicomponent droplet made of Fluid α initialized inside another component made of $Fluid\beta$ gives a Δp vs $\frac{1}{R}$ (3.4) is given by Figure (3.7).

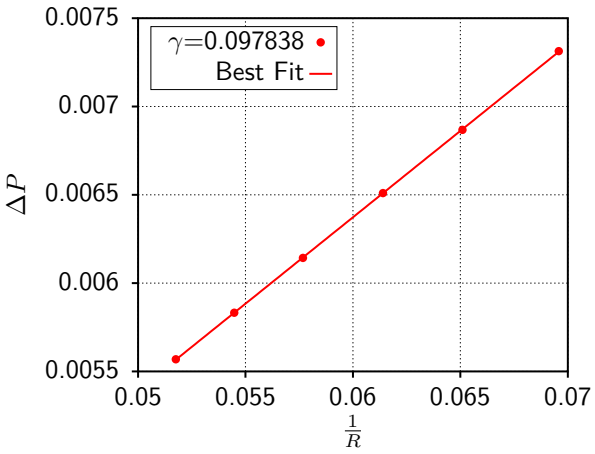

Figure 3.7: The pressure difference $\Delta P = P(\boldsymbol{x}_{in}) - P(\boldsymbol{x}_{out})$ is plotted as a function of $\frac{1}{R}$ for droplets of varying radii. The droplets are initialized with a $\rho_{\text{bulk}} = 2.06$ and an interaction parameter value of $\mathcal{G} = 1.3$. The best fit line is obtained for the two quantities and the slope γ is the surface tension, which for this case is 0.1.

3.2 Polymer dynamics

In the previous section the methodology to solve the flow field through the lattice Boltzmann method was discussed. In this section the equations to solve the polymer dynamics is presented. Through this section we illustrate how the polymer dynamics can be blended with the equations for the fluid motion to simulate the non-Newtonian rheology. However, it is important to first introduce the polymer model which will be integrated with the flow field. In this thesis, we choose the *Finitely Extensible Non-Linear Elastic-Peterlin* (FENE-P from hereon) model for simulating the dynamics of polymers. Therefore, in the first section the basic elements of the FENE-P model will be explained, and the relevant quantities will be introduced. Following this, the equations necessary to evolve the state of polymers in a flow field will be outlined. Finally, the methodology to blend the multicomponent flows with the polymer dynamics will be explained.

3.2.1 The FENE-P model

According to the FENE-P model a polymer chain consists of a spring connecting two non-deformable beads [48] (Figure (3.8)). The two beads are indistinguishable in nature. Now, we can define a vector $\boldsymbol{\mathcal{R}}$, called the director vector, which is an end-to-end vector connecting the two beads [34]. In addition to the director vector $\boldsymbol{\mathcal{R}}$, we can also introduce a potential for the spring. In the FENE-P model the spring is only allowed to stretch a certain length L. Further, a force law can be defined for governing the extension of the spring. The force law for the FENE-P model is defined as the following [34]:

$$\boldsymbol{F}^c = \frac{H\boldsymbol{\mathcal{R}}}{1 - \langle \boldsymbol{\mathcal{R}}^2/L^2 \rangle}, \tag{3.25}$$

where $\boldsymbol{F}^c$, $H, L^2, \langle\cdot\rangle$ represent the force vector due to the spring, the spring constant, the square of maximum extensible length and the *configurational average* [49]. The configurational average can be thought of as an

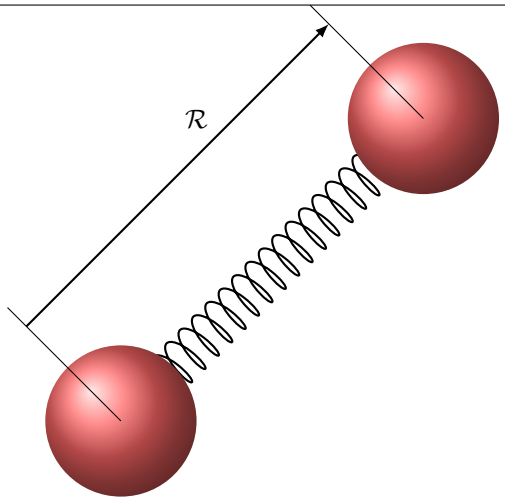

Figure 3.8: A schematic of the dumb-bell representation of a polymer is shown here. Two dumb bells of color red and red are shown with a finitely extensible spring attached between them. The director vector $\boldsymbol{\mathcal{R}}$ is the end to end vector of the polymer connecting the two dumb-bells.

average performed over all the polymers which are subjected to a similar force field [34]. As can be observed from Equation (3.25) the force $\boldsymbol{F}_c$ is non-linear in nature. Further, as the spring extends to a length equal to the maximum extensible length L, in other words as $\boldsymbol{\mathcal{R}}^2 \rightarrow L^2$ in Equation (3.25), the force $\boldsymbol{F}_c$ diverges.

To summarize, the FENE-P model is a simple model of a polymer chain subjected to a force field. The force field is non-linear in nature and allows only a finite extension of the spring connecting the two beads. Now, when the polymers are subjected to a flow field the stresses in the flow field will stretch and compress the polymers [50]. As a result the polymer will exert back a force on the fluid and generate *feedback stresses* (called the polymeric feedback stresses). As a result, we need a quantitative measure of this polymeric feedback stress in order to quantify the behavior of polymers subjected to a flow field. In this thesis, we are interested in understanding how the flow near the contact line affects the behavior of the polymers, and in turn how the polymers affect the flow field. Therefore, in the next section we define two important parameters which will be extensively used in this thesis to quantify both the behavior of polymers in the flow, as well as, the effect that polymers have on the flow, namely: (a) conformation tensor $\underline{\underline{\boldsymbol{C}}}$, (b) polymeric shear stress $\underline{\underline{\boldsymbol{\sigma}}}_P$.

3.2.2 Conformation tensor and polymeric stress tensor

The conformation tensor $\underline{\underline{\boldsymbol{C}}}$ is defined as the second moment of the end-to-end vector $\boldsymbol{\mathcal{R}}$ [34]. An element C_{ij} of $\underline{\underline{\boldsymbol{C}}}$ is defined as:

$$C_{ij} \equiv \langle \boldsymbol{\mathcal{R}}_i \boldsymbol{\mathcal{R}}_j \rangle, \tag{3.26}$$

where $i,\ j$ correspond to the axes directions $x,\ y,\ z$. $\boldsymbol{\mathcal{R}}$ is the director vector from bead 1 to bead 2 and $\langle \cdot \rangle$ is the averaging over the configuration distribution function which is defined by a given flow field [2]. From the relation for the conformation tensor $\underline{\underline{\boldsymbol{C}}}$ it can be seen that the tensor is symmetric in nature, which implies that $C_{ij} = C_{ji}$. Using the definition of a conformation tensor $\mathcal{C}$ the polymeric stress tensor is defined as [50]:

$$\underline{\underline{\boldsymbol{\sigma}}}_P = f(r_{\mathrm{P}}) \underline{\underline{\boldsymbol{C}}}, \tag{3.27}$$

where $f(r_{\mathrm{P}}) = \frac{L^2-3}{L^2-r^2}$ is the FENE-P potential. The term $r = \sqrt{\mathrm{Tr}(\underline{\underline{\boldsymbol{C}}})}$ and it represents the extension length of the polymer. Two important points have to be mentioned regarding the aforementioned relation. Firstly, in a state of equilibrium where the polymers do not undergo stretching $\mathrm{Tr}(\underline{\underline{\boldsymbol{C}}})$ is set to three. In other words, $\underline{\underline{\boldsymbol{C}}}$ is a unity matrix $\mathbb{1}$ when the polymers are in equilibrium. The second important point is that the relation given by Equation (3.27) is phenomenological and follows as part of a definition [50]. It is also evident from

[2] Given a particular flow field and time t, a *configurational distribution function* $\Psi(\boldsymbol{\mathcal{R}}, t)$ can be defined over which the averaging is performed for all the relevant quantities, for example: the product of the elements of the conformation tensor $\boldsymbol{\mathcal{R}}_i \boldsymbol{\mathcal{R}}_j$ [49]

Equation (3.27) that the potential $f(r_P)$ diverges as $r \to L$. Therefore, now we have defined two quantities $\underline{\underline{\boldsymbol{C}}}$ and $\underline{\underline{\boldsymbol{\sigma}}}_P$ which represent the average state of a polymer subjected to a flow field. $\underline{\underline{\boldsymbol{C}}}$ provides information on the average orientation of the polymer, and based on the orientation a polymeric stress terms $\underline{\underline{\boldsymbol{\sigma}}}_P$ is defined.

Now, we move on to describe the evolution of the polymeric quantities mentioned in the previous section, namely $\underline{\underline{\boldsymbol{C}}}$ and $\underline{\underline{\boldsymbol{\sigma}}}_P$, when subjected to flow fields. The evolution of the polymer stress tensor is entirely defined in terms of the conformation tensor $\underline{\underline{\boldsymbol{C}}}$, which satisfies:

$$\overset{\triangledown}{\underline{\underline{\boldsymbol{C}}}} = \frac{f(r_{\mathrm{P}})\underline{\underline{\boldsymbol{C}}} - \mathbb{1}}{\tau_P} \tag{3.28}$$

where $\overset{\triangledown}{\underline{\underline{\boldsymbol{C}}}}$ is the upper convected time derivative defined for tensors (analogous to the material derivative for scalars) [31]. The term τ_P is called the *polymeric relaxation time*, a parameter that will be used constantly throughout the thesis. Therefore, the physical significance of Equation (3.29) is that the conformation tensor relaxes on a typical time scale $\tau = \tau_P$, the polymer relaxation time. τ_P is synonymous to the intrinsic time scale τ of a viscoelastic material that was obtained through the Maxwell model in Chapter 2. Finally, the convected derivative is given by the following:

$$\overset{\triangledown}{\underline{\underline{\boldsymbol{C}}}} = \frac{D\underline{\underline{\boldsymbol{C}}}}{Dt} - \underline{\underline{\boldsymbol{C}}} \cdot \boldsymbol{\nabla u} - \nabla \boldsymbol{u}^T \cdot \underline{\underline{\boldsymbol{C}}} \tag{3.29}$$

where $\frac{D}{Dt}()$ represents the material derivative or the convective derivative.

Therefore, in this section we introduced the basic aspects of the FENE-P model and the quantities relevant to the model, namely: L (maximum extensional length of the polymer), τ_P (relaxation time of the polymer), $\underline{\underline{\boldsymbol{C}}}$ (conformation tensor) and finally $\underline{\underline{\boldsymbol{\sigma}}}_P$ (the polymeric stress tensor). In the next section we outline the numerical scheme (finite difference) used to solve Equation (3.29) , and specify how it is integrated with the flow variables obtained from the LB formalism.

3.2.3 Evolution of conformation tensor - finite difference scheme

In the previous section the equation for the evolution of conformation tensor was discussed, see Equation (3.29). In this section the numerical methodology, i.e. finite difference, used to solve Equation (3.29) is discussed.

Expanding the LHS of Equation (3.29) and rearranging the terms, the following equation is obtained:

$$\frac{\partial \underline{\underline{\boldsymbol{C}}}}{\partial t} = \underbrace{-(\boldsymbol{u} \cdot \boldsymbol{\nabla})\underline{\underline{\boldsymbol{C}}}}_{advection} + \underline{\underline{\boldsymbol{C}}} \cdot \boldsymbol{\nabla u} + (\boldsymbol{\nabla u})^T \cdot \underline{\underline{\boldsymbol{C}}} - \frac{f(r_{\mathrm{P}})\underline{\underline{\boldsymbol{C}}} - \mathbb{1}}{\tau_P} = \underline{\underline{\boldsymbol{C}}}_{\mathrm{RHS}}. \tag{3.30}$$

Equation (3.30) is the evolution equation for the conformation tensor $\underline{\underline{\boldsymbol{C}}}$ and can be expressed in the form:

$$y' = f(t, y) \qquad \text{with} \qquad y(t_0) = y_0,$$

where y' is the derivative of the dependent variable y w.r.t to an independent variable t, and, $f(t, y)$ is the generalized rule according to which y evolves. Similarly, in direct correspondence with Equation (3.30), $\underline{\underline{\boldsymbol{C}}}$ is dependent on time t, and the rhs of Equation (3.30) is the rule according to which the conformation tensor $\underline{\underline{\boldsymbol{C}}}$ evolves. To evolve $\underline{\underline{\boldsymbol{C}}}$ a two-step Adams-Bashforth scheme is used using a polynomial interpolation, according to which:

$$y(t_{n+1}) = y(t_n) + \frac{3}{2}\Delta t f(t_n, y_n) - \frac{1}{2}\Delta t f(t_{n-1}, y_{n-1}),$$

where the subscript n corresponds to the current time step, Δt is the discretization in time and $f(t_n, y_n)$ is evaluated at the current time step. Using a direct correspondence, the evolution equation for Equation (3.30) can be written as:

$$\underline{\underline{\boldsymbol{C}}}(t_{n+1}) = \underline{\underline{\boldsymbol{C}}}(t_n) + \frac{1}{2}(3\underline{\underline{\boldsymbol{C}}}_{\mathrm{RHS}}(t_n) - \underline{\underline{\boldsymbol{C}}}_{\mathrm{RHS}}(t_{n-1})). \tag{3.31}$$

$\underline{\underline{\boldsymbol{C}}}_{\mathrm{RHS}}$ consists of 4 terms, as can be seen in Equation (3.30). These terms are the following:

$$\text{Term 1} \quad : \quad -(\boldsymbol{u}\cdot\nabla)\underline{\underline{\boldsymbol{C}}}, \tag{3.32}$$

$$\text{Term 2} \quad : \quad +\underline{\underline{\boldsymbol{C}}}\cdot(\nabla\boldsymbol{u}), \tag{3.33}$$

$$\text{Term 3} \quad : \quad (\nabla\boldsymbol{u})^T\cdot\underline{\underline{\boldsymbol{C}}}, \tag{3.34}$$

$$\text{Term 4} \quad : \quad -\frac{f(r_{\mathrm{P}})\underline{\underline{\boldsymbol{C}}}-\mathbb{1}}{\tau_P}, \tag{3.35}$$

since the conformation tensor $\underline{\underline{\boldsymbol{C}}}$ has 9 elements the terms involve a calculation for each of these 9 elements. A sample calculation for each of the terms is presented here:

Term 1:

$$-(u\frac{\partial}{\partial x}+v\frac{\partial}{\partial y}+w\frac{\partial}{\partial z})\begin{bmatrix}C_{xx} & C_{xy} & C_{xz}\\ C_{xy} & C_{yy} & C_{yz}\\ C_{xz} & C_{yz} & C_{zz}\end{bmatrix} \tag{3.36}$$

where $u=u(x,y,z), v=v(x,y,z), w=w(x,y,z)$ are the velocity components and each of the elements of the conformation tensor $\underline{\underline{\boldsymbol{C}}}$ are functions of x, y, z. Using *second order* finite difference in space the following is obtained (shown for the first element of the tensor):

$$\begin{aligned}-(u\frac{\partial C_{xx}}{\partial x}+v\frac{\partial C_{xx}}{\partial y}+w\frac{\partial C_{xx}}{\partial z}) = &-u(x,y,z,t)\left(\frac{C_{xx}(x+\Delta x,y,z,t)-C_{xx}(x-\Delta x,y,z,t)}{2\Delta x}\right)\\ &-v(x,y,z,t)\left(\frac{C_{xx}(x,y+\Delta y,z,t)-C_{xx}(x,y-\Delta y,z,t)}{2\Delta y}\right)\\ &-w(x,y,z,t)\left(\frac{C_{xx}(x,y,z+\Delta z,t)-C_{xx}(x,y,z-\Delta z,t)}{2\Delta z}\right),\end{aligned} \tag{3.37}$$

where the discretization in space in the $x,\ y,\ z$ directions are given by Δx, Δy and Δz, and are all equal to 1. Similarly, the above set of equations can be written for all the 6 elements.

Term 2:

$$\begin{bmatrix}C_{xx} & C_{xy} & C_{xz}\\ C_{xy} & C_{yy} & C_{yz}\\ C_{xz} & C_{yz} & C_{zz}\end{bmatrix}\cdot\begin{bmatrix}\frac{\partial u}{\partial x} & \frac{\partial v}{\partial x} & \frac{\partial w}{\partial x}\\ \frac{\partial u}{\partial y} & \frac{\partial v}{\partial y} & \frac{\partial w}{\partial y}\\ \frac{\partial u}{\partial z} & \frac{\partial v}{\partial z} & \frac{\partial w}{\partial z}\end{bmatrix} \tag{3.38}$$

The first element corresponding to (1,1) is:

$$\begin{aligned}C_{xx}\left(\frac{u(x+\Delta x,y,z,t)-u(x-\Delta x,y,z,t)}{2\Delta x}\right)+C_{xy}\left(\frac{u(x,y+\Delta y,z,t)-u(x,y-\Delta y,z,t)}{2\Delta y}\right)+\\ C_{xz}\left(\frac{u(x,y,z+\Delta z,t)-u(x,y,z-\Delta z,t)}{2\Delta z}\right).\end{aligned} \tag{3.39}$$

The general term (i,j) is $\sum_k C_{i,k}\partial_k u_j$ where ∂_k denotes the derivative w.r.t to the k^{th} direction.

Term 3:

$$\boldsymbol{\nabla u}^T\cdot\underline{\underline{\boldsymbol{C}}}=(\underline{\underline{\boldsymbol{C}}}\cdot\boldsymbol{\nabla u})^T. \tag{3.40}$$

Basically, **Term 3** is the transpose of **Term 2**, and from the basic properties of matrices $(\mathrm{AB})^{\mathrm{T}}=\mathrm{B}^{\mathrm{T}}\mathrm{A}^{\mathrm{T}}$, where $\mathrm{A}=\underline{\underline{\boldsymbol{C}}}$ and $\mathrm{B}=\boldsymbol{\nabla u}$. However, since the conformation tensor $\underline{\underline{\boldsymbol{C}}}$ is symmetric, $\underline{\underline{\boldsymbol{C}}}^T=\underline{\underline{\boldsymbol{C}}}$.

Term 4:

$$f(r_{\mathrm{P}})=\frac{L^2-3}{L^2-\mathrm{Tr}(\ \underline{\underline{\boldsymbol{C}}}\ )} \tag{3.41}$$

Firstly, the FENE-P potential at every location (x,y,z) is evaluated depending on the state of the conformation tensor $\underline{\underline{\boldsymbol{C}}}$. After this, the potential is multiplied with the conformation tensor $\underline{\underline{\boldsymbol{C}}}$ and the following operation is performed:

$$\frac{1}{\tau_P}(f(r_{\mathrm{P}})\underline{\underline{\boldsymbol{C}}}-\mathbb{1}), \tag{3.42}$$

at every location x, y, z.

Therefore, some key points need to be clarified regarding the *initialization* of $\underline{\underline{\boldsymbol{C}}}$, evaluation of $\underline{\underline{\boldsymbol{C}}}_{RHS}$ near the boundaries:

1. The magnitudes of the elements of the conformation tensor are all initialized to a value 0. Therefore,
$$\underline{\underline{\boldsymbol{C}}}(t=0) = 0. \tag{3.43}$$
2. At any instant, when calculating the $\underline{\underline{\boldsymbol{C}}}_{RHS}$, the value of $\underline{\underline{\boldsymbol{C}}}$ evaluated from the previous time step is used.
3. The evaluation of the conformation tensor at the boundaries can occur for two different boundary conditions.
   - The first boundary condition is the *periodic boundary condition*. In this case conformation tensor $\underline{\underline{\boldsymbol{C}}}$ is evaluated exactly similar to the periodic boundary condition as mentioned in the section on **Boundary Conditions** (Section (3.1.2)) in this chapter. The evaluation of $\underline{\underline{\boldsymbol{C}}}_{RHS}$ happens at the nodes corresponding to $k = 1$ and $k = N_x$ (see Figure (3.2)) and the magnitudes of the conformation tensor are then copied to the ghost nodes at $k = 0$ and $k = N_x + 1$.
   - All of the above calculations are done only for the fluid nodes, see fig Figure (3.2). Therefore, in order to evaluate the value of $\underline{\underline{\boldsymbol{C}}}_{RHS}$ at the fluid nodes corresponding to the row $j = N_y$ (see Figure (3.2)) using a *second order finite difference* the value of the relevant quantities need to be known at the ghost nodes. Therefore, the values of the conformation tensor $\underline{\underline{\boldsymbol{C}}}$ need to be evaluated at the nodes in the row $j = N_y + 1$. To perform this calculation a first order finite difference (or linear extrapolation) is used.

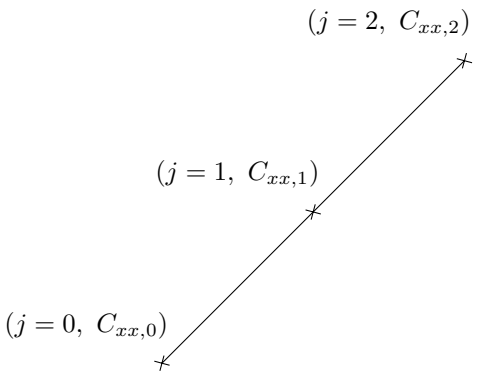

Figure 3.9: At any given i and k such that $j = 0$ the value of the conformation tensor is calculated using the linear extrapolation. For this, 3 points are determined of which $j = 0$ corresponds to the ghost node and the $j = 1,\ 2$ correspond to the fluid nodes. $C_{xx,0}$ corresponds to the value of C_{xx} at $i, j = 0, k$. The equation of the line is given by $y = mx + c$.

A sample calculation at the ghost node j=0 and for C_{xx}, the magnitude of the slope and of the intercept are given by (see Figure (3.9)):

$$m = C_{xx,2} - C_{xx,1},$$
$$c = 2C_{xx,1} - C_{xx,2}.$$

Therefore, using the straight line equation $y = mx + c$, the value of $C_{xx,0}$ is the value of the intercept itself:

$$C_{xx,0} = 2C_{xx,1} - C_{xx,2}. \tag{3.44}$$

This calculation can be extended to all the ghost nodes in all directions x, y, z using the same principles. An important point to note is that the calculation of the conformation tensor at the boundaries are performed before the evaluation of $\underline{\underline{\boldsymbol{C}}}_{RHS}$.

Therefore, in this section the finite difference scheme used to evolve the conformation tensor $\underline{\underline{\boldsymbol{C}}}$ was discussed. From this we understand how to evaluate the dynamics of the conformation tensor if a particular flow field is given. In the next section we understand how the polymer stresses are evaluated included in the momentum equation of the fluid. Basically, this is the *polymer feedback mechanism*.

3.3 Coupling Lattice Boltzmann method and FENE-P

In the previous section we discussed how the flow field $\boldsymbol{u}(x, y)$ is used to evaluate the dynamics of the orientation tensor $\underline{\underline{\boldsymbol{C}}}$. Now, we have to account for the feedback of the polymer into the fluid. This is done by introducing a volumetric body force applied on the fluid in the Navier-Stokes equation, as follows [51]:

$$\rho[\partial_t \boldsymbol{u} + (\boldsymbol{u}\cdot\boldsymbol{\nabla})\boldsymbol{u}] = -\nabla p + \boldsymbol{\nabla}\cdot\underline{\underline{\boldsymbol{\sigma}}}_S + \underbrace{\frac{\eta_p}{\tau_P}\boldsymbol{\nabla}\cdot\underline{\underline{\boldsymbol{\sigma}}}_P}_{\text{polymeric feedback force}} + \sum_{\xi}\boldsymbol{g}_{\xi}, \tag{3.45}$$

where η_P is called the polymeric viscosity, τ_P is the polymeric relaxation time, $\underline{\underline{\boldsymbol{\sigma}}}_P$ is the polymeric stress tensor, $\sum_{\xi}\boldsymbol{g}_{\xi}$ is the Shan-Chen interaction force summed over the components $\xi \in \{\alpha, \beta\}$, $\underline{\underline{\boldsymbol{\sigma}}}_s$ is the stress tensor due to the fluid and p is the pressure field. η_P is a new parameter whose role is to control the the strength of feedback stresses into the fluid. Now, the feedback force is a vector and the j^{th} component of the force is given by:

$$(\boldsymbol{\nabla}\cdot\underline{\underline{\boldsymbol{\sigma}}}_P)_j = \sum_i \frac{\partial}{\partial x_i}(\sigma_P)_{ij}, \tag{3.46}$$

where i runs over the directions x, y, z. A sample calculation for the x-component of the force is given by:

$$\frac{\partial \sigma_{P,xx}}{\partial x} + \frac{\partial \sigma_{P,yx}}{\partial y} + \frac{\partial \sigma_{P,zx}}{\partial z}, \tag{3.47}$$

where $\sigma_{P,xx} = f(r_{\text{P}})C_{xx}$. This is again expanded using the second order finite difference which gives:
x component polymeric force at (x, y, z):

$$\begin{aligned}\frac{\sigma_{P,xx}(x+\Delta x, y, z) - \sigma_{P,xx}(x-\Delta x, y, z)}{2\Delta x} &+ \frac{\sigma_{P,yx}(x, y+\Delta y, z) - \sigma_{P,yx}(x, y-\Delta y, z)}{2\Delta y} \\ &+ \frac{\sigma_{P,zx}(x, y, z+\Delta z) - \sigma_{P,zx}(x, y, z+\Delta z)}{2\Delta z}\end{aligned} \tag{3.48}$$

y component polymeric force:

$$\begin{aligned}\frac{\sigma_{P,xy}(x+\Delta x, y, z) - \sigma_{P,xy}(x-\Delta x, y, z)}{2\Delta x} &+ \frac{\sigma_{P,yy}(x, y+\Delta y, z) - \sigma_{P,yy}(x, y-\Delta y, z)}{2\Delta y} \\ &+ \frac{\sigma_{P,zy}(x, y, z+\Delta z) - \sigma_{P,zy}(x, y, z+\Delta z)}{2\Delta z}\end{aligned} \tag{3.49}$$

z component polymeric force:

$$\begin{aligned}\frac{\sigma_{P,xz}(x+\Delta x, y, z) - \sigma_{P,xz}(x-\Delta x, y, z)}{2\Delta x} &+ \frac{\sigma_{P,yz}(x, y+\Delta y, z) - \sigma_{P,yz}(x, y-\Delta y, z)}{2\Delta y} \\ &+ \frac{\sigma_{P,zz}(x, y, z+\Delta z) - \sigma_{P,zz}(x, y, z+\Delta z)}{2\Delta z}.\end{aligned} \tag{3.50}$$

Therefore, the magnitude of these feedback polymeric forces are controlled by varying the parameter η_P and also τ_P. The parameter L^2, also called the maximum extensible length of the polymer, is varied in order to achieve large stresses.

3.3.1 Multicomponent viscoelastic simulations

The goal of this thesis is to investigate the contact line motion in viscoelastic liquids that are surrounded by Newtonian components. In addition, many physical situations/applications arise where one of the components

is viscoelastic and the other component is Newtonian [52–55]. Therefore, we need a technique to control the viscoelasticity so that it can be "switched" on or off at specified regions. For this a smoothing function is formulated such that the viscoelasticity can be toggled between the multicomponent fluids. The form of the smoothing function is [51]:

$$f_{\pm}(\phi) = \left(\frac{1 \pm \tanh(\phi/\Delta)}{2} \right), \tag{3.51}$$

where $\phi = \frac{\rho_A(\boldsymbol{x}) - \rho_B(\boldsymbol{x})}{\rho_A(\boldsymbol{x}) + \rho_B(\boldsymbol{x})}$, Δ is a free parameter called the smoothing parameter which controls the thickness across the diffuse interface during which the polymeric stresses go to zero. The smoothing parameter is fixed by matching appropriately matching analytical solutions with the solutions obtained from the simulations. The above concepts can be illustrated using a simple example:

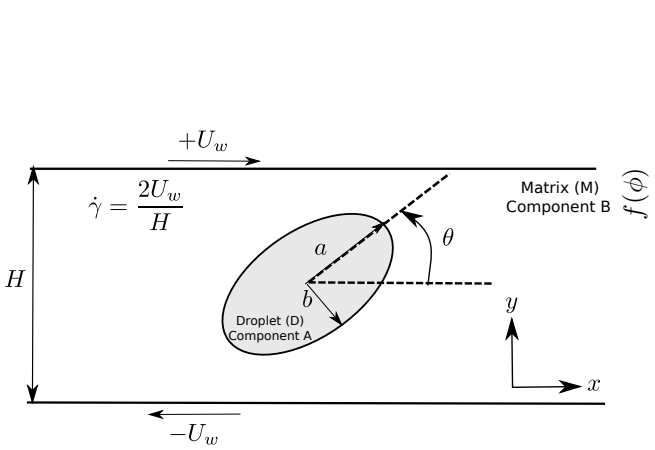

(a) Droplet in a solvent

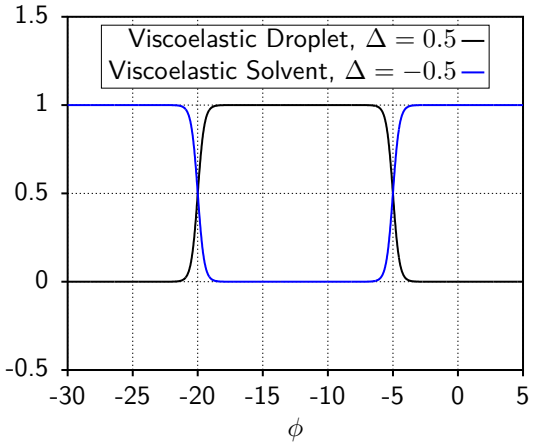

(b) Smoothing function, $|\Delta| = 0.5$

Figure 3.10: (a) A droplet subjected to a shear flow is shown. The **Droplet** is *Component-A* **rich** and *Component-B* **poor**, whereas, the **Matrix** is *Component-A* **poor** and *Component-B* **rich**. (b) The smoothing function $f_{\pm}(\phi)$ is plotted across the cross section of a droplet. It is seen that in case of a viscoelastic droplet the smoothing function peaks in the region corresponding to the droplet, whereas, it is zero in the region corresponding to the solvent. However, in case of a viscoelastic solvent, the smoothing function is unity in the region of solvent and zero inside the droplet. Therefore, the smoothing function is used to modulate the polymeric stresses in different regions of the simulation domain.

A confined droplet inside a channel is subjected to shear flow [3]. It is of interest to study (a) the steady state deformation of a viscoelastic droplet and (b) the steady state deformation of a Newtonian droplet inside a viscoelastic solvent. For the case of a viscoelastic droplet the polymeric stresses act only inside the droplet, and, for a viscoelastic solvent they act only inside the solvent. Therefore, it is beneficial if the polymeric stresses corresponding to $\underline{\underline{\boldsymbol{\sigma}}}_P$ can be modulated in the simulation domain depending on where the non-Newtonian components are present. By using the smoothing function we can achieve the modulation of the polymeric stresses across the simulation domain. From Figure (3.10), by changing the sign of Δ from positive to a negative value (maintaining the same magnitude), it is possible to simulate (a) and (b), respectively.

3.3.2 Viscosity ratios

Finally, in this section the concept of viscosity ratios are discussed. In chapter 4, most of the simulations and results are presented for the case of viscosity ratio, between the viscoelastic component and the Newtonian component, equal to 1. The concept is again illustrated using the case of the droplet, as shown in figure Figure (3.10). However, the concept can be extended to any multicomponent viscoelastic simulation.

[3] In the example where the Shan-Chen multicomponent method was discussed we used the α, β notation for the droplet and the surrounding (Figure (3.4)). Here, α and β are replaced by components A and B. Hence, it is just a change in the notation.

Viscosity of viscoelastic droplet

- The viscoelastic droplet's viscosity is the sum of the viscosity due to component A and the "dissolved" polymeric viscosity η_P. The relaxation time, and hence the dynamic viscosity, of the LB fluid is given by:

$$\rho c_s^2\Big(\tau_s - \frac{1}{2}\Big) = \eta_s = \eta_A f_+(\phi) + \eta_B f_-(\phi), \tag{3.52}$$

  where τ_s is determined by the spatial location. For the case of a viscoelastic droplet, the relaxation time inside the droplet is entirely determined by component A, whereas, in the Newtonian solvent the contribution to the relaxation time is dominated by component B. However, the values of τ for the individual components A and B must be chosen in order that $\eta_P + \eta_A = \eta_B$, in order that the viscosity ratio is set to 1.

Viscosity of viscoelastic droplet The same principle as for the case of a viscoelastic droplet holds here. Here, the viscosity of the viscoelastic solvent is set in such a way which ensures $\eta_B + \eta_{\mathrm{P}} = \eta_A$.

3.4 Conclusion

At the end of this chapter we have covered all the required aspects to simulate non-Newtonian flows using the LB formalism. In other words, we have introduced all the relevant concepts to solve the following equations [51]:

$$\text{Continuity}: \quad \partial_t \rho_\xi + \boldsymbol{\nabla}\cdot(\rho_\xi \mathbf{u}) = \boldsymbol{\nabla}\cdot\mathbf{D}_{\mathbf{S},\xi} \tag{3.53}$$

$$\text{Momentum}: \quad \rho[\partial_t \boldsymbol{u} + (\boldsymbol{u}\cdot\boldsymbol{\nabla})\boldsymbol{u}] = -\boldsymbol{\nabla}p + \boldsymbol{\nabla}\cdot\underline{\underline{\boldsymbol{\sigma}}}_S + \frac{\eta_p}{\tau_P}\boldsymbol{\nabla}\cdot\underline{\underline{\boldsymbol{\sigma}}}_P + \sum_\xi \boldsymbol{g}_\xi; \tag{3.54}$$

$$\text{Conformation tensor evolution}: \quad \partial_t \underline{\underline{\mathbf{C}}} + (\mathbf{u}\cdot\boldsymbol{\nabla})\underline{\underline{\mathbf{C}}} = \underline{\underline{\mathbf{C}}}\cdot(\boldsymbol{\nabla}\mathbf{u}) + (\boldsymbol{\nabla}\mathbf{u})^{\mathbf{T}}\cdot\underline{\underline{\mathbf{C}}} - \frac{\underline{\underline{\boldsymbol{\sigma}}}_{\mathbf{P}} - \mathbb{1}}{\tau_{\mathbf{P}}} \tag{3.55}$$

$$\text{Closure}: \quad \underline{\underline{\boldsymbol{\sigma}}}_P = f(r_{\mathrm{P}})\underline{\underline{\boldsymbol{C}}}. \tag{3.56}$$

Here, ρ_ξ is the density of the ξ-th component where $\xi \in \{A, B\}$ and $\rho = \sum_\xi \rho_\xi$ indicates the total density. $\boldsymbol{u}$ represents the velocity evaluated by taking into account both components A and B. p_ξ is the internal ideal pressure of component ξ, and the total pressure $p = \sum_\xi p_\xi$. The term $\sum_\xi \boldsymbol{g}_\xi$ takes into account the body force contributions coming from all the internal and external forces. The *internal* force in our model is the "Shan-Chen" interaction force which is a force experienced by each of the component ξ. An interaction parameter $\mathcal{G}$ is defined for this interaction. In addition, adjacent to the wall, the *external* force due to the wall on the component ξ is controlled through another interaction parameter $\mathcal{G}_{wall,\xi}$ which helps to control the wetting properties of component ξ (contact angle). The diffusion of one component into the other and the viscous stress tensor of the solvent (S) is [51]:

$$\boldsymbol{D}_{S,\xi} = \mu\Big[\Big(\boldsymbol{\nabla}p_\xi - \frac{\rho_\xi}{\rho}\boldsymbol{\nabla}p\Big) - \Big(\boldsymbol{g}_\xi - \frac{\rho_\xi}{\rho}\sum_\xi \boldsymbol{g}_\xi\Big)\Big] \tag{3.57}$$

$$\underline{\underline{\boldsymbol{\sigma}}}_S = \eta_S\Big(\boldsymbol{\nabla}\boldsymbol{u} + (\boldsymbol{\nabla}\boldsymbol{u})^{\mathrm{T}} - \frac{2}{3}\mathbb{1}(\boldsymbol{\nabla}\boldsymbol{u})\Big) + \eta_b\mathbb{1}(\boldsymbol{\nabla}\boldsymbol{u}), \tag{3.58}$$

where η_S is the shear viscosity of the and η_b refers to the bulk viscosity. μ refers to the mobility coefficient [4]. The reader should note that the dimensions of $\underline{\underline{\boldsymbol{\sigma}}}_P$ are not the dimensions of a stress tensor, rather, the dimensions of $\frac{\eta_P}{\tau_P}\underline{\underline{\boldsymbol{\sigma}}}_P$ together have the dimensions of a stress tensor. Following this, we discussed the methodology to evaluate the effect of the flow field on the dynamics of the conformation tensor.

Most importantly, we obtained the key parameters for simulating non-Newtonian flows using LB. The final list of parameters that will be used to simulate the moving contact line problem for non-Newtonian fluids are the following:

- Polymer relaxation time τ_P to control the relaxation time of the polymers;

[4] The implementation of the aforementioned equations has not been discussed in this chapter. The interested reader is referred to [51] and references therein.

- Maximum extensible length L^2 to control the flexibility of the polymer chains;
- Polymeric viscosity η_P to modulate the strength of the polymeric stresses;
- Smoothing parameter Δ to modulate the polymeric stresses across the simulation domain;
- Wall interaction parameter $\mathcal{G}_{\mathrm{wall},\xi}$ to control the microscopic wetting angle for the component ξ;
- Interaction parameter $\mathcal{G}$ to control the surface tension between the two components ξ and ξ';
- BGK relaxation time τ_ξ and ρ_ξ to control the dynamic viscosity η of the component ξ.

Chapter 4

Results

We concluded the previous chapter by identifying the key parameters for the FENE-P model, namely: the polymer relaxation time τ_P, the square of the maximum extension length L^2, polymeric viscosity η_P. Before we simulate the moving contact line problem for viscoelastic fluids it is necessary to benchmark the LB code against some standard non-Newtonian flows. We would like to perform the benchmark cases for two reasons: (a) to obtain a range of values for the aforementioned parameters , (b) to test the working of the LB code under various flow situations, for example: shear, extensional, and time dependent flows. We divide the benchmark cases based on single component and multicomponent flows. In the single component case we will simulate (a) Couette flow, (b) Steady elongational flow, (c) Oscillatory shear flow. In the multicomponent case we will simulate (a) the shear flow of a confined viscoelastic droplet in a Newtonian matrix (b) the shear flow of a confined Newtonian droplet in a viscoelastic matrix. Through these simulations we will obtain the range of parameters necessary for simulating the viscoelastic contact lines. Additionally, these benchmark cases will allow us to test the LB code under various flow conditions. Following this, we perform a benchmark case for the Newtonian contact line and obtain the scale separation parameter λ_s (defined in Chapter 2). Finally, we investigate the effects of viscoelasticity on the contact line motion for two cases: (a) symmetric wetting and (b) asymmetric wetting, and report our findings.

All the quantities used in the Lattice Boltzmann simulations have dimensions in the lattice units **lbu**.

4.1 Validation

In this section, the results of the benchmark cases performed to understand the features of the non-Newtonian rheology through LB simulations is presented. The following benchmark cases are studied and the non-Newtonian features which they exhibit is mentioned:

- **Couette flow**: Able to simulate the shear-thinning behavior of non-Newtonian fluids subjected to high non-dimensional shear rates.
- **Steady elongational flow**: Through this test it is shown that the LB simulation can simulate extensional flows.
- **Small amplitude oscillatory shearing**: Through this test it is shown that the LB simulations can simulate the viscous and the elastic behavior of a non-Newtonian fluid subjected to an oscillatory shear flow. To characterize the elastic and the viscous behavior of the non-Newtonian fluid, the material functions G' (elasticity modulus) and G'' are calculated.
- **Deformation of a droplet subjected to viscoelasticity and confinement**: We study two cases: (a) viscoelastic droplet (surrounded by a Newtonian matrix) and (b) Newtonian droplet surrounded by a viscoelastic matrix. We measure and quantify the deformation of the droplet as a function of Ca and compare it against standard experimental results.

For the study of the following test cases we closely follow the paper by Gupta *et al.* [51] and compare the results of the above simulations against their results.

4.1.1 Dilute polymer rheology for single-component flows

4.1.1.1 Master equation

Before we compare and benchmark the LB simulations we need establish a theoretical platform against which comparisons can be made. Therefore, in this section we briefly outline the main equations to be solved for the non-Newtonian flows.

In Chapter 3 we described the equation for the upper convected derivative of the conformation tensor $\underline{\underline{\boldsymbol{C}}}$ (Equation (3.29)). We will utilize this equation in steady state to obtain a master equation. Recalling from Chapter 3, the dimensionless polymeric feedback stress is given by [51]:

$$\underline{\underline{\boldsymbol{\sigma}}}_P = f(r_P)\underline{\underline{\boldsymbol{C}}} = \frac{L^2 - 3}{L^2 - \mathrm{Tr}(\underline{\underline{\boldsymbol{C}}})}. \tag{4.1}$$

Taking the trace of the above equation and rewriting the expression for feedback we get:

$$\underline{\underline{\boldsymbol{\sigma}}}_P = Z(\mathrm{Tr}(\underline{\underline{\boldsymbol{\sigma}}}_P))\underline{\underline{\boldsymbol{C}}}, \tag{4.2}$$

where $Z = \frac{L^2 - 3 + \mathrm{Tr}(\underline{\underline{\boldsymbol{\sigma}}}_P)}{L^2}$. Now, substituting $\underline{\underline{\boldsymbol{C}}} = \underline{\underline{\boldsymbol{\sigma}}}_P / Z$ in Equation (3.29) and on simplifying further we get [51]:

$$Z(\underline{\underline{\boldsymbol{\sigma}}}_P - \mathbb{1}) + \tau_p[\ \mathrm{D_t}\underline{\underline{\boldsymbol{\sigma}}}_P - \underline{\underline{\boldsymbol{\sigma}}}_P \cdot (\boldsymbol{\nabla u}) - (\boldsymbol{\nabla u})^T \cdot \underline{\underline{\boldsymbol{\sigma}}}_P - \underline{\underline{\boldsymbol{\sigma}}}_P \mathrm{D_t} \log Z\ ] = 0. \tag{4.3}$$

In Equation (4.3) D_t corresponds to the material derivative and $\mathbb{1}$ is the unitary matrix. In the upcoming cases we will use Equation (4.3) in steady state (Couette flow, steady elongational flow) as well as time dependent case (oscillatory shear rheology) to derive expressions for the following quantities:

$$\mathcal{S} = \sigma_{P,xy} \tag{4.4}$$

$$\mathcal{N} = \sigma_{P,xx} - \sigma_{P,yy}, \tag{4.5}$$

where $\mathcal{S}, \mathcal{N}$ are the polymeric shear stress and the first normal stress difference. Here, the x-axis is along the direction of the forcing applied and y-axis is perpendicular to it. Hence, the above definitions. These two quantities will be of importance to us throughout this chapter. Especially in the case of the non-Newtonian contact lines where the region near the contact line is a region of high shear stresses.

We now begin by simulating the Couette flow for the FENE-P model.

4.1.1.2 Case 1: Couette flow

In this section the steady shear flow is simulated in the presence of polymers inside the flow. The setup for the flow geometry is shown in Figure (4.1). Initially, an expression for the normal stress $\mathcal{N}$ and the shear stress $\mathcal{S}$ will be derived. Following this derivation, the results from the LB simulations for $\mathcal{N}$ and $\mathcal{S}$ will be compared against theory.

For theory we substitute in Equation (4.3) the following velocity field $\boldsymbol{u}(x, y)$:

$$\boldsymbol{u} = \begin{pmatrix} \dot{\gamma} y \\ 0 \\ 0 \end{pmatrix}, \tag{4.6}$$

where $\dot{\gamma} = \frac{2U_w}{L_y}$ (Figure (4.1)) is the constant shear rate. The tensor $\boldsymbol{\nabla u}$, for a shear flow, is given by the following matrix:

$$\boldsymbol{\nabla u} = \begin{pmatrix} \partial_x u_x & \partial_x u_y & \partial_x u_z \\ \partial_y u_x & \partial_y u_y & \partial_y u_z \\ \partial_z u_x & \partial_z u_y & \partial_z u_z \end{pmatrix} = \begin{pmatrix} 0 & 0 & 0 \\ \dot{\gamma} & 0 & 0 \\ 0 & 0 & 0 \end{pmatrix}. \tag{4.7}$$

where $\dot{\gamma}$ is the gradient of u_x in the direction normal to the shear. Once the flow has achieved steady state the components of $\underline{\underline{\boldsymbol{\sigma}}}_P$ cease to change with time and Equation (4.3) simplifies to:

$$Z(\underline{\underline{\boldsymbol{\sigma}}}_P - \mathbb{1}) + \tau_p[\ \cancel{\mathrm{D_t}\underline{\underline{\boldsymbol{\sigma}}}_P} - \underline{\underline{\boldsymbol{\sigma}}}_P \cdot (\boldsymbol{\nabla u}) - (\boldsymbol{\nabla u})^T \cdot \underline{\underline{\boldsymbol{\sigma}}}_P - \underline{\underline{\boldsymbol{\sigma}}}_P \cancel{\mathrm{D_t} \log Z}\ ] = 0 \tag{4.8}$$

$$Z(\underline{\underline{\boldsymbol{\sigma}}}_P - \mathbb{1}) + \tau_p[\ -\underline{\underline{\boldsymbol{\sigma}}}_P \cdot (\boldsymbol{\nabla u}) - (\boldsymbol{\nabla u})^T \cdot \underline{\underline{\boldsymbol{\sigma}}}_P\ ] = 0 \tag{4.9}$$

The above equations can be represented in the matrix form:

$$Z\begin{pmatrix}\sigma_{P,xx}-1 & \sigma_{P,xy} & 0\\ \sigma_{P,yx} & \sigma_{P,yy}-1 & 0\\ 0 & 0 & \sigma_{P,zz}-1\end{pmatrix}-\tau_p\left[\ \dot{\gamma}\begin{pmatrix}2\sigma_{P,yx} & \sigma_{P,yy} & 0\\ \sigma_{P,yy} & 0 & 0\\ 0 & 0 & 0\end{pmatrix}\ \right]=0. \tag{4.10}$$

Solving the above equation gives $\sigma_{P,yy}=\sigma_{P,zz}=1$ and then replacing $\sigma_{P,xx}-\sigma_{p,yy}$ with the first normal stress difference $\mathcal{N}$ (Equation (4.5)), $\sigma_{P,xy}$ with the polymeric shear stress $\mathcal{S}$ (Equation (4.4)) and $\dot{\gamma}\tau_p$ with Λ, we get the following set of equations for $\mathcal{N}$ and $\mathcal{S}$:

$$\Big(1+\frac{\mathcal{N}}{L^2}\Big)\mathcal{N} \quad =2\Lambda\mathcal{S}, \tag{4.11}$$

$$\Big(1+\frac{\mathcal{N}}{L^2}\Big)\mathcal{S} \quad =\Lambda. \tag{4.12}$$

The above two equations can be divided and rearranged to obtain a relation between the first normal stress difference and the polymeric shear stress, given by:

$$\mathcal{N}=2\mathcal{S}^2. \tag{4.13}$$

Substituting the relation for $\mathcal{S}$, from Equation (4.13) back into Equation (4.11), we obtain the following third degree polynomial equation for $\mathcal{S}$:

$$2\frac{\mathcal{S}^3}{L^2}+S-\Lambda=0. \tag{4.14}$$

This cubic equation can be solved exactly to obtain 1 real and 2 complex roots. The real root is given by:

$$\mathcal{S}(\Lambda,L)=2\Big(\frac{L^2}{6}\Big)\sinh\Big(\frac{1}{3}\mathrm{arcsinh}\Big(\frac{\Lambda L^2}{4}\Big(\frac{L^2}{6}\Big)^{-\frac{3}{2}}\Big)\Big), \tag{4.15}$$

and from Equation (4.13), we find the expression for $\mathcal{N}$ as:

$$\mathcal{N}(\Lambda,L)=2\Big(\frac{L^2}{6}\Big)\sinh^2\Big(\frac{1}{3}\mathrm{arcsinh}\Big(\frac{\Lambda L^2}{4}\Big(\frac{L^2}{6}\Big)^{-\frac{3}{2}}\Big)\Big). \tag{4.16}$$

Now that we know the mathematical expressions for $\mathcal{N}$ and $\mathcal{S}$ it is useful to plot their dependence on L, the maximum extensible length of the polymer (see Figure (4.2)). We see that as $L^2\to\infty$, known as the *Oldroyd-B* limit, the relation for $\mathcal{S}$ and $\mathcal{N}$:

$$\mathcal{S}\to\dot{\gamma}\tau_P, \tag{4.17}$$

$$\mathcal{N}\to 2\dot{\gamma}^2\tau_P^2=2\mathcal{S}^2. \tag{4.18}$$

where $\dot{\gamma}$ is the shear rate and τ_P is the polymer relaxation time. Equation (4.18) indicates a perfectly elastic behavior. For finite values of L^2, $\mathcal{S}$ and $\mathcal{N}$ both are below the *Oldroyd-B* limit.

Now, the simulation of a shear flow of a FENE-P fluid is simulated using the LB method and compared against theoretical predictions for $\mathcal{N}$ and $\mathcal{S}$. The numerical simulations are performed in a 3D domain and a cut-section is analyzed for the first normal stress difference and the shear stress. For this we adopt a cell of size $L_x\times H\times L_z=10\times 60\times 10$. Periodic boundary conditions are applied in the direction of the shear, and the bounce back rule is applied to the fluid population adjacent to both the top wall ($y=H$) and the bottom wall ($y=0$). The top and the bottom walls are moved with opposite velocities, of magnitude U_w. Polymer relaxation times in the following range are used: $10^3\leq\tau_p\leq 10^5$, and, shear rates in the range: $10^{-6}\leq\dot{\gamma}\leq 10^{-2}$, are used. The numerical simulations were conducted for 2 different maximum extensible lengths of the polymer: $L^2=10^2, 10^4$ and a polymeric viscosity of $\eta_P=0.136$ is used.

We normalize the polymeric shear stress $\mathcal{S}$ by it's value in the *Oldroyd-B* limit to observe the departure of the polymeric fluid from elastic behavior. The result of the $\mathcal{N}$ and the $\mathcal{S}$ for the case of the shear flow is plotted in Figure (4.3).

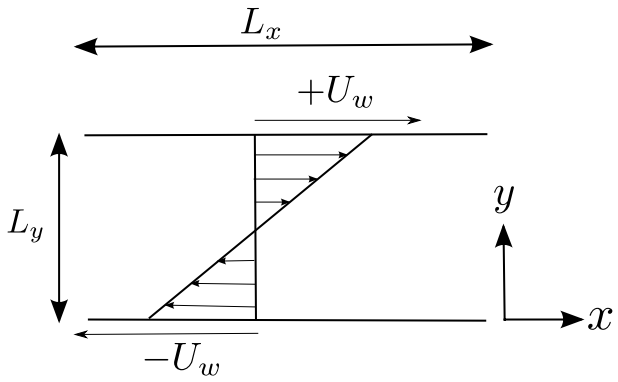

Figure 4.1: In this figure the a cut section of the 3 dimensional flow geometry for the Couette flow is plotted. The simulation domain contains top and the bottom walls which shear the fluid in opposite directions with the velocity of magnitude U_w. The normal direction direction is denoted by z and the flow domain is periodic in the x-direction.

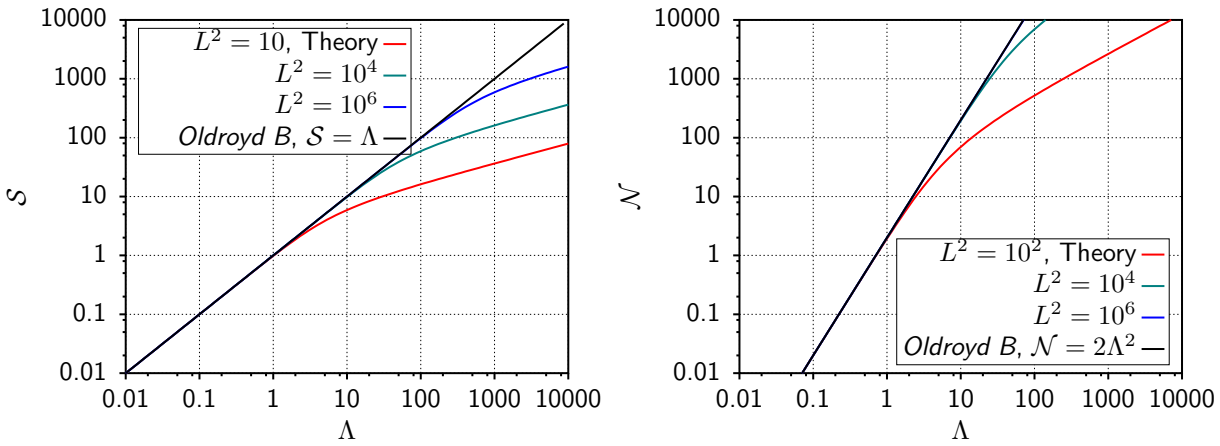

(a) Shear stress

(b) Normal Stress

Figure 4.2: The $\mathcal{S}$ and $\mathcal{N}$ obtained from Equation (4.15) and Equation (4.16) respectively, are plotted against the non-dimensional shear rate ($\Lambda = \dot{\gamma}\tau_p$) for different values of maximum polymer extension lengths of L^2.

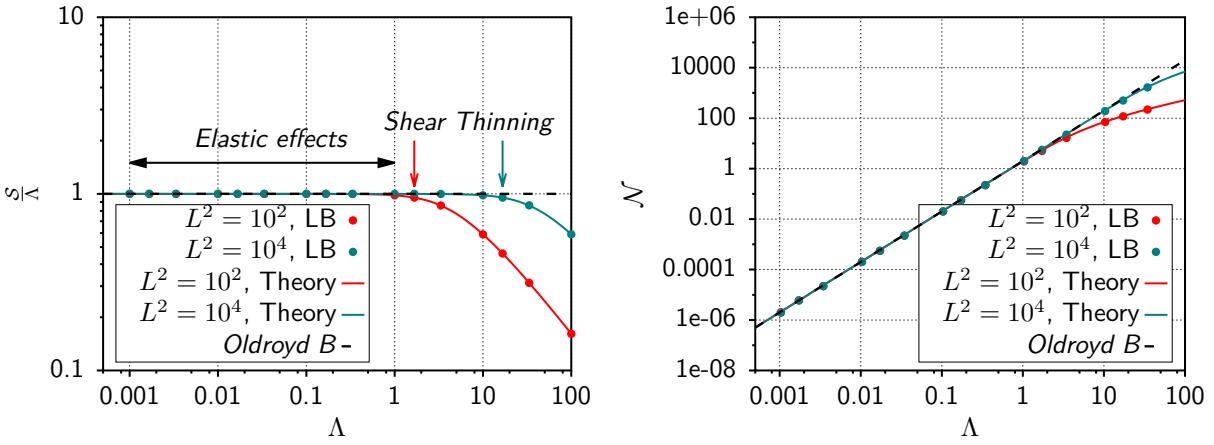

(a) Shear stress

(b) Normal stress

Figure 4.3: $\mathcal{S}$ (polymeric shear stress) and $\mathcal{N}$ (first normal stress difference) obtained from Lattice Boltzmann (LB) is plotted against non-dimensional shear rate ($\Lambda = \dot{\gamma}\tau_p$) for two different values of maximum polymer extension lengths of $L^2 = 10^2,\ 10^4$. The simulation results are compared against the theoretical expressions for $\mathcal{N}$ (Equation (4.16)) and $\mathcal{S}$ (Equation (4.15)) obtained in the section on shear flow. As seen from (a) and (b), $\mathcal{S}$ and $\mathcal{N}$ depart from the *Oldroyd-B* limit after crossing a certain Λ. This exhibits the onset of shear thinning. A smaller L^2 exhibits shear thinning earlier in comparison with a larger L^2. The above plots can be reproduced using the test `R237_STEADY_COUETTE_FLOW` with the help of the gnuplot script `plot_shear_normal_stress.gnu`. The simulations for different L^2 and Λ is handled by the script `rxx.sh` and is registered in gitlab as `ISSUE #247`. The plots can be found in the folder `final_plots`.

Observations

- Firstly, from Figure (4.3), we observe that there is an excellent agreement for both $\mathcal{N}$ and $\mathcal{S}$ obtained from LB simulations and that predicted from the theoretical analysis, see Equation (4.16) and Equation (4.15), for ranges of non-dimensional shear Λ ranging from 10^{-3} to 100.
- The shear thinning behavior is captured by the LB model which is characterized by decreasing polymeric shear stress and the normal stress with increasing Λ. In addition, we observe from Figure (4.3) that as the flexibility of the polymer denoted by the parameter L^2 is increased, the onset of shear thinning effects is delayed w.r.t Λ.
- Finally, the response of the fluid to an applied shear stress can be divided into 2 regimes: (a) *elastic*, and, (b) *purely thinning* regimes. In the elastic regime, the polymeric shear stress increases linearly with Λ, and, the first normal stress difference increases quadratically with Λ. However, after Λ crosses a critical value, the increase in the polymeric shear stress is no longer linear and follows an increase depending on the flexibility of the polymer.

Hence, the simple shear flow has been simulated and the $\mathcal{N}$ and the polymeric shear stress $\mathcal{S}$ have been validated against the corresponding expressions from the FENE-P model. Finally, the model is able to capture the shear thinning effects, and, through this, the elastic regime can be separated from the shear thinning regime.

4.1.1.3 Case 2: Steady elongational Flow

The uniaxial elongational flow is relevant to many polymer processing applications like injection molding and fiber spinning. The velocity field in a steady elongational flow is given by the velocity vector:

$$\boldsymbol{u} = \begin{pmatrix} -\frac{\dot{\epsilon}}{2}x \\ -\frac{\dot{\epsilon}}{2}y \\ \dot{\epsilon}z \end{pmatrix} \tag{4.19}$$

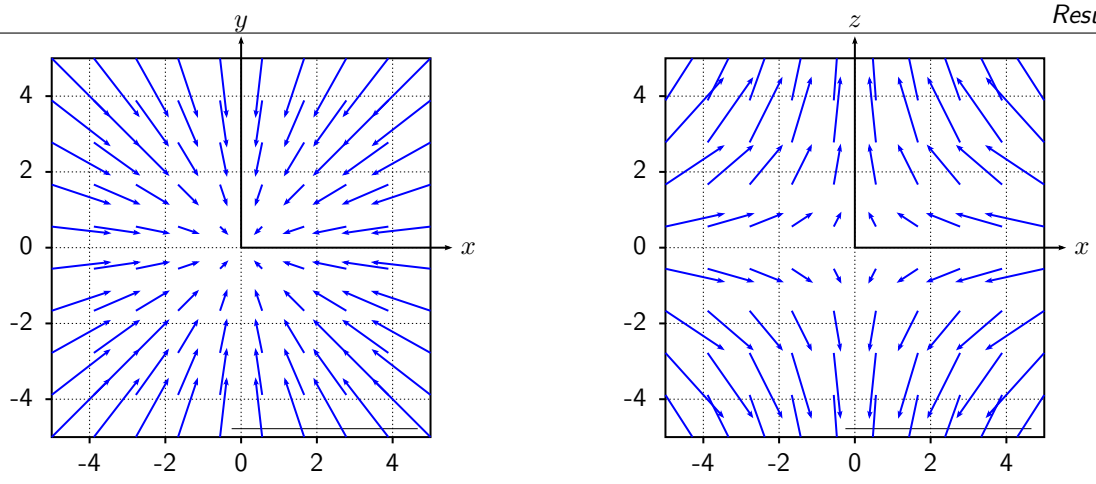

(a) xy plane (b) xz plane

Figure 4.4: The velocity vector field in the (a) xy and the (b) xz plane for an elongational flow as described by Equation (4.19) is plotted here. A strain rate magnitude of $\dot{\epsilon} = 0.5$ is used.

where $\dot{\epsilon}$ is the elongational rate. The velocity field as given by Equation (4.19) is visualized in Figure (4.4). From the Figure (4.4) it is clear that in the xy plane the flow tends to converge towards the point $(0, 0)$, whereas, in the xz plane the flow indicates a stretching along the z-direction. The velocity field can now be substituted into Equation (4.3) to obtain the polymeric stresses as a function of the non-dimensionless elongation rate $\Lambda_e = \tau_P \dot{\epsilon}$, where τ_P is the relaxation time of the polymer. From this, we derive a measure for the polymeric viscosity when subjected to a purely extensional flow.

We now substitute the elongational velocity field given by Equation (4.19) and substitute it in Equation (4.3). The equation can be further simplified in terms of the following 3 terms [51]:

$$\begin{aligned} D &= \sigma_{P,zz} - \sigma_{P,xx}, \\ T &= \mathrm{Tr}(\underline{\underline{\boldsymbol{\sigma}}}_P) - 3, \\ \Lambda_e &= \dot{\epsilon}\tau_P, \end{aligned}$$

where Λ_e is the non-dimensional elongation rate. Finally, we obtain a quadratic equation in terms of the non-dimensional elongation rate Λ_e:

$$2L^2 D\Lambda_e^2 + \Big[-4D^2 + (L^2 - D - 3)(D + 3)\Big]\Lambda_e + \frac{2D^3}{L^2} - (L^2 - D - 3)D = 0. \tag{4.20}$$

where $D = \sigma_{P,zz} - \sigma_{P,xx}$, L^2 is the maximum extension length squared. As can be seen from Equation (4.20), for the sake of simplicity in solving, the equation is expressed as a quadratic in terms of Λ_e rather than a cubic in terms of D and $\Lambda_e = \dot{\epsilon}\tau_P$ is the non-dimensional elongation rate. Further, using Equation (4.20) we find the solutions for Λ_e given by:

$$(\Lambda_e)_\pm = \frac{D}{L^2} + \frac{(L^2 - (D + 3))}{4DL^2}\Big(-(D + 3) \pm \sqrt{9D^2 + 6D + 9}\Big). \tag{4.21}$$

Now, the solution to Equation (4.21) are found in two limiting cases: (a) $D \to 0$, and, (b) $D \to \infty$. These two cases correspond to lowest and highest extensions of the polymers in the elongational flow.

1. $D \to 0$:
   After simplification we find that $\lim_{D\to 0}(\Lambda_e)_- \to \infty$, and hence, we choose the solution as limit $D \to 0$, which is given by:
   $$(\Lambda_e)_+ = \frac{D}{3} + \mathcal{O}(D^2). \tag{4.22}$$

It is seen that the term $D = \sigma_{P,zz} - \sigma_{P,xx}$ does not depend on the L^2. Therefore, for sufficiently small Λ_e the behavior of all polymers is similar.

2. $D \to \infty$:
   In the limit $D \to \infty$ we find:
$$(\Lambda_e)_- = \frac{D}{2L^2} + \mathcal{O}(\frac{1}{D}). \tag{4.23}$$
   where the difference in the elongational stresses $D = \sigma_{p,zz} - \sigma_{p,xx}$ depends on maximum extensible length squared of the polymer L^2 or the flexibility of the polymer, when Λ_e is approaches large magnitudes. Physically, high difference in stresses D can be achieved for the following two cases:

   - when the polymer relaxes very slowly in comparison to the applied elongational rate $\dot{\epsilon}$
   - when the polymer relaxes fast but the applied elongational rate $\dot{\epsilon}$ is very high.

Therefore, solutions to Equation (4.21) has two branches, namely: (a) the positive branch ($\Lambda_{e,+}$), and, (b) the negative branch ($\Lambda_{e,-}$). Further, when $\Lambda_e \ll 1$ the solution is $\Lambda_{e,+}$, however, when $\Lambda_e \gg 1$ the solution is the negative branch $\Lambda_{e,-}$. The solution branches are plotted in Figure (4.5) for the case of the maximum extensible length square of the polymer $L^2 = 10^4$. To quantify the polymeric stress difference D generated due to an extensional flow we define the *elongational viscosity* η_e as:

$$\eta_e = \frac{\eta_P}{\tau_P}\frac{D}{\dot{\epsilon}}, \tag{4.24}$$

where η_P is the polymeric viscosity. Therefore, according to the solution of Equation (4.21) the ratio of the *elongational viscosity* η_e to the polymeric viscosity η_P simplifies to:

$$\frac{\eta_e}{\eta_P} = \frac{1}{\tau_P}\frac{D}{\dot{\epsilon}} = \begin{cases} 3 & \dot{\epsilon}\tau_P \ll 1 \\ 2L^2 & \dot{\epsilon}\tau_P \gg 1. \end{cases} \tag{4.25}$$

Now, we describe the LB simulation methodology to obtain the ratio of extensional viscosity to the polymeric viscosity. The numerical simulations are carried out in a 3D domain of size $L_x \times L_y \times L_z = 20 \times 20 \times 20$. Periodic conditions are applied in all three directions. The elongational strain amplitude was varied in the range of $10^{-5} \leq \dot{\epsilon} \leq 10^{-2}$ and the polymeric relaxation time was varied from $10^3 \leq \tau_P \leq 10^5$. The simulations were conducted for 3 different finite extensibility lengths of the polymers, $L^2 = 10,\ 10^2,\ 10^4$. The polymeric viscosity is maintained to a value $\eta_P = 0$. All the results presented were obtained only after the simulation has reached steady state. The polymeric stresses $\sigma_{P,zz}$ and σ_{xx} are subtracted at a given location (x, y, z) in the simulation domain for different Λ_e and they are divided by the applied $\dot{\epsilon}$ and plotted for different L^2, see Figure (4.5b). In addition, we also see that the Figure (4.5a) faithfully follows the positive and the negative branches for different values of D.

From Figure (4.5), for a fixed polymeric relaxation time (τ_P) and polymer flexibility (L^2), it can be concluded that the for small $\dot{\epsilon}\tau_P$ the viscosity ratio has a constant value of 3. However, increasing $\dot{\epsilon}$ the viscosity ratio increases and plateaus to a new stable value. Another interesting property of the model allows the viscosity ratio to diverge when the polymer flexibility is increased. This can be concluded from Equation (4.25). In addition, this is logically consistent with the fact that higher flexibility of the polymers allows for higher stresses to be developed, which in turn, allows for a larger value of D.

4.1.1.4 Case 3: Small amplitude oscillatory shearing

The viscoelastic response of soft materials is characterized with the help of oscillatory rheology. In this section, a numerical *small amplitude oscillatory shear experiment* is carried out to obtain the *loss modulus* and *storage modulus* of a viscoelastic fluid with the help of LB. The small amplitude implies that the amplitude of the shear allows us to probe the viscoelastic fluid in the linear viscoelastic regime and, numerically, that translates into $L \gg 1$. Firstly, the theory is presented for the case of small amplitude oscillatory shear rheology using Equation (4.3). The velocity field is given by the following matrix:

$$\boldsymbol{u} = \begin{pmatrix} \dot{\gamma}(t)y \\ 0 \\ 0 \end{pmatrix}. \tag{4.26}$$

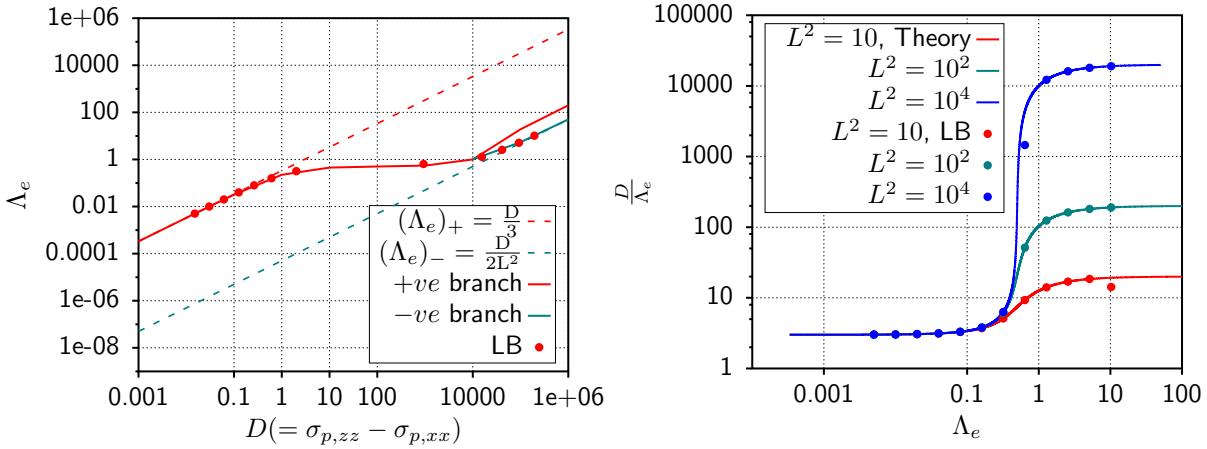

(a) solution branches for $L^2 = 10^4$

(b) $\frac{\eta_e}{\eta_P}$ for varying L^2

Figure 4.5: In (a) the positive and negative branches of the solutions to Equation (4.21) are compared against the LB simulations. and the extensional viscosity as a function of the applied elongational stress ϵ. The plot (b) can be reproduced using the test `R237_STEADY_EXTENSIONAL_FLOW_FENEP` with the help of the gnuplot script `ext_viscosity_compare.gnu`. The simulations for different L^2 and Λ_e is handled by the script `rxx.sh` and is registered in gitlab as `ISSUE #246`. The plots can be found in the folder `final_plots`.

The above sinusoidal velocity field can be substituted into Equation (4.3) to perform further calculations using the tensor notation. However, we would like to approach this problem using a scalar argument using the Maxwell mode introduced in Chapter 2. The details of the tensor calculation is provided in [51]. In the Maxwell model the equation for the spring dashpot model was introduced using Equation (2.28), where σ corresponded to the stress and ϵ corresponded to the strain. Substituting a sinusoidal signal for the stress σ and ϵ of the form:

$$\sigma(t) = \sigma_0 \exp(i\omega\tau), \tag{4.27}$$

$$\epsilon(t) = \epsilon_0 \exp(i\omega\tau), \tag{4.28}$$

where σ_0, ϵ_0 correspond to the amplitude of the stress and strain signal, ω corresponds to the frequency of forcing and τ corresponds to the time scale introduced by the spring dashpot model (Equation (2.28)). Substituting the above signal in Equation (2.28) and simplifying, we get:

$$k(i\omega)\epsilon_0 \exp(i\omega t) = \Big(i\omega + \frac{1}{\tau}\Big)\sigma_0 \exp(i\omega t). \tag{4.29}$$

A further simplification by defining a complex modulus E^*:

$$E^* = \frac{\sigma_0}{\epsilon_0} = \frac{k(i\omega)}{i\omega + \frac{1}{\tau}},$$

and obtaining the above equation in a complex form gives:

$$E^* = \frac{k\omega^2\tau^2}{1+\omega^2\tau^2} + i\frac{k\omega\tau}{1+\omega^2\tau^2}.$$

Finally, we designate the quantity $\frac{E^*}{k}$ as G^*. Therefore,

$$G^* = G' + iG'' = \frac{\omega^2\tau^2}{1+\omega^2\tau^2} + i\frac{\omega\tau}{1+\omega^2\tau^2}.$$

The quantity G' is called the *storage modulus* and term G'' is called the *loss modulus*, as was described in Chapter 2. In addition, the term τ is equal to the polymer relaxation time τ_P. Therefore, we have derived a storage modulus and loss modulus through the Maxwell model and this will be compared against the LB simulations.

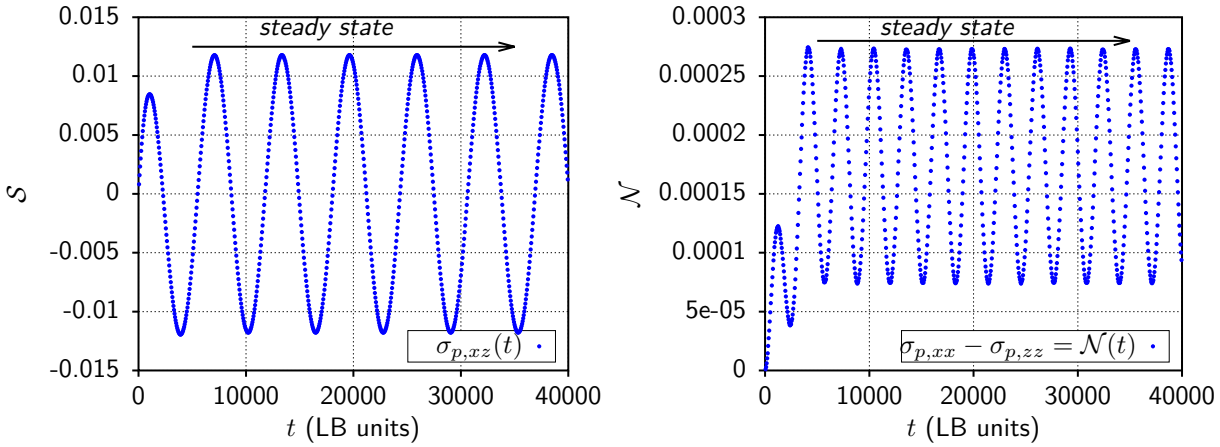

(a) Shear stress (b) Normal Stress

Figure 4.6: Shear and normal stress signal obtained from the LB simulations as a function of time for the case of a small amplitude oscillatory shear. This plot can be reproduced using the test `R237_SAOS_COUETTE_FLOW` with the help of the gnuplot script `shear_stress_plot.gnu` and `normal_stress_plot.gnu`. The simulations for different ω and τ_p is handled by the script `rxx.sh` and is registered in gitlab as `ISSUE #245`. The plots can be found in the folder `final_plots`.

Now the details of the simulations are described. The simulation is performed in a 3D domain of size $L_x \times L_y \times L_z = 10 \times 60 \times 10$. As before, the boundary conditions for the fluid are *periodic* in the direction of the shear and *bounce back* boundary condition for the fluid is applied at the walls. The oscillatory shear flow profile is generated by prescribing the velocities at the top and bottom wall whose velocity directions are opposite and the magnitude is given by $u_x = \dot{\gamma}(t)y = \frac{2U_w}{H}\cos(\omega t)y,\ u_y = 0,\ u_z = 0$. The frequency of oscillation ω is varied in the range $10^{-6} \leq \omega \leq 10^{-3}$ and the polymer relaxation time τ_P is changed in the range of $10^3 \leq \tau_P \leq 10^6$. The feedback of the polymer into the fluid is 0 which is controlled by setting the polymeric viscosity $\eta_P = 0.0$. To calculate the *storage* and the *loss* modulus it should be ensured that both $\mathcal{S}$ and $\mathcal{N}$ have acquired a steady signal. This can be ensured by making sure that the time required for the growth of the boundary layer is smaller than the time at which the velocities change direction at the walls. This can be mathematically formulated as:

$$\tau_{\nu_s} \sim \frac{H^2}{\nu_s}, \tag{4.30}$$

$$\tau_{\nu_s} \ll \frac{1}{\omega}, \tag{4.31}$$

where ν_s is the kinematic viscosity, H is the separation between the walls, τ_{ν_s} gives the time required for momentum diffusion from the walls to the channel and ω is the frequency of the shear signal $\dot{\gamma}(t)$. Hence, the height of the channel H is adjusted in such a way so as to satisfy the criteria given by Equation (4.31). Now, from the LB simulations, the polymeric shear stress signal $\mathcal{S}$ and the normal stress $\mathcal{N}$, as obtained from the LB simulations are plotted in Figure (4.9). From the $\mathcal{S}$ the real and the imaginary components of the viscosity are obtained to finally calculate G' and G''. The method to calculate the real (η') and imaginary components (η'') of the viscosity is by starting off from the expression for $\mathcal{S}(t)$ given by [51]:

$$\mathcal{S}(t) = \dot{\gamma}\eta'\cos(\omega t) - \dot{\gamma}\eta''\sin(\omega t).$$

Multiplying the above equation by $\cos(\omega t)$ (or $\sin(\omega t)$) on both sides of the equation and averaging over the period of a signal from $t = 0$ to $t = \frac{2\pi}{\omega}$ gives the following:

$$\int_0^{\frac{2\pi}{\omega}} dt\ \mathcal{S}(t)\cos(\omega t) = \int_0^{\frac{2\pi}{\omega}} dt\ \eta'\cos^2(\omega t) - \int_0^{\frac{2\pi}{\omega}} dt\ \eta''\cos(\omega t)\sin(\omega t)^{0}. \tag{4.32}$$

The terms corresponding to cross terms of the nature $\sin(\omega t)\cos(\omega t)$ are canceled out. Therefore, finally we

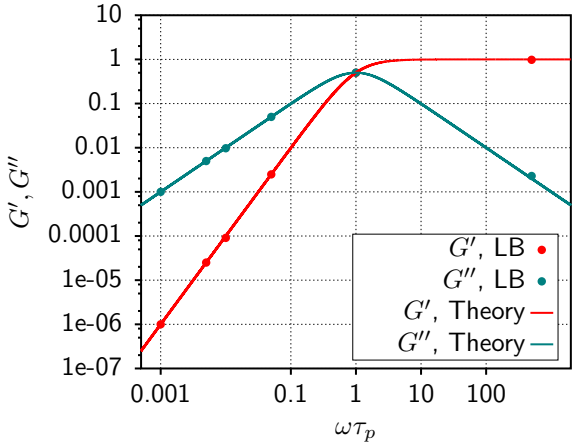

Figure 4.7: The elasticity modulus (G') and the loss modulus (G'') obtained through LB simulations is plotted as a function of the product of the frequency of wall oscillation and the relaxation time of the polymer. The results obtained from the LB simulations are compared against the corresponding theoretical predictions for the elasticity and loss modulus as a function $\omega\tau_p$, respectively. This plot can be reproduced using the test `R237_SAOS_COUETTE_FLOW` with the help of the gnuplot script `Gp_Gpp_compare.gnu`. The simulations for different ω and τ_p is handled by the script `rxx.sh` and is registered in gitlab as `ISSUE #245`. The processing of the normal and shear stress signal is performed using the C code `Gp_Gpp.c`. The plots can be found in the folder `final_plots`.

have expression to obtain η' and η'', and hence also G' and G'', from the simulations:

$$\eta' = \frac{2\langle \mathcal{S}(t)\cos(\omega t)\rangle}{\dot{\gamma}^{(0)}}, \quad \eta'' = \frac{2\langle \mathcal{S}(t)\sin(\omega t)\rangle}{\dot{\gamma}^{(0)}}, \tag{4.33}$$

where the $\langle\cdot\rangle$ represents the integral of the signal over time t.

Finally, in Figure (4.7), the comparison of G', G'' from the LB simulations with that from the theoretical expressions lead to an excellent matching. This implies that the LB simulation can successfully simulate polymers under time varying conditions. In addition, a measure of the elasticity of the polymer can be obtained through the calculation of the *storage* and of the *loss* modulus.

4.1.2 Dilute polymer rheology for multicomponent flows

In the previous section single-component flows involving non-Newtonian rheology was simulated and bench marked against standard non-Newtonian rheological flows. However, since the dynamic contact line problem involves the participation of 2 fluid components it is required to understand how the LB simulations perform in simulating multicomponent flows, where one of the component is viscoelastic in nature. In addition, it should be remembered that in LB, the multicomponent nature of the fluids are simulated using the *Shan-Chen* (from here on SC) interaction model. The SC model introduces a diffuse interface between two components which is characterized by a layer of thickness ζ. Then, the question arises as to what would be the optimal thickness ζ of the diffuse interface, such that, the results obtained from the *Shan Chen* model matches the theoretical predictions? The answer to this lies in controlling the tunable parameters: (a) G - controls the interaction strength between two components, (b) mobility μ - controls the diffusion of one component into another. In addition, the introduction of viscoelasticity introduces an additional parameter ϕ which regulates the viscoelastic nature of the diffuse interface. Therefore, in order to obtain an estimate for the parameters: μ, G and ϕ, it is important that the LB simulation is bench marked for the case of a multicomponent flow [51]. This exercise provides a platform on which the simulation for the non-Newtonian contact lines can be conducted.

Droplet deformation in a confined channel is chosen for testing the multicomponent simulation in the presence of a viscoelastic component. Droplet dynamics in a confined channel, apart from being useful in industrial applications, has been studied extensively and reviewed for the case of Newtonian and non-

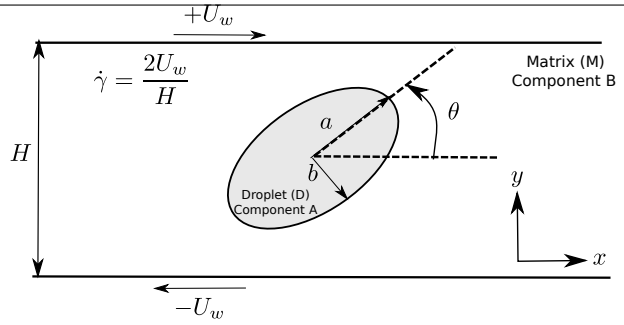

Figure 4.8: In this figure the schematic of the flow geometry for the confined droplet is shown. The simulation domain is 2 dimensional and the top and the bottom walls, separated by H, move in opposite directions with a velocity of magnitude U_w, creating an effective shear rate of $\dot{\gamma} = \frac{2U_w}{H}$. The **Droplet** is denoted by **Component A** and the **Matrix** is denoted by **Component B**. The component A is assigned a viscosity of η_A and the matrix is assigned a viscosity of η_B. The polymer is added to the component A (or component B) in terms of a shear viscosity η_P such that the viscosity ratio between the Droplet and the Matrix is given by $\frac{\eta_A+\eta_P}{\eta_B}$ (or $\frac{\eta_A}{\eta_B+\eta_P}$). The shape of the droplet is assumed to be ellipsoidal and hence allowing for the definition of a major and minor axis of the ellipse whose lengths are denoted by $\boldsymbol{a}$ and $\boldsymbol{b}$, respectively.

Newtonian fluids. Hence, it has been chosen as the reference case for studying the performance of LB code. In this section, two different cases of droplet deformation will be considered and compared, namely [51]:

- Newtonian droplet inside a viscoelastic matrix
- Viscoelastic droplet inside a Newtonian matrix.

The geometry for the flow is shown in Figure (4.8). Two measures are introduced to understand the deformation of the confined droplet. They are the following:

- Deformation parameter D: The deformation parameter D is given by the ratio:

$$\mathcal{D} = \frac{a-b}{a+b}, \tag{4.34}$$

  where a and b are the droplet semi-axes.

- Orientation angle θ: The orientation angle θ is the angle between the shear flow direction and major semi-axes. This is illustrated in Figure (4.8).

Both the deformation parameter $\mathcal{D}$ and the orientation angle θ is measured as a function of the capillary number Ca, whose definition is given by [51]:

$$Ca = \frac{\dot{\gamma} R \eta_M}{\gamma} \tag{4.35}$$

where $\dot{\gamma}$ is the shear rate, R is the effective radius of the droplet, η_M is the viscosity of the matrix (Component B) and γ is the surface tension between the fluid components in Component A and Component B. This definition of a Ca gives the balance between the viscous forces, acting on the effective surface area of the droplet, and the surface tension forces acting to stabilize any deformations. Deformation in an unconfined droplet as a function of the Ca has been derived by Taylor, which is given by [56]:

$$\mathcal{D} = \frac{19\chi + 16}{16\chi + 16} Ca, \tag{4.36}$$

where $\chi = \frac{\eta_D}{\eta_M}$ represents the viscosity ratio between the droplet and the matrix. However, the simulation performed in LB will be for a confined droplet. Hence, effects of confinement on the droplet deformation have to be included in Equation (4.36). This case has been studied by Shapira and Haber who provided

correction terms to the deformation which is $\mathcal{O}(Ca)$. The expression is for the deformation of the droplet under confinement is given by [57]:

$$\mathcal{D} = \frac{19\chi + 16}{16\chi + 16}\left[1 + C_{sh}\frac{2.5\chi + 1}{\chi + 1}\left(\frac{R}{H}\right)^3\right]Ca, \tag{4.37}$$

where C_{sh} is a numerical factor accounting for the distance between the center of the droplet to the wall and R is the effective radius of the droplet. For the case of a droplet placed halfway in between the plate the value of C_{sh} is 5.6996. In addition, the expression for θ, orientation angle, as a function of Ca as derived by Maffetone and Minale [58] is given by:

$$\theta(Ca) = \frac{1}{2}\arctan\left(\frac{f_1}{Ca}\right) \tag{4.38}$$

where f_1 and it's associated expressions are listed below:

$$\begin{cases} f_1 &= \frac{40(1+\chi)}{(3+2\chi)(16+19\chi)(1+C_{sh}f_{1c}(\frac{R}{H})^3)}, \\ f_{1c} &= \frac{1+2.5\chi}{1+\chi} - f_{2c}, \\ f_{2c} &= -\frac{10-9\chi}{12+\chi}, \end{cases} \tag{4.39}$$

where χ is the viscosity ratio between the droplet and the matrix, C_{sh} is a constant determined by the relative position of the droplet center with respect to the wall value (equal to 6.6996).

Hence, now that the relevant parameters D and θ, corresponding to the deformation and the orientation of the droplet, have been defined the simulation details will be outlined.

Simulation Details A droplet of radius $R = 30$ grid nodes is initialized in the center of a 2 dimensional flow domain. The dimensions of the flow domain are chosen to be $L_x \times H \times L_z = 288 \times 128 \times 1$, where the flow is periodic in the x-direction and bounded by walls in the y-direction (also the direction of shear). A schematic is shown in Figure (4.8). The densities of the two components are initially chosen to have the values: $\rho_1 = 2.0,\ \rho_2 = 0.1$ and interaction parameter value of $\mathcal{G} = 1.5$. The following combination of ρ_1, ρ_2 and $\mathcal{G}$ is used to obtain the magnitude of surface tension γ through a standard *Laplace* test through which we obtain the value of γ=0.09. The shear viscosity of the droplet and the matrix component is set to be equal to $\eta_D = \eta_M = 1.74$, where the polymer can be dissolved either inside the droplet or inside the matrix. Finally, neutral wetting properties are chosen for the two components at the walls $y = 0$ and $y = H$, which implies that a droplet initialized with a suitable combination of $\rho_1,\ \rho_2$ and $\mathcal{G}$ will achieve a contact angle of 90^o in equilibrium. With regards to the non-Newtonian effects, either the matrix or the droplet is made viscoelastic with polymer relaxation times of $\tau_p = 2000,\ 4000$ and a maximum extensibility of $L^2 = 10^4$. Once the droplet is initialized at the center of the channel a shear flow field is applied on the droplet with the velocity profile: $u_x = \dot{\gamma}y,\ u_y = 0,\ u_z = 0$, through the top and bottom walls. The simulation is run for approximately 5×10^5 time steps for the flow to reach steady state. Following this the *deformation* and the *orientation* of the droplet are measured and used for compared for the cases of different polymer relaxation times τ_P.

4.1.2.1 Newtonian droplet in a viscoelastic matrix

In this case a Newtonian droplet is embedded inside a visco-elastic fluid whose viscosity ratio and the polymeric concentration is:

$$\chi = \frac{\eta_D}{\eta_M} = \frac{\eta_A + \eta_P}{\eta_B} = 1.0, \quad \frac{\eta_P}{\eta_P + \eta_A} = 0.4, \tag{4.40}$$

where $\eta_D = \eta_M = 1.74$ corresponds to the dynamic viscosities of the droplet and the matrix component, respectively, and the polymeric viscosity is set to a value of $\eta_P = 0.6993$. It is important to quantify the effects of the viscoelastic matrix, and for this the *Deborah Number* is introduced whose definition is given by [51]:

$$De = \frac{\mathcal{N}R}{2\gamma Ca^2}, \tag{4.41}$$

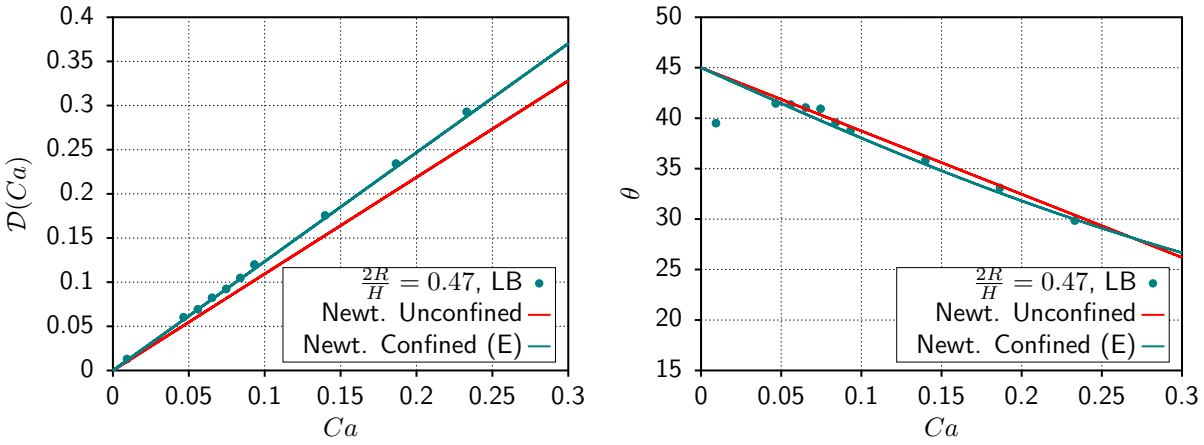

(a) $\mathcal{D}$ (b) θ

Figure 4.9: The steady deformation parameter $\mathcal{D}$ as a function of Ca for a Newtonian droplet inside Newtonian solvent is plotted in Figure (a). The confinement ratio of the droplet is given $\frac{2R}{H} = 0.47$, and, the viscosity of the droplet and the matrix are equal. $\mathcal{D}$ from the LB simulations are compared against theory. The $\mathcal{D}$ for an unconfined droplet is given by *Newt. Unconfined* (Equation (4.36)), and, $\mathcal{D}$ for a confined droplet is given by *Newt. Confined* (Equation (4.37)). In (b) the steady state orientation angle of the droplet is plotted as a function of Ca. Similar to (a) the droplet is compared against the steady state orientation angle obtained from *Newt. Unconfined* and *Newt. Unconfined*.

where $\mathcal{N}$ is the first normal stress difference generated in a simple shear flow (Equation (4.18)), R is the effective radius of the droplet, γ is the surface tension and Ca is the capillary number as defined in Equation (4.35). Equation (4.41) can be recast into a form which compares the timescale introduced by the polymer and the droplet [51]:

$$De = \frac{\tau_P}{\tau_{em}} \frac{\eta_P}{\eta_M}, \tag{4.42}$$

where $\tau_{em} = \frac{R\eta_M}{\gamma}$ and the definition of the first normal stress difference in the *Oldroyd limit* (Equation (4.18)) is used. From Equation (4.42), it can be seen that De is dependent on the ratio of the timescale of the emulsion and the polymer relaxation time, τ_P [51]. We would like to digress for a moment and clarify the difference between the Deborah number De and the Weissenberg number Wi (introduced in Section (2.4) and later used to study viscoelastic contact lines). According to [33] the definitions of the De and Wi are often confused. In De the external time scale τ_{ext} (time scale not related to the polymer relaxation time τ_P) is the time scale of observation, whereas, in Wi the external time scale is τ_{ext} is related to the reciprocal of the deformation rate of the flow. Therefore, according to the above definition, De is 0 for the case of steady state flows whereas the Wi is non-zero. Therefore, in view of this definition, for the case of the droplet the external time scale is $\tau_{ext} = \tau_{em}$ which is the time scale set by the interfacial properties of the droplet.

The deformation, $\mathcal{D}$, and the orientation, θ, of a Newtonian droplet in a viscoelastic medium of a relaxation time of $\tau_P = 2000,\ 4000$ are simulated and compared against the Newtonian case (a Newtonian droplet inside a Newtonian solvent). For the parameters: $R = 30,\ H = 128,\ \chi = 1,\ \eta_M = 1.74,\ \gamma = 0.09$, $\tau_P = 2000$ and 4000 the corresponding values of the $De = 1.42$ and 2.84, respectively. The variation of $\mathcal{D}$ and θ as a function of Ca for the two polymer relaxation times is shown in Figure (4.10a) and Figure (4.10b).

Observations

- From Figure (4.10a), it can be seen that the deformation parameter for the Newtonian droplet in a viscoelastic solvent is smaller in comparison with a Newtonian droplet inside a Newtonian solvent. Thus, it can be concluded that a matrix viscoelasticity inhibits the deformation of a droplet.
- From Figure (4.10b), where the steady state orientation of the droplets are compared, it is observed that droplets inside a viscoelastic matrix with higher polymer relaxation times (oe De) align more easily

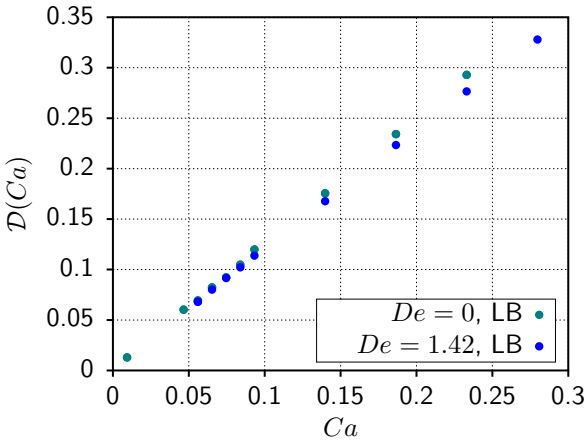

(a) $\mathcal{D}(Ca)$, Viscoelastic Matrix

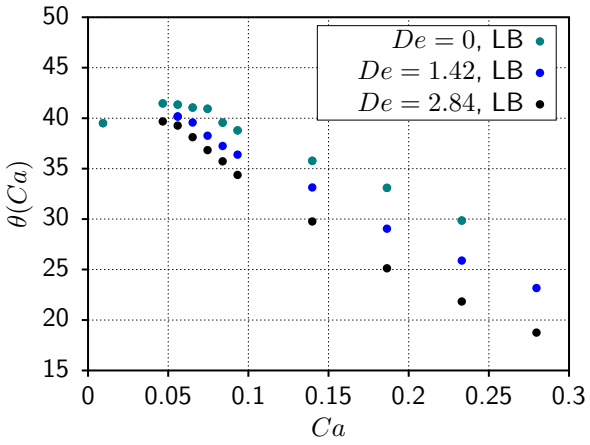

(b) $\theta(Ca)$, Viscoelastic Matrix

Figure 4.10: The steady state deformation parameter $\mathcal{D}$ and steady state orientation θ as a function of the Ca is plotted for a Newtonian droplet inside a viscoelastic matrix. The concentration of the polymer inside the viscoelastic matrix is given by $\frac{\eta_P}{\eta_B+\eta_P} = 0.4$, and the confinement ratio for the droplet is $\frac{2R}{H} = 0.47$. The $De = 1.42,\ 2.84$ correspond to polymer relaxation times of $\tau_P = 2000,\ 4000$, respectively. This plot can be reproduced using the test `R237_DROPLET_IN_VISCO` with the help of the gnuplot scripts `steady_state_deformation.gnu` and `steady_state_orientation.gnu`. The simulations for different Deborah number De and Capillary number Ca is handled by the script `r237.sh` and is registered in gitlab as `ISSUE #242`. The plots can be found in the folder `final_plots`.

with the flow.

- The tensor feedback stress magnitude ((Equation (4.43))) calculated for the current case is shown Figure (4.11) where the magnitude of the tensor feedback is plotted for two different Ca. The tensor feedback stress magnitude is calculated according to the formula:

$$\left\| \underline{\underline{\boldsymbol{\sigma}}}_P \right\| = \sqrt{\underline{\underline{\boldsymbol{\sigma}}}_P : \underline{\underline{\boldsymbol{\sigma}}}_P} = \sqrt{\sigma_{P_{ij}} \sigma_{P_{ij}}}, \tag{4.43}$$

where the repeated index ij corresponds to an Einstein summation. Firstly, we see that the feedback stresses are certainly higher for the case of a higher Ca. In addition, when a constant Ca is maintained, a higher De number gives rise to a higher magnitude of feedback stresses around the Newtonian droplet.

4.1.2.2 Viscoelastic droplet in a Newtonian matrix

In this section a viscoelastic droplet is placed inside a Newtonian matrix. The viscosity ratio between the droplet and the matrix, as before, is maintained at unity, and, the polymer concentration inside the droplet is maintained at $\eta_P = 0.6933$. 2 different polymer relaxation times are used for the droplet: $\tau_P = 2000$, $\tau_P = 4000$, giving rise to the same set of $De = 1.42,\ 2.84$. Firstly, we compare the results of the steady state deformation and the steady state orientation of the droplet. This has been plotted in Figure (4.12a) and Figure (4.12b). In addition, the tensor stress magnitudes inside the droplet are shown in Figure (4.13).

Observations

1. From Figure (4.12a), it can be seen that the deformation parameter for a viscoelastic droplet is smaller in comparison with it's Newtonian counterpart. However, these differences are significant for higher Ca.

2. From Figure (4.12b), it is observed that as the viscoelastic nature of the droplet is increased (an increase in the De) the droplet resists to orient with the flow when compared to smaller De. However, this effect is only shown at higher Ca ($Ca > 0.15$). At lower Ca the differences between $De = 0,\ 1.42,\ 2.84$ are rather small.

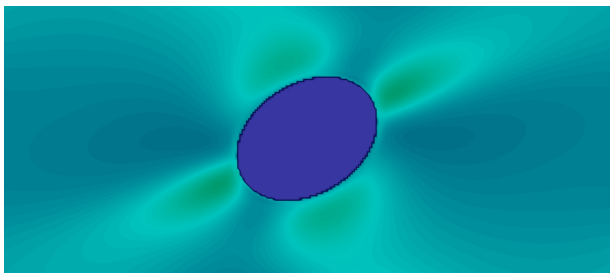

(a) $Ca = 0.145, De = 1.42$

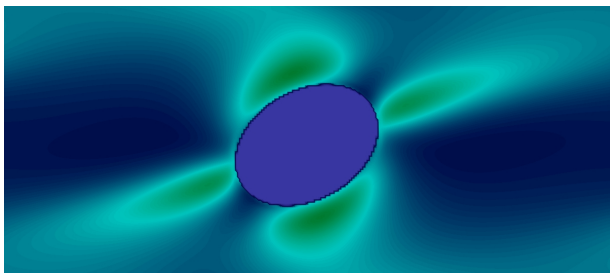

(b) $Ca = 0.145, De = 2.84$

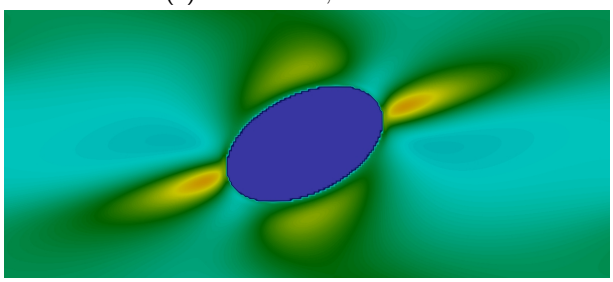

(c) $Ca = 0.24, De = 1.42$

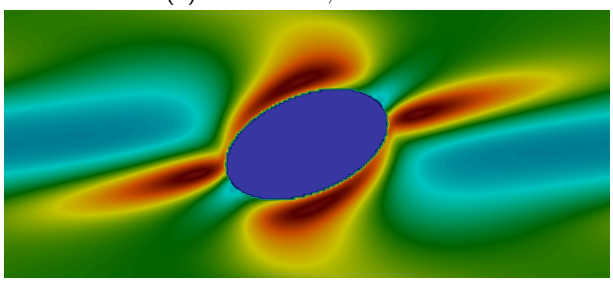

(d) $Ca = 0.24, De = 2.84$

Figure 4.11: Contour plots of the feedback stress magnitude from the 2D LB simulation for a Newtonian droplet inside a viscoelastic matrix for a unity viscosity ratio ($\frac{\eta_A}{\eta_B+\eta_P}$) is shown. The confinement ratio of the droplet is maintained at a constant value of $\frac{2R}{H} = 0.47$ for all the figures shown above. The first row corresponds to a $Ca = 0.145$ and the two polymer relaxation times of $\tau_P = 2000, 4000$ corresponding to $De = 1.42,\ 2.84$, respectively. The color bar indicates the magnitude of the tensor feedback stress (Equation (4.43)) which ranges from a minimum magnitude of 10^{-9} to a maximum stress magnitude of 0.0015.

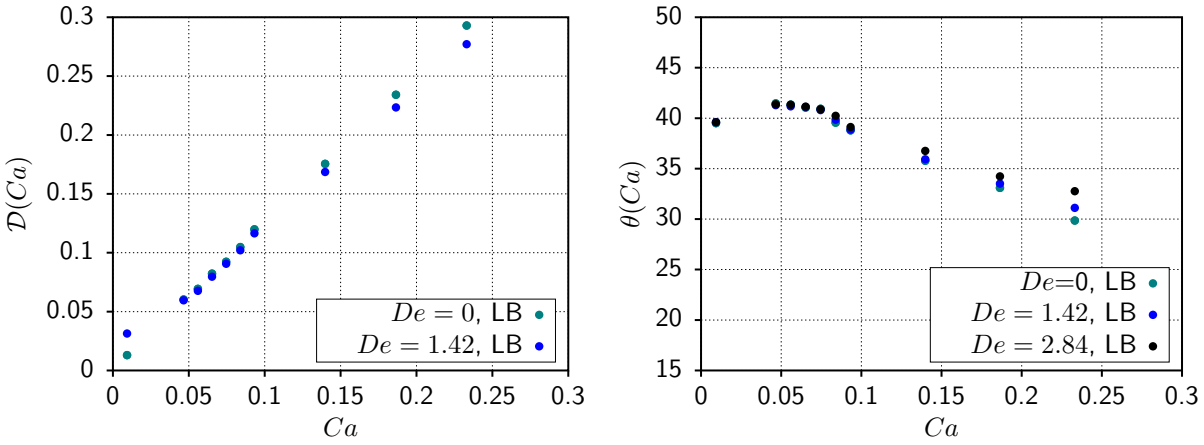

(a) $\mathcal{D}(Ca)$, Viscoelastic droplet

(b) $\theta(Ca)$, Viscoelastic droplet

Figure 4.12: The steady state deformation parameter $\mathcal{D}$ and steady state orientation θ as a function of the Ca is plotted for a viscoelastic droplet inside a Newtonian matrix. The concentration of the polymer inside the droplet is given by $\frac{\eta_P}{\eta_B+\eta_P} = 0.4$, and the confinement ratio for the droplet is $\frac{2R}{H} = 0.47$. The $De = 1.42,\ 2.84$ correspond to polymer relaxation times of $\tau_P = 2000,\ 4000$, respectively. This plot can be reproduced using the test `R237_VISCO_DROPLET` with the help of the gnuplot scripts `steady_state_deformation.gnu` and `steady_state_orientation.gnu`. The simulations for different Deborah number De and Capillary number Ca is handled by the script `r237.sh` and is registered in gitlab as `ISSUE #243`. The plots can be found in the folder `final_plots`.

3. It is also instructive to look at the polymeric feedback stress magnitudes inside the droplet, for both increasing Ca and De. This is shown in Figure (4.13). As expected, the tensor feedback stresses are higher for higher Ca and De, due to stronger velocity gradients of the flow inside the droplet. The larger deviations from the Newtonian case at higher Ca for $De = 1.42,\ 2.84$ can be attributed to the increase in the magnitudes of the tensor feedback stresses arising inside the droplet.

4.1.3 Conclusion

It is beneficial to conclude this section by summarizing the results obtained from the all validation cases which were performed, and most importantly: to adopt the knowledge obtained from the validation cases in simulating the non-Newtonian contact line problem. The summary of the tests are as follows:

1. **Couette flow**
   - The excellent matching for the *polymeric shear stress* $\mathcal{S}$ and the *first normal stress difference* $\mathcal{N}$ in comparison to theoretical predictions for a steady shear flow showed that the LB model could be effectively combined with the FD formalism for evolving the dynamics of polymers (governed by the FENE-P potential) in a simple shear flow.
   - In addition, it also showed that the model could simulate shear thinning effects at high Λ, and, the shear thinning can be delayed by increasing the flexibility of the polymer, controlled by the parameter L^2. This knowledge will be useful in isolating the elastic effects from the shear thinning effects when simulating the non-Newtonian contact line problem.
2. **Steady elongational flow**
   - It is known that elongational flow generates flow fields which are purely stretching with zero vorticity, in contrast with the flow field generated in a shear flow. Through this test the *elongational viscosity* of a dilute FENE-P solution was obtained from the LB simulations and compared to theoretical predictions. The matching between theory and simulation suggests that the model is robust and efficient in predicting the dynamics of FENE-P polymers under different flow condition.

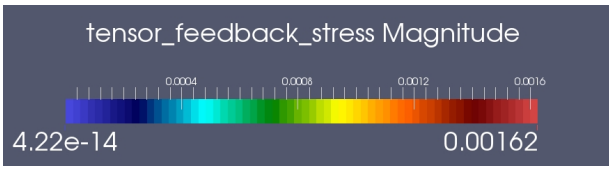

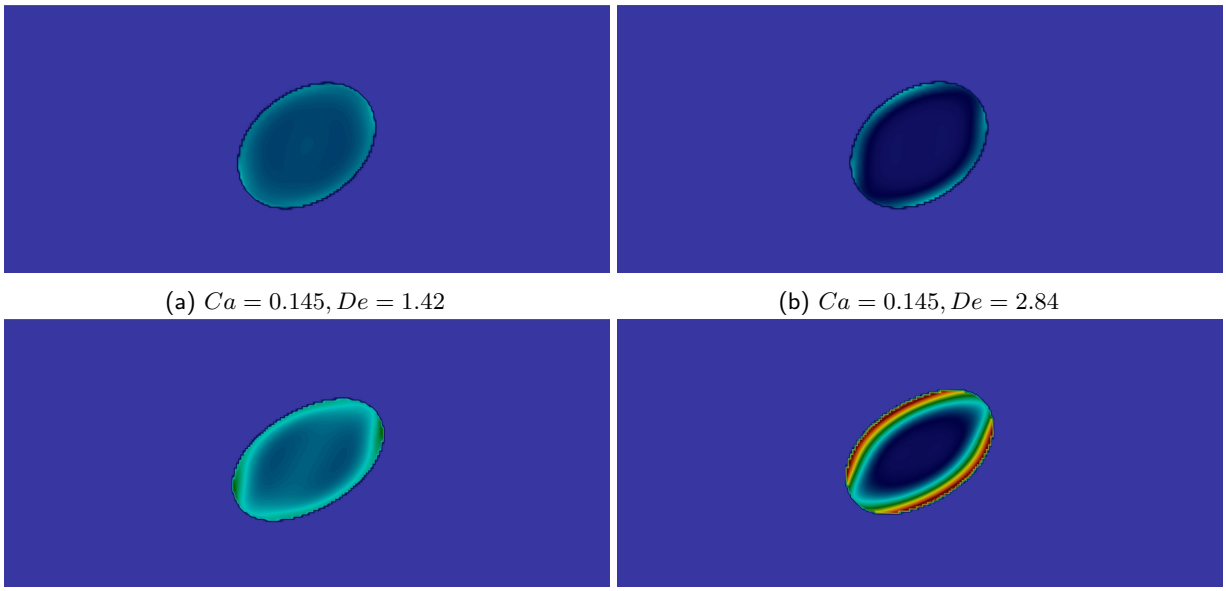

(a) $Ca = 0.145, De = 1.42$

(b) $Ca = 0.145, De = 2.84$

(c) $Ca = 0.24, De = 1.42$

(d) $Ca = 0.24, De = 2.84$

Figure 4.13: Contour plots of the feedback stress magnitude from the 2D LB simulation for a viscoelastic droplet inside a Newtonian matrix for a unity viscosity ratio ($\frac{\eta_A}{\eta_B+\eta_P}$) is shown. The confinement ratio of the droplet is maintained at a constant value of $\frac{2R}{H} = 0.47$ for all the figures shown above. The first row corresponds to a $Ca = 0.145$ and the two polymer relaxation times of $\tau_P = 2000, 4000$ corresponding to $De = 1.42,\ 2.84$, respectively. The color bar indicates the magnitude of the tensor feedback stress (Equation (4.43)) which ranges from a minimum magnitude of 10^{-9} to a maximum stress magnitude of 0.00162.

3. **Oscillatory shear flow**

   - Unlike the previous two cases this test was performed to understand the robustness of the LB under time dependent flows. For this, the storage and loss modulus G' and G'', which is characteristic of a viscoelastic material, were calculated using the polymeric shear stress signal, once it had stabilized. An excellent matching of G' and G'', as a function of the non-dimensionalized oscillation frequency ($\omega\tau_P$), with the theoretical prediction implied that the LB model could handle time dependent flows.
   - However, the LB model seemed to work best when the criteria $\omega\tau_{\nu_s} \ll 1$, which necessitates that the time required for the momentum diffusion from the moving walls should be lesser in comparison with the time period of velocity signal.

4. **Droplet deformation**:

   - Both, Newtonian droplet in a viscoelastic matrix and Viscoelastic droplet in a Newtonian matrix, were simulated using multicomponent *Shan-Chen* LB. The effects of viscoelasticity on *steady state deformation* and *steady state orientation*, as a function of the Ca, were captured very well by the LB simulations (when compared with the theoretical predictions).
   - In addition, as stated at the beginning of the chapter, the values of relevant parameters: (a) mobility μ, (b) smoothing parameter Δ were obtained for simulating multicomponent flows involving viscoelastic fluids.

Now, since the role of all the relevant FENE-P parameters: τ_P, L^2, ϕ and the fluid LB parameters: τ, $\mathcal{G}$ and μ under various flow conditions have been explored and understood, non-Newtonian contact lines can now be studied using this knowledge. Hence, first, a simple validation is performed to understand the case of a Newtonian contact line using the multicomponent LB, following which the non-Newtonian contact lines will be studied using the features studied in this section.

4.2 Contact lines

In this section the non-Newtonian contact line problem is addressed. Firstly, we describe the Couette flow model for binary fluid systems in which the contact line problem will be investigated. Following the description of the Couette model, it's LB implementation will be discussed and the relevant parameter values will be presented. The results for the steady state macroscopic contact angle θ_M as a function of the Ca will be shown and validated against the theoretical θ_M vs Ca, using a single free parameter: separation of scales λ_s.

Once the benchmarking for the case of Newtonian contact lines has been established, the results of the non-Newtonian contact lines will be discussed in the final section.

4.2.1 Couette flow geometry setup

The problem of dynamic contact lines has been extensively studied in the past few years. Different authors have adopted different geometries for studying the dynamic contact lines. Jacqmin [19] studied the steady state and the wetting failure for dynamic contact lines using lubrication theory and phase field simulations in a Couette flow geometry. Bryant *et al.* [59,60] studied the dynamic contact lines using phase field LB simulations for both liquid-gas and binary liquid systems, in a Couette flow setup. Further, Sbragaglia *et al.* [28] extended the work done by Jacqmin [19] in terms of theory to study the wetting failure in multicomponent systems with variable viscosity ratio, χ, separation of length scales, λ_s, and microscopic wetting angle, θ_{m}. The extended theory was validated with results from the multicomponent LB simulations for the macroscopic θ_{M} as a function of Ca, and, the accuracy in the predictions of diffuse interface measurements towards sharp-interface theoretical predictions was also addressed.

Hence, considering the amount of literature available on the study of dynamic contact lines for multicomponent systems in a Couette flow, our simulation can be readily compared against existing theoretical predictions. In addition, the Couette flow model is simple with regards to the implementation of relevant boundary conditions and also with regards to the run time of a single simulation.

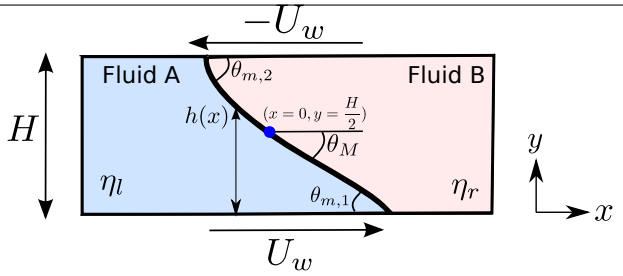

Figure 4.14: The figure represents a schematic of the flow geometry for the problem being studied. The geometry is infinite in the x direction. 2D rectangular channel with two fluids (**Fluid A** and **Fluid B**) are sandwiched between the top and bottom walls. **Fluid A** and **Fluid B** have dynamic viscosities of η_l and η_r, respectively. The fluids are sheared by the top and bottom walls with a velocity of $-U_w$ and U_w, respectively. The angle subtended by the interface at the center of the channel is defined as θ_M, whereas, the microscopic contact angle of **Fluid A** at the top and bottom walls are defined as $\theta_{m,1}$ and $\theta_{m,2}$, respectively. In addition, the interface profile is captured by the function $h(x)$, where x is set to zero at the center of the channel.

Geometry Description :
The Couette flow geometry used in the LB simulations is described and explained in Figure (4.14).

The Couette flow cell consists of two fluids, **Fluid A** and **Fluid B**. The Couette cell is bounded by moving walls in the y direction: $y = 0$ $(-U_w)$ and $y = H$ $(+U_w)$, and, periodic in the direction of the shear. The *Shan-Chen* multicomponent model is employed for obtaining two immiscible fluids. **Fluid A** is initialized with components: $\rho_1 = 2.0$ (major) and $\rho_2 = 0.1$ (minor), and, **Fluid B**: $\rho_1 = 0.1$ (minor) and $\rho_2 = 2.0$ (major). The surface tension between the fluids in the multicomponent model is controlled by the interaction strength $\mathcal{G} = 1.3$ and the total bulk density $\rho_1 + \rho_2 = 2.1$ [61]. The viscosity of Fluid A and B are set to a value equal to $\eta_l = \eta_r$=1.75 and, as a consequence, a viscosity ratio of 1.0 is maintained between them. The microscopic contact angle at the top and bottom wall for the two fluids are controlled by the wettability parameters $\mathcal{G}_{A,\text{wall}}$ and $\mathcal{G}_{B,\text{wall}}$ [47]. The following values are chosen:

$$\begin{cases} \mathcal{G}_{A,\text{wall,bottom}} = -0.22, & \mathcal{G}_{A,\text{wall,top}} = +0.22, \\ \mathcal{G}_{B,\text{wall,bottom}} = +0.22, & \mathcal{G}_{B,\text{wall,top}} = -0.22, \end{cases} \tag{4.44}$$

where the integer 1 or 2 in the subscript of $\mathcal{G}_{A/B,\text{wall}}$ corresponds to fluid 1 or 2 respectively, the term bottom or top corresponds to the top and bottom wall. Hence, a negative value of the $\mathcal{G}$ corresponds to a hydrophilic behavior of the fluid towards the wall, and, a positive value of $\mathcal{G}$ corresponds to a hydrophobic behavior. Therefore, Equation (4.44) suggests that the fluids wet the top and bottom wall with opposite wettability. This implies that when $U_w = 0$ the interface between the two fluids is a *straight line* between the top and bottom wall whose slope is given by $\tan(\pi - \theta_\text{m})$, where θ_m is the microscopic wettability.

Now that the Couette flow geometry for the problem has been described in detail, the bench marking for the case of Newtonian contact lines for a multicomponent system will be performed.

4.2.2 Newtonian contact lines

In this section the bench marking for the case of dynamic contact lines in a Newtonian fluid will be done. Prior to the benchmarking it is useful to identify the relevant *non-dimensional quantities* and the *observables* for the bench marking.

The requisite equations accompanied by simplifications effected by lubrication theory to describe the interface in multicomponent systems has been comprehensively dealt by Sbragaglia *et al.* [28]. Here, the key parameters from the article will be highlighted and used for bench marking our system:

1. The capillary number for the system is defined as:

$$Ca = \frac{\eta_l U_w}{\gamma}, \tag{4.45}$$

where η_l is the dynamic viscosity of Fluid A, U_w is the velocity of the wall and γ is the surface tension between the two fluids.

2. The viscosity ratio χ is defined as:

$$\chi = \frac{\eta_r}{\eta_l}, \tag{4.46}$$

where η_l, η_r represent the dynamic viscosities of Fluid A and Fluid B, respectively, see Figure (4.14).

3. The separation of length scales λ_s is defined as:

$$\lambda_s = \frac{l_s}{H}, \tag{4.47}$$

where l_s is the microscopic slip length and H is the channel height. This quantity represents the separation between length scales at which the hydrodynamic theory successfully describes flow characteristics near a contact line. However, it is important to note that in the LB method the no-slip boundary condition is imposed and a *diffuse interface* is used to regularize the contact line singularity [19, 28, 60, 62].

4. Finally, the microscopic contact angle θ_{m} is a parameter which allows for the control of the wetting angle at the wall, see fig Figure (4.14). The smaller the value of θ_{m}, higher the tendency for the fluid to wet the wall.

The following features of the Newtonian contact lines are studied using LB simulations and they are compared against relevant theoretical predictions as obtained by Sbragaglia *et al.* [28]:

1. θ_{M} vs Ca: As shown in Figure (4.14), the angle at the center of the channel is determined as a function of Ca. This is compared against theoretical predictions to determine the scale separation parameter λ_s.

2. **Interface profile**: For a particular Ca, using the value of λ_s, the interface from the LBE simulations is compared against the theoretical predictions.

3. **Velocity profile**: For the same Ca the velocity profile at a particular position $\frac{x}{L}$, where L is the span of the contact line, and compared against the theoretical results, using the slip length parameter λ_s. In addition the velocity field near the contact line is visualized using the velocity vectors.

The above measurements are made in the simulations once they have achieved a steady state. We check for the steady state by measuring the velocity of the contact line at the top and bottom walls, see Figure (4.15).

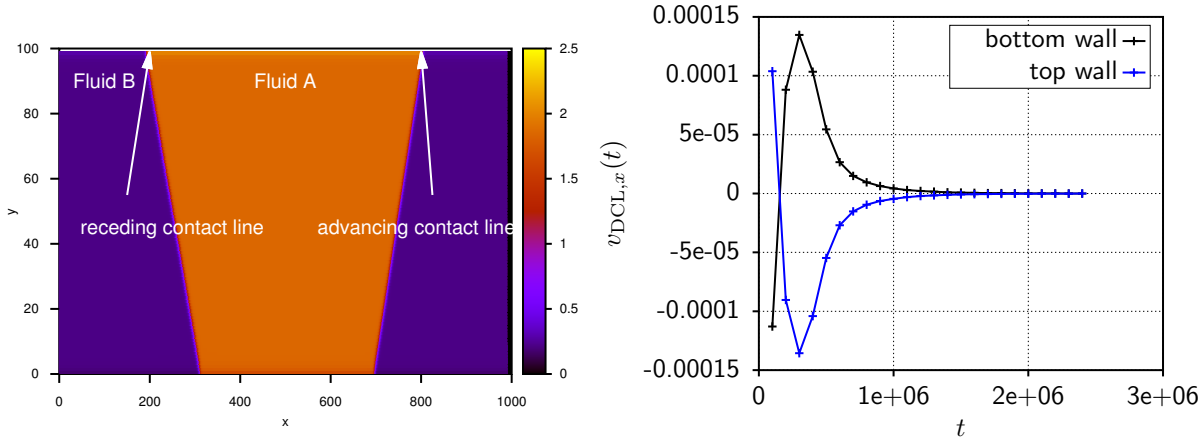

(a) $\chi = 1.0$, θ_{m} =40.48, $Ca = 5.362 \times 10^{-4}$

(b) $\chi = 1.0$, θ_{m} =40.48, $Ca = 5.362 \times 10^{-4}$

Figure 4.15: In (a) the LB setup for the Couette flow geometry is shown. The contour of Fluid A is shown in the figure. Equal volumes of Fluid A and Fluid B are initialized inside the Couette flow geometry. In (b) the magnitude of the contact line velocity at different simulation times are plotted. The blue line corresponds to the contact line at the top wall and the black line corresponds to the contact line at the bottom wall.

4.2.2.1 θ_{M} vs Ca

As shown in Figure (4.14), the angle at the center of the channel θ_{M} is measured as a function of Ca. To extract the angle θ_{M} a contour plot of the density field on the interface at the level $\rho_{av} = \frac{\rho_A+\rho_B}{2}$, with ρ_A and ρ_B being the densities of Fluid A and Fluid B (see Figure (4.14)), respectively. The result of θ_{M} vs Ca is shown in Figure (4.16) for a microscopic wetting angle of θ_{m} =40.48, and, a viscosity ratio χ of 1.0 between Fluid A and Fluid B.

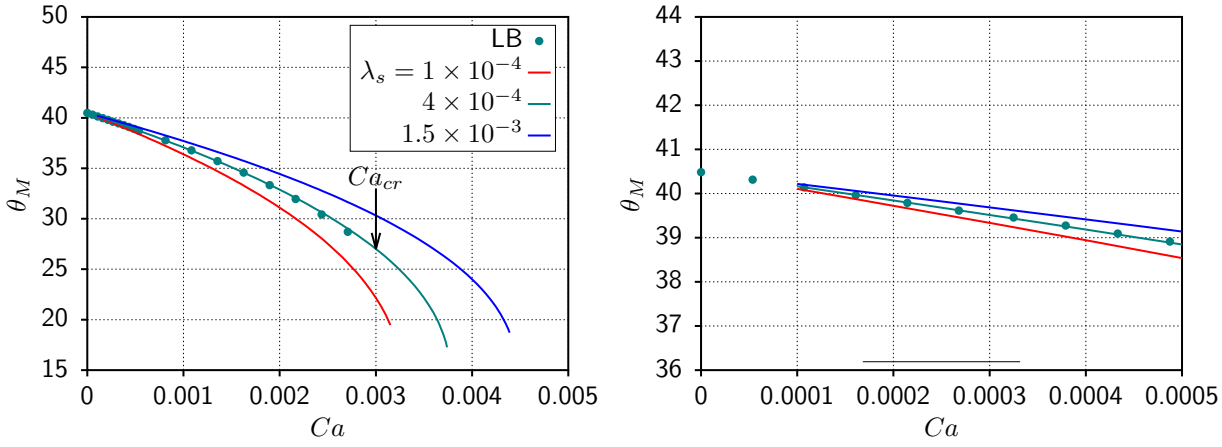

(a) θ_{M} vs Ca

(b) θ_{M} vs Ca, inset

Figure 4.16: In (a) θ_{M} vs Ca obtained from LB simulations is compared against the theoretically derived curves, for different values of the scale separation parameter λ_s. The viscosity ratio of $\chi = 1.0$ is maintained between the two fluids in Couette flow setup and the microscopic contact angle θ_{m} =40.48 is used to derive the theoretical curves. The value of $\rho_A = 2.00$, $\rho_B = 0.06$ and the interaction parameter value $\mathcal{G} = 1.3$ is used, which gives a surface tension $\gamma = 0.0634$ and a dynamic viscosity value of $\eta_l = \eta_r = 0.3433$. The BGK relaxation time for both the components is 1.0 and the multi relaxation time is utilized. In (b) a magnified view of the plot in (a) for the range of Ca between 0 and 0.001 is shown.

The condition of opposite wall wettabilities is used (see Section (2.2)). Using these parameters the non-linear boundary value problem, as stated in chapter 2, is solved for various scale separation parameters λ_s. LB simulation results are compared to theoretical curves to identify the scale separation parameter λ_s. We observe the following:

- In Figure (4.16), for $\lambda_s = 4 \times 10^{-4}$ the LB simulation matches the theoretical prediction. To understand the sensitivity of the simulated curve to the value of λ_s, a comparison between a lower $\lambda_s = 1 \times 10^{-4}$ and a higher $\lambda_s = 1.5 \times 10^{-3}$ is also shown.
- The critical capillary number observed in the LB simulations (indicated by an arrow) in Figure (4.16) is smaller than the critical Ca predicted by the theory. This could be due to the finite size effects introduced by the finite size of the channel.

Using λ_s obtained above, we also validate the shape of the interface from simulations against theory.

4.2.2.2 Interface comparison

In Figure (4.17) we study the behavior of interfaces for the following parameters: $\chi = 1.0$, θ_{m} =40.48, $\lambda_s = 4 \times 10^{-4}$. Before we compare the interfaces obtained from LB with theory, we first compare the theoretical curves themselves in Figure (4.17a). Following this, the interface is obtained through LB for the highest Ca before the system reaches critical wetting, $Ca = 2.47 \times 10^{-3}$. We compare this results against theory as well.

We observe the following:

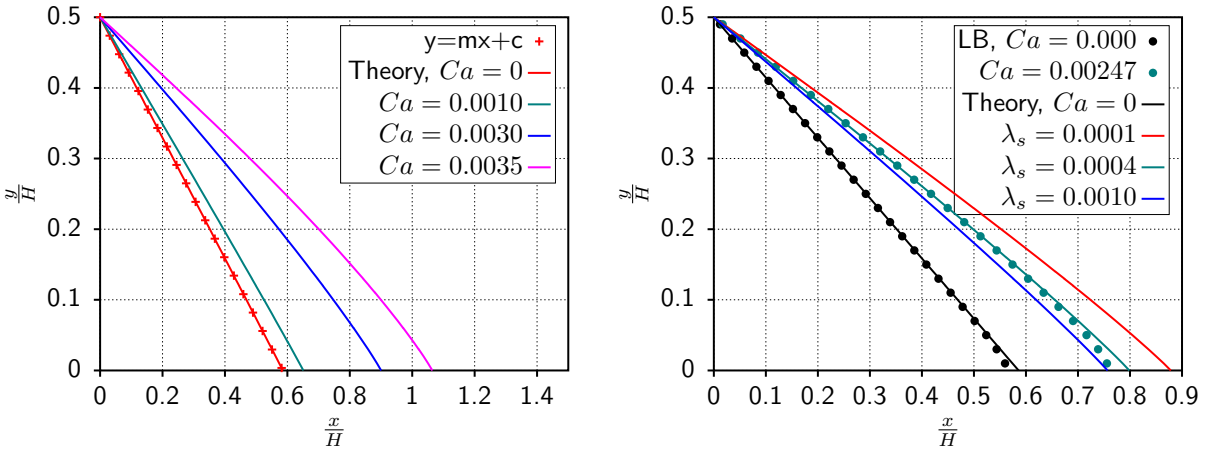

(a) $\chi = 1.0$, θ_{m} =40.48, $\lambda_s = 4 \times 10^{-4}$, Theory

(b) $\chi = 1.0$, θ_{m} =40.48, $\lambda_s = 4 \times 10^{-4}$, LB vs Theory

Figure 4.17: In (a) the shape of the interface, as obtained from theory, characterized by the normalized y co-ordinate $\frac{y}{H}$ is plotted against the normalized x co-ordinate $\frac{x}{H}$, where H is the distance between the walls (see Figure (4.14)). The shape of the interface is plotted for different values of Ca. The parameters used for plotting the interface are:$\chi = 1.0$, θ_{m} =40.48, $\lambda_s = 4 \times 10^{-4}$. The case of $Ca = 0$ is compared with the equation of a straight line whose slope is given by π - θ_{m}. In (b) the interface shape as obtained through LBE is compared against the theoretical predictions. The comparison is done for $Ca = 0\& \ 2.47 \times 10^{-3}$, for the following set of parameter values $\rho_A = 2.00$, $\rho_B = 0.06$, $\mathcal{G} = 1.3, \mathcal{G}_{A,ads} = -0.4$. The interface for $Ca = 2.47 \times 10^{-3}$ is compared for three different values λ_s.

- In Figure (4.17a) the shape of interface at $Ca = 0$ is benchmarked against the equation to a straight line y=mx+c with slope $m = \pi - \theta_m$ and intercept $c = 0.5$. We see that they match perfectly and therefore can be used for comparison at higher Ca.
- From Figure (4.17a) we observe that as the Ca approaches towards the Ca_{cr} the interface curvature increases and the position of the receding contact line is pushed backward.
- In Figure (4.17b) the interface shapes as obtained from LBE is compared against the theoretical interface shapes. Firstly, $Ca = 0$ is compared with the theoretical prediction. It can be seen that the interface matches well with theory for $\frac{y}{H} > 0.02$. For $\frac{y}{H} < 0.02$ the interface starts to bend and hence deviates from theory. A similar bending of the interface near the wall is seen for $Ca = 2.47 \times 10^{-3}$. For both: $Ca = 0$ & .00247 the value of $\lambda_s = 4 \times 10^{-4}$.
- To probe the sensitivity of the simulated interface w.r.t λ_s a comparison between a lower $\lambda_s = 1 \times 10^{-4}$ and a higher $\lambda_s = 1.5 \times 10^{-3}$ is also shown. The position of the contact line for $\lambda_s < 4 \times 10^{-4}$ lags behind in comparison with the position of the contact line for $\lambda_s > 4 \times 10^{-4}$.

In the next section the velocity field near the contact is visualized and we try to quantitatively match the velocity profile with that obtained from theory.

4.2.2.3 Velocity fields

We look at the velocity fields from a qualitative and a quantitative perspective. For this $\chi = 1.0$, $\theta_m = 40.48$, $\lambda_s = 4 \times 10^{-4}$, $Ca = 5.362 \times 10^{-4}$ is chosen. At the cross section $\frac{x}{L}$=0.5 (L is the span of the receding contact line) the x-component of the velocity field $v_x(y)$ is plotted in Figure (4.18). It is interesting to observe the velocity vector field $\boldsymbol{u}(x, y)$ near the receding contact line and qualitatively compare it to Huh-Scriven velocity fields which was introduced in Chapter 2, see Figure (4.18b).

The following are the observations:

- From Figure (4.18a) it is seen that the x-velocity component is quadratic in the y-direction. Hence, it resembles a Poiseuille-like velocity distribution. In addition, the slip at the wall is negligible and very

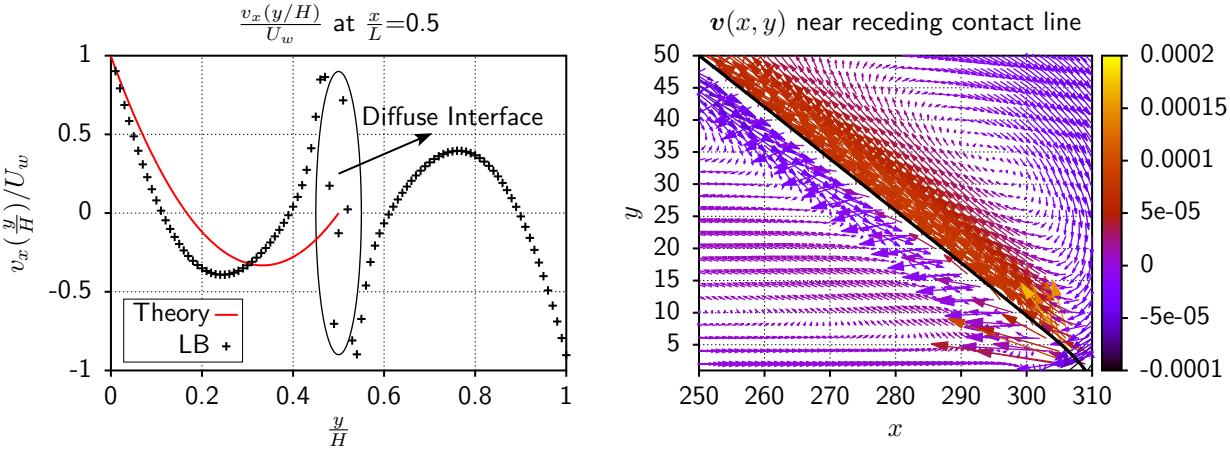

(a) $\chi = 1.0, \theta_m = 40.48, Ca = 5.362 \times 10^{-4}$ (b) $\chi = 1.0, \theta_m = 40.48, Ca = 5.362 \times 10^{-4}$

Figure 4.18: In (a) the x-component of the velocity profile v_x is plotted as a function of the normalized y co-ordinate $\frac{y}{H}$ at a location $\frac{x}{L} = 0.5$, where L is the span of the interface. Spurious oscillations in v_x are observed at the diffuse interface and the position of the interface is indicated in the figure. In (b) the velocity vector field $\boldsymbol{v}(x, y)$ is plotted for a region close to the receding contact line. The magnitude of the velocities is represented by the changing color of the arrows at different spatial locations and the color code provides the magnitude. The black line represents the interface.

close to zero [1].

- However, it can be observed that the magnitude of the velocity gradient for the LB simulation, as $\frac{y}{H} \to 0$, is higher in comparison to theory. In addition, the magnitude of the velocity at the diffuse interface (5 grid points) is comparable to the wall velocity U_w.
- From Figure (4.18b) we see that the velocity vectors qualitatively behave in a manner similar to the Huh-Scriven velocity fields, i.e. when they approach the diffuse interface they take a turn and the mass diffusion across the interface is low.
- In addition, the spurious velocity vectors at the contact line are high in magnitude, as seen in Figure (4.18b). However, the velocity of the contact line itself (w.r.t to a stationary frame of reference) is very close to zero, as suggested by Figure (4.15).

With this we conclude the benchmarking for Newtonian contact lines. For all the three features – θ_M vs Ca, interface profile and velocity profile, we have found very good agreement between simulation and theory. In the next section non-Newtonian contact lines will be investigated.

4.2.3 Non-Newtonian contact lines

We now simulate the non-Newtonian contact lines. As was discussed in Chapter 2 (Section (2.4)), the addition of polymers to the Newtonian fluid gives rise to an additional time scale, the polymer relaxation time τ_P. τ_P competes with the time scale of the flow and the non-dimensional Weissenberg number Wi is defined as:

$$Wi = \tau_P \dot{\gamma}, \tag{4.48}$$

where τ_P is the polymer relaxation time, and $\dot{\gamma}$ is the shear rate. Based on our knowledge of contact lines from Chapter 2 we can define two different Wi depending on the position from the contact line. The first definition can be called the global Wi which is calculated using the global shear rate $\dot{\gamma}_{\text{global}} = \frac{2U_w}{H}$. However, close to the contact line the local shear rate is higher in magnitude when compared to the global shear rate. Roughly:

$$\dot{\gamma}_{\text{local}} \approx H\dot{\gamma}_{\text{global}}, \tag{4.49}$$

[1] When velocity data is extrapolated at the position of the wall, the magnitude of the velocity is negligible.

where H is the height of the channel in Couette flow geometry and U_w is the LB wall velocity. The above argument can be rationalized based on the fact that close to the contact line the velocity vectors have to negotiate sharp turns within a very small height $h(x)$, where x is the distance from the contact line. In a LB simulation the smallest distance is the distance between any two lattice points and, close to the contact line the change in the velocity component parallel to the wall is close to $2U_w$ (Figure (4.19)). Therefore, the local shear rate $\dot{\gamma}_{\text{local}} \approx H\dot{\gamma}_{\text{global}}$. As a consequence:

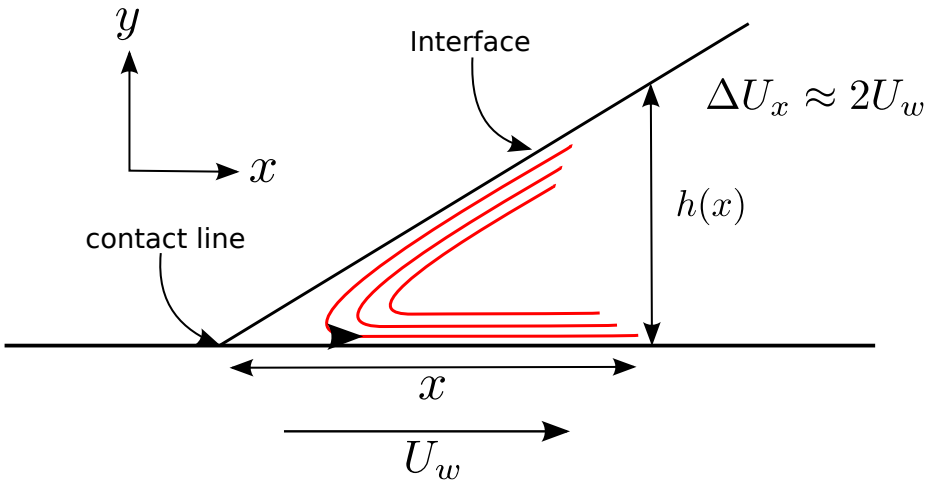

Figure 4.19: A schematic of the velocity field close to the contact line is shown. The distance from the contact line is given by the distance x. The height to the interface is given by $h(x)$. The wall velocity is given by U_w and the direction is towards the positive x-axis. Close to the contact line the change in the x-component of the velocity of the fluid is approximately twice the wall velocity. In a LB simulation the minimum grid length is 1 cell. Therefore, the local shear rate $\dot{\gamma}_{\text{local}}$ is approximately H times the global shear rate $\dot{\gamma}_{\text{global}}$.

$$Wi_{\text{local}} \approx HWi_{\text{global}}. \tag{4.50}$$

In the following sections we investigate the contact line problem for (a) symmetric wetting, and (b) asymmetric wetting.

4.2.3.1 Symmetric wetting

Firstly, we investigate opposite wettability for the case where both Fluid A and Fluid B have equal wetting angles at the top and bottom walls (Figure (4.20)).

We compare the shape of interface at $Ca = 1.75 \times 10^{-3}$ for both the receding (RCL) and the advancing contact lines (ACL) in Figure (4.21). We observe the following:

- At the receding contact line the displacement of the contact line increases as τ_p decreases. Even though we observe a trend for the displacement of the contact line for varying τ_P, it is weak.
- At the advancing contact line the differences in the displacement of the contact line between different polymer relaxation times are negligible. However, the displacement of the contact line for $\tau_P = 0$ is the largest.

In addition to the shape of the interface, interestingly, we observe that the polymer relaxation time τ_P has no influence on the critical wetting behavior. In other words the Ca_{cr} did not change for different polymer relaxation times τ_P. The reason for this can be argued along the following lines.

Critical wetting occurs at a critical capillary number Ca_{cr} due to instabilities at the moving contact line. For the case of symmetric wetting in Newtonian contact lines, the instability at Ca_{cr} will occur at both the top and bottom walls, due to the symmetries in dynamical viscosities η and microscopic wetting angles of Fluid A and Fluid B (Figure (4.22)). However, when either Fluid A or Fluid B is replaced with a viscoelastic fluid, the symmetry is broken by the presence of polymers in one of the fluids which introduces additional normal and polymeric shear stresses. Therefore, contact line instability at the top and bottom wall, might not

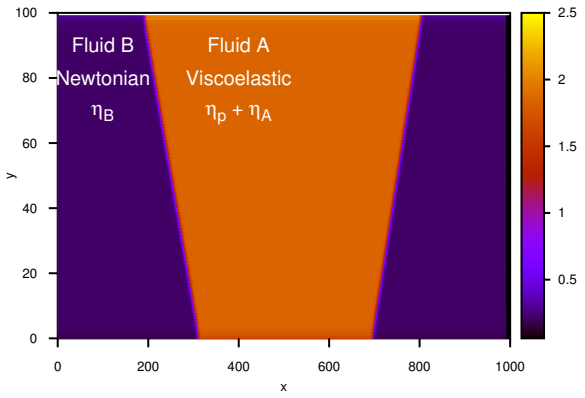

Figure 4.20: Symmetric wetting ($\theta_{m,1} = \theta_{m,2}$) is depicted. To simulate contact lines for non-Newtonian fluids, Fluid A is made viscoelastic and Fluid B is Newtonian. The viscoelasticity of Fluid A is controlled through the polymer relaxation time τ_P for a fixed L^2, and polymeric viscosity η_P. The dynamic viscosity of Fluid A is the sum of viscosity due to component A (η_A) and due to the polymer (η_P). For Fluid B the dynamic viscosity is given by the viscosity of component B (η_B). The viscosity ratio χ between the 2 fluids is 1.

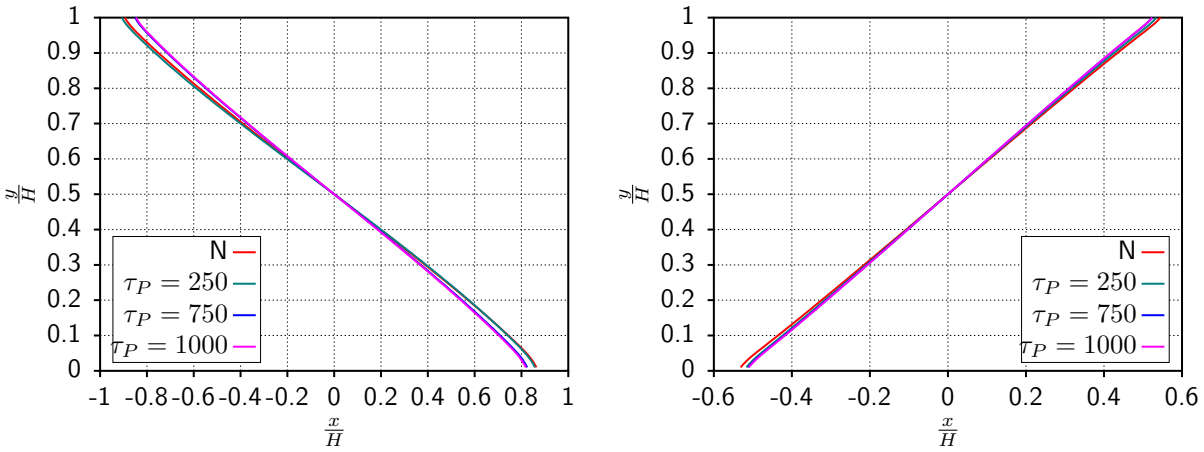

(a) RCL, $Ca = 1.75 \times 10^{-3}$ (b) ACL, $Ca = 1.75 \times 10^{-3}$

Figure 4.21: The interfaces corresponding to the (a) receding and (b) advancing contact lines are plotted for different τ_P. In the x-axis the normalized x-coordinate (normalized by the height of the channel H). Similarly, the y position of the interface is normalized by the height H between the walls. The x position corresponding to $y = \frac{H}{2}$ is set to 0. The LB parameters chosen for the simulation are: (a) $\rho_A = 2.00$, $\rho_B = 0.1$ and $\mathcal{G} = 1.3$ gives a surface tension $\gamma = 0.1$. The BGK relaxation times of the two fluids is given by $\tau = 3$ which gives a value of dynamic viscosity $\eta_r = \eta_l = 1.75$. The viscoelasticity of the central fluid is changed by controlling the polymer relaxation time τ_P. For the above simulations $L^2 = 10^4, \tau_P = 0.693$, and, $\tau_P = 0$ case is where both Fluid A and Fluid B are Newtonian. The above plots can be reproduced using the test `R237_COUETTE_WETTING_MC` with the help of the gnuplot script `interface_compare_plot.gnu`. The simulations for different τ_p is handled by the script `r237.sh` and is registered in gitlab as `ISSUE #133`.

occur at the same velocities at the top and bottom walls. In other words, the critical wetting at the receding contact line for the viscoelastic fluid might be delayed in comparison with the Newtonian fluid. The instability of the interface itself is governed by the smaller of the two wall velocities. Hence, it becomes impossible to probe the effects of viscoelasticity on the critical wetting behavior.

Therefore, we adopt a wetting condition which prevents the Newtonian fluid from causing the wetting failure, and allows us to perceive *only* the effects of viscoelasticity on critical wetting at the receding contact line. We impose a microscopic wetting angle of 90^o at the bottom wall and maintain the same angle, as the symmetric wetting case, at the top wall. This ensures that velocities required to cause critical wetting at the bottom wall contact line is much larger in magnitude than the velocity required to cause critical wetting at the top wall. This allows us to exclude the contribution of the Newtonian fluid towards critical wetting and exclusively probe viscoelastic effects on the moving contact line. The next section deals with the asymmetric case. In the parameter range investigated the symmetric wetting case does not allow us to investigate the

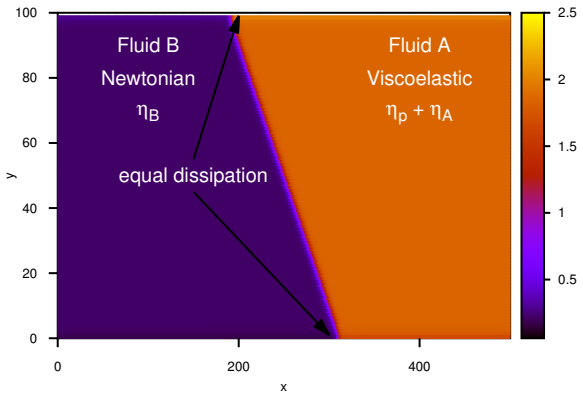

Figure 4.22: In the symmetric wetting case instability at the contact line can occur due to Fluid A (top wall) or Fluid B (bottom wall) due to the symmetric conditions in viscosities and microscopic wetting angles.

influence of viscoelasticity on the critical wetting behavior. Therefore, we adopt an asymmetric wetting case where the microscopic contact angle at the top and bottom walls are changed.

For the case of symmetric wetting we observed that the maximum wall velocity that could be achieved (before critical wetting) was $U_w = 2 \times 10^{-4}$. Therefore, the range of Wi that was simulated was:

τ_P	Wi_{global}	Wi_{local}
250	0.001	0.1
500	0.002	0.2
750	0.003	0.3
1000	0.004	0.4

4.2.3.2 Asymmetric wetting

Our aim now is to probe solely the effects of viscoelasticity on the critical wetting behavior. Therefore, the following set of wetting angles at the top and bottom wall are used:

$$\theta_{\text{m,top}} \approx 43^o, \quad \theta_{\text{m,bottom}} \approx 90^o.$$

These wetting angles ensure that the wetting failure will occur first at the top wall. More importantly, the wetting failure occurs solely due to the viscoelastic component. With this motivation we move ahead to investigate the contact line at the interface of a viscoelastic component and a Newtonian component. Before that, we outline the LB parameters used for this simulation using Figure (4.23). A point to note in Figure (4.23) is that the relaxation time of the two components **A** and **B** inside Fluid A and Fluid B are changed in a way that ensures a viscosity ratio $\chi = 1.0 = \frac{\eta_P + \eta_A}{\eta_B}$.

Before presenting the results for the asymmetric wetting case, we provide the range of Wi investigated. The results in the following section are discussed for $Ca = 5.25 \times 10^{-3}$ for which the velocity is the wall velocity $U_w = 3 \times 10^{-4}$ and $H = 120$. Therefore, the range of global and local Wi are summarized in the table:

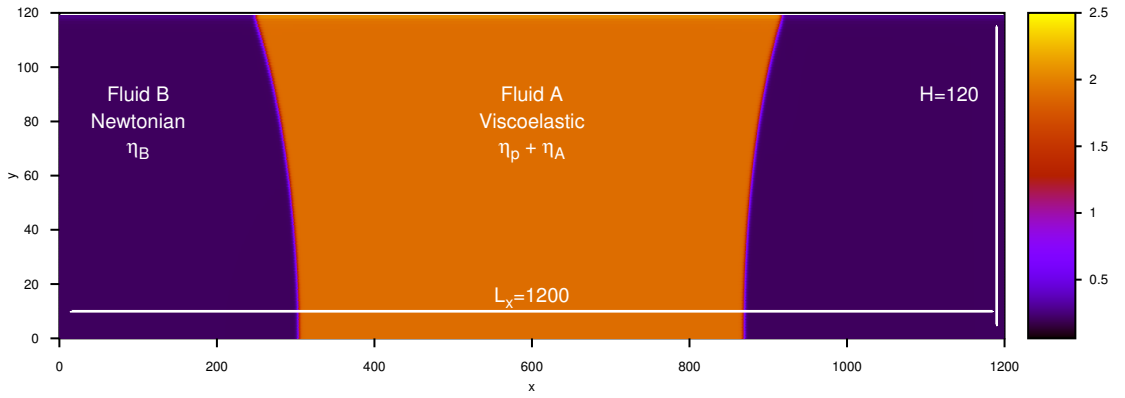

Figure 4.23: The setup for studying the contact line in the asymmetric wetting configuration in presented in the above figure. The density contour plot of component A is shown in the figure. The densities of component A and B in the channel are initialized to $\rho_A = 2.00, \rho_B = 0.1$ with the interaction strength $\mathcal{G} = 1.3$ between the two components. The BGK relaxation time of the two components is given by $\tau_A = \tau_B = 3.0$ inside Fluid B. However, the relaxation time of the two components inside Fluid A is equal to $\tau_A = \tau_B = 1.0$. The distance between the walls is given by $H = 120$, and, $L_x = 1200$. With regards to the FENE-P parameters, the τ_P of the viscoelastic component is varied between 1000 to 5000, the maximum extensible length is $L^2 = 10^4$ and the polymeric viscosity η_P=1.4. The adopt the asymmetric wettabilities at the top and bottom wall $\mathcal{G}_{\mathrm{A,wall,top}} = -0.22$ at the top wall and $\mathcal{G}_{\mathrm{A,wall,bottom}} = 0$. Similarly, for component B, the $\mathcal{G}_{\mathrm{B,wall,top}} = +0.22$ and $\mathcal{G}_{\mathrm{A,wall,bottom}} = 0$. Finally, Fluid A is made the viscoelastic component and Fluid B is made the Newtonian component.

τ_P	Wi_{global}	Wi_{local}
1000	0.005	0.6
2000	0.010	1.2
3000	0.015	1.8
4000	0.020	2.4
5000	0.025	3.0

We now investigate various aspects of the non-Newtonian contact line.

(a) Shape of interface

In this section the shape of the interface for different relaxation times of the polymer is studied. Here, we study both the receding and the advancing contact lines. All measurements are made once the simulation has reached steady state. Steady state is ensured by checking the shape of the interface at 2 different times and checking for their superposition. In addition, the receding and advancing contact line velocity is monitored and checked for steady state. Once steady state is ensured, the x-coordinate of the contact line at the bottom wall are all coincided to a single point and their shape at different heights are compared. This is shown in Figure (4.24). The following observations are made:

- It seen that for the receding interface the normalized interface profiles start to deviate from about $\frac{y}{H} \approx 0.5$ and upwards . Whereas the deviations for the advancing contact line are more evident from $\frac{y}{H} \approx 0.2$ and upwards.
- With respect to the final steady state position of the receding contact line, we see that the Newtonian contact line has receded the most. As the Wi increases the displacement of the receding contact line decreases. However, for the case of the advancing contact lines it is seen that the the Newtonian contact line has advanced the most. Further, for a higher Wi the displacement of the advancing contact line is lower.

Further, the shape of the interface can also be characterized by the local slope of the interface for different Wi. This is shown in Figure (4.25). From Figure (4.25) the following observations can be made:

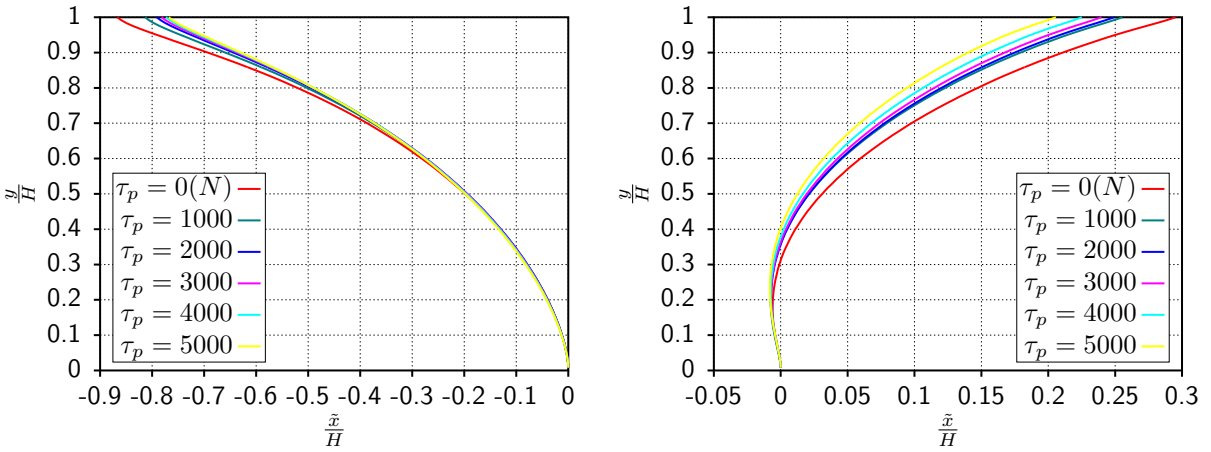

(a) RCL, $Ca = 5.25 \times 10^{-3}$ (b) ACL, $Ca = 5.25 \times 10^{-3}$

Figure 4.24: The interfaces corresponding to the (a) receding and (b) advancing contact lines are plotted for different $\tau_P.\tau_P = 0$ case corresponds to the case where both Fluid A and Fluid B are Newtonian. In the x-axis the normalized x coordinate (normalized by the height of the channel H) is plotted where the positions of the contact line at the bottom wall are assembled at a single point, for the sake of comparison. Similarly, the y position of the interface is normalized by the height H between the walls. The above plots can be reproduced using the test `R238_NON_NEWTONIAN_COUETTE_WETTING_MC` with the help of the gnuplot script `interface_plot.gnu`. The simulations for different τ_p is handled by the script `r238.sh` and is registered in gitlab as `ISSUE #182`. The plots can be found in the folder `final_plots`.

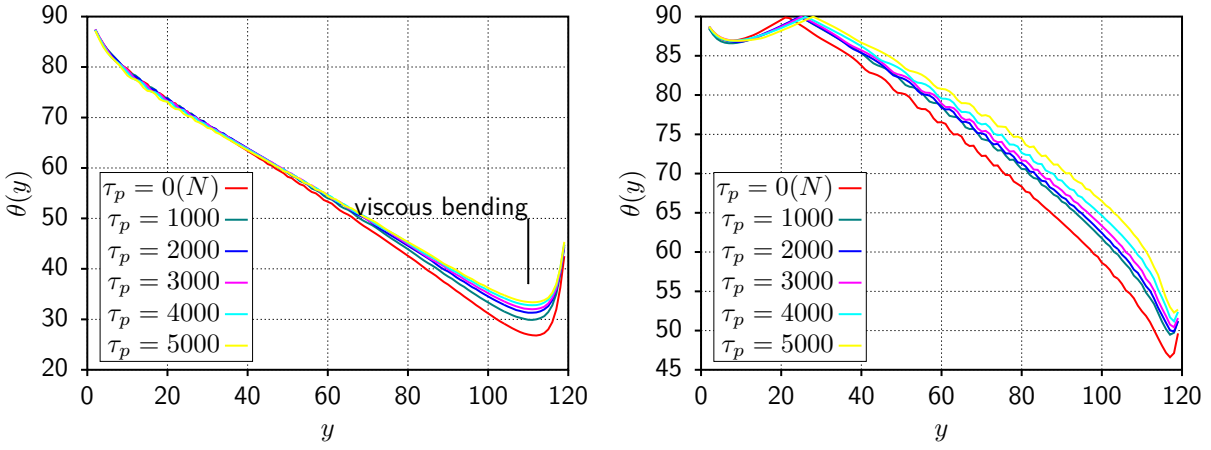

(a) RCL, $Ca = 5.25 \times 10^{-3}$ (b) ACL, $Ca = 5.25 \times 10^{-3}$

Figure 4.25: The local slope of the interface for (a) receding contact line, (b) advancing contact line. The above plots can be reproduced using the test `R238_NON_NEWTONIAN_COUETTE_WETTING_MC` with the help of the gnuplot script `interface_slope_compare.gnu`. The simulations for different τ_p is handled by the script `r238.sh` and is registered in gitlab as `ISSUE #182`. The plots can be found in the folder `final_plots`.

- **Receding contact line**: We observe the viscous bending of the interface as the interface approaches the wall near $y = 120$. The bending is highest for Wi and as the Wi is increased we observe that the bending is less pronounced.
- **Advancing contact line**: Just as in the case the receding contact line the viscous bending is observed for the case of the advancing contact line, see Figure (4.25b). However, the onset of the bending is much closer to the wall rather than the earlier onset observed in the receding contact line. In addition, interestingly, it is similar to the receding contact line in the sense that the bending is most pronounced

for the case of $Wi = 0$ and the bending starts to disappear for the case of higher Wi. For the case of the highest Wi we observe negligible bending.

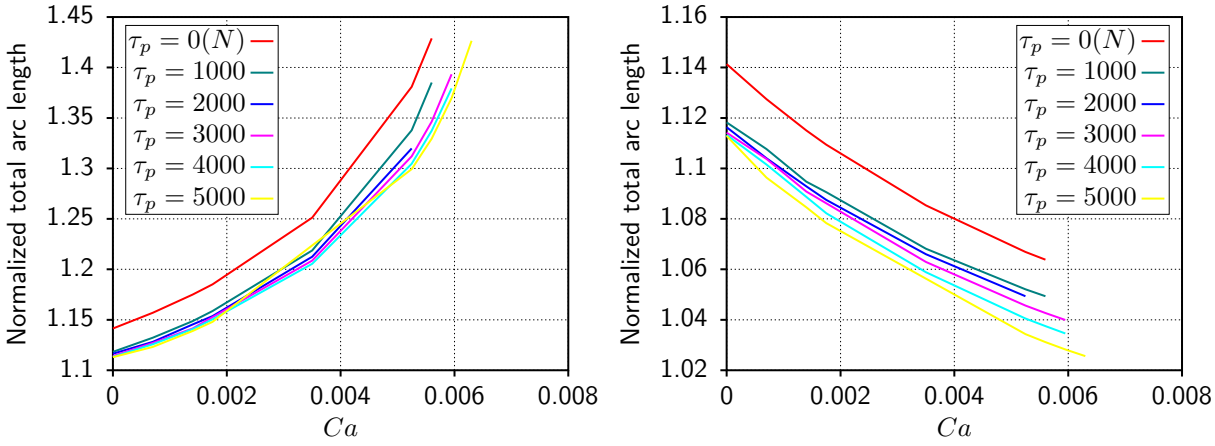

(a) RCL (b) ACL

Figure 4.26: The normalized total arc length of the interface for the (a) receding and the (b) advancing contact line is plotted. The total arc length is normalized with the height of the channel H. The total arc length is calculated by summing the discrete arc lengths $ds_i = \sqrt{dx_i^2 + dy_i^2}$ for $i = 1, \cdots, 120$.

In the above analysis, a comparison at a single Ca was carried out. However, it is interesting to see what happens for a range of Ca. For this, we compare the total arc length of the interface as a function of the Ca. From the above analysis it seems to suggest that the viscous bending of the interface and the displacement of the interface from it's initial position is somehow minimized for higher Wi. Therefore, it is interesting to compare the total arc length as a function of the Ca for the interfaces corresponding to the receding and advancing contact line. This comparison is shown in Figure (4.26). The following observations can be made:

- **Receding contact line**: From Figure (4.26a), for the case of the receding contact line it is seen that the differences between the total arc lengths between different Wi is not observable. In addition, it is seen that at $Ca = 0$ the arc lengths are different. This is not expected, since at $Ca = 0$ τ_P is not a parameter. However, it is known that LB method is susceptible to artifacts like spurious currents which drive velocity fields leading to generation of stresses even at $Ca = 0$. This departure of the total interface length is possibly due to these spurious currents.
- **Advancing contact line**: From Figure (4.26b), similar to the case of receding contact lines, the arc lengths do not start from the same value at $Ca = 0$. However, the differences between the arc lengths become more evident at higher Ca. For the case of higher Ca it is clear that the interface length is smallest for the case of the highest Wi.

Therefore, in this section the shape of the interface for the non-Newtonian contact lines was investigated for a range of polymer relaxation times τ_P. It could be concluded that for the range of Wi simulated here, significant effects were seen at the advancing interface, whereas, at the receding interface the effect were not as pronounced. To arrive at this conclusion, we investigated the steady state position of the interface for a particular Ca, the slope of the interface θ as a function of y, and, finally, we also compare the total interface length as a function of the Ca.

It is instructive to measure the polymeric shear ($\mathcal{S}$) and normal stress ($\mathcal{N}$) components near the contact line to see if the observations of this section can be explained.

(b) Polymeric shear stress and Normal stresses

The polymeric shear stress $\mathcal{S}$(x,y) or $\sigma_{P,xy}$ is measured at the fluid node next to the wall, i.e. $y = 120$. Similarly, the first normal stress difference $\mathcal{N}$ or $\sigma_{P,xx} - \sigma_{P,yy}$ is measured at the fluid node next to the wall. We measure both $\mathcal{N}$(x) and $\mathcal{S}$(x) for a $Ca = 5.25 \times 10^{-3}$. The results are plotted in Figure (4.27). We observe the following from Figure (4.27) for the polymeric shear stresses $\mathcal{S}$(x,y=120):

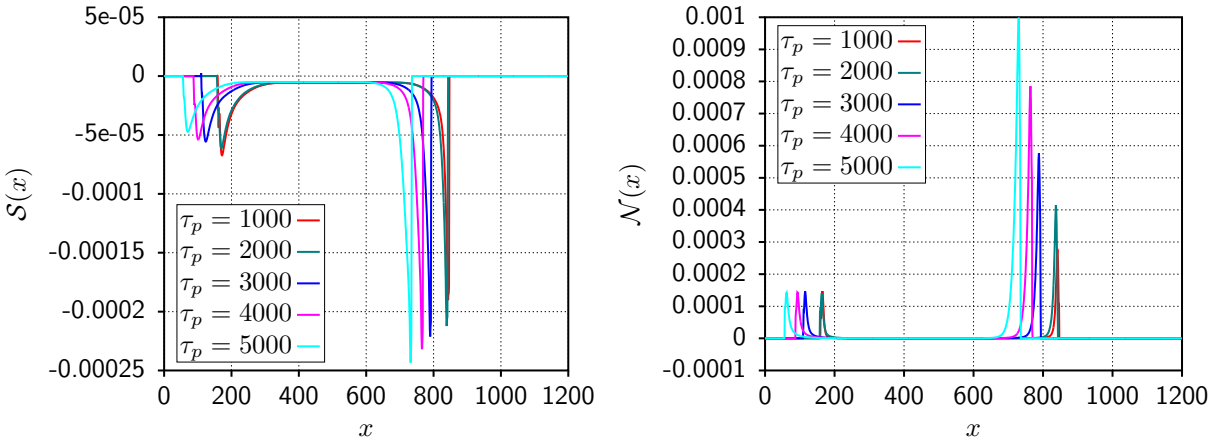

(a) $\mathcal{S}(x)$ at y=120, $Ca = 5.25 \times 10^{-3}$

(b) $\mathcal{N}(x)$ at y=120, $Ca = 5.25 \times 10^{-3}$

Figure 4.27: The first normal stress $\mathcal{N}(x, y = 120)$ and the polymeric shear stress $\mathcal{S}(x, y = 120)$ is plotted for a $Ca = 5.25 \times 10^{-3}$. The above plots can be reproduced using the test R238_NON_NEWTONIAN_COUETTE_WETTING_MC with the help of the gnuplot script `normal_stress_plot.gnu` and `shear_stress_plot.gnu`. The simulations for different τ_p is handled by the script `r238.sh` and is registered in gitlab as `ISSUE #182`. The plots can be found in the folder `final_plots`.

- **Receding Contact Line**:
  - The magnitude of $\mathcal{S}$ is 0 in the region corresponding to Fluid B (Figure (4.23)). Inside the viscoelastic region the shear stresses are maximum close to the contact line and then decrease and finally plateau. This implies that the non-Newtonian effects are localized to regions close to the contact line. This can be rationalized, since that is the location where the shear rates are largest.
  - From Figure (4.27a) the magnitude of the polymeric shear stresses are lower for higher Wi. This could explain why the steady state displacement of the receding contact line decreased as Wi was increased, see Figure (4.24a). Since, the polymeric shear stresses directly affect the polymeric viscosity η_P a higher η_P would correspond to a higher viscosity and therefore a higher entrainment.
- **Advancing Contact Line**:
  - Interestingly, for the advancing contact line we see that the gradients of the polymeric shear stresses are sharper in comparison with the receding contact line. In addition, the magnitudes are also higher. Therefore, the advancing contact lines are characterized by larger and steeper polymeric shear stress profiles.
  - The second interesting observation is regarding the trend of shear stress profile. It can be seen that the magnitude of the shear stresses increases with increase in Wi. This is opposite to what was observed at the receding contact line.

Now we look at the $\mathcal{N}(x, y = 120)$:

- **Receding contact line**:
  - From Figure (4.27b), surprisingly, it can be seen that at the receding interface the normal stresses do not vary in magnitude with an increase in the Wi.
- **Advancing contact line**:
  - For the advancing contact line we see that the magnitude of normal stresses are larger for higher Wi.

Therefore, from the above observations, we see that at the advancing contact line the magnitude of shear stresses and the normal stresses are both high. In addition, the magnitude of both the stresses increase with

an increase in the Wi. However, for the case of the receding contact line, a trend in the magnitude of the shear stresses is seen, where the magnitude of the shear stresses decreases with an increase in the Wi. However, surprisingly, the magnitude of the normal stresses do not alter for increasing Wi.

These observations can be used to make a hypothesis. If the polymer in the viscoelastic fluid is replaced by a Newtonian fluid the polymeric shear stresses and the normal stresses can be replaced with the hydrodynamic stresses. This leads to a larger displacement of the contact line, as seen in Figure (4.24a). However, increasing the Wi leads to a decrease in the magnitude of the polymeric shear stresses which seem to exert a force in the negative x direction on the contact line, which stops it from being entrained. This seems to suggest that the polymeric shear stresses have the effect of an additional viscosity added to a Newtonian solvent.

Let us apply the hypothesis developed in the previous paragraph and apply it to the case of the advancing contact line. A higher magnitude of polymeric shear stresses is observed for higher Wi. In addition, the normal stresses are also higher for higher Wi. From Figure (4.24b), we observe that the interface advances the least for the highest Wi. Also, from Figure (4.25b) we see that the viscous bending is highest for the Newtonian case and this bending reduces drastically on increasing the Wi. From the previous paragraph we hypothesized that the polymeric shear stress is responsible for the entrainment of the fluid through an "effective" viscosity. If the same hypothesis is applied to this particular case we end up with the conclusion that the entrainment should be highest for the case of the highest polymeric shear stress which happens to be for the highest Wi. We see that in fact the interface is "pulled" back for the case of the highest Wi. However, the involvement of normal stresses on the curvature of interface can only be hypothesized and this requires a detailed analysis.

To conclude this section we analyze the behavior of the normal and shear stresses with respect to the analytical predictions of the *Oldroyd-B* model. According to the *Oldroyd-B* model (Equation (4.15) and Equation (4.16) in the limit of $L^2 \to \infty$) the expressions for the normal stress $\mathcal{N}$ and the shear stress $\mathcal{S}$ is given by:

$$\mathcal{N} = 2\eta_P \tau_P \dot{\gamma}^2, \tag{4.51}$$

$$\mathcal{S} = \frac{\eta_P}{\tau_P} \dot{\gamma} \tau_P, \tag{4.52}$$

and from the above equations we can manipulate to get the following relation between $\mathcal{S}$ and $\mathcal{N}$ [2]:

$$\frac{\mathcal{N}}{2\mathcal{S}^2} = \frac{\tau_P}{\eta_P}. \tag{4.53}$$

Equation (4.53) is plotted for the shear and normal stress signals for $Ca = 5.25 \times 10^{-3}$ and different polymer relaxation times τ_P. This is shown in Figure (4.28). From figure we see that the *Oldroyd-B* definition of the polymer is only obeyed away from the contact line for different polymer relaxation times. However, close to the contact lines the ratio $\frac{\eta_P}{\tau_P}\left(\frac{\mathcal{N}}{2\mathcal{S}^2}\right)$ becomes negative as well. The reason for this might be due to the accumulation of errors in the numerical scheme used for the solving conformation tensor dynamics of the FENE-P polymer [63]. Similarly, the normalized normal stress is plotted for different relaxation times in Figure (4.29). This is a direct indication of the square of the shear rate $\dot{\gamma}$. In this figure we see that the peaks at the receding contact decrease for increasing relaxation time, and, at the advancing contact line the peaks show a constant value except for the case of $\tau_P = 1000$. But drawing conclusions from this plot might not be accurate, since from the previous analysis we observed that the *Oldroyd-B* assumption might not hold near the contact lines.

4.2.4 Critical wetting

In this section we comment on the dependence of the Ca_{cr} on Wi. We remind the reader that in the case of symmetric wetting we observed negligible changes in the Ca_{cr} as a function of the Wi. Hence, we decided to adopt the asymmetric wetting case to ensure that the critical wetting happens at the receding contact line for the viscoelastic fluid.

For asymmetric wetting case we observed changes in the Ca_{cr} as Wi was varied. However, the changes were very weak. Ca_{cr} varied from a value of 5.25×10^{-3} to 7×10^{-3} for the Wi_{global} varying from 0.005 to

[2] We see that an additional term $\frac{\eta_P}{\tau_P}$ is multiplied to both $\mathcal{N}$ and $\mathcal{S}$. This is because of the way the polymeric feedback stress is introduced into the Navier Stokes equation (Equation (3.45)). The entire term $\frac{\eta_P}{\tau_P}\underline{\underline{\boldsymbol{\sigma}}}_P$ is considered as the feedback stress.

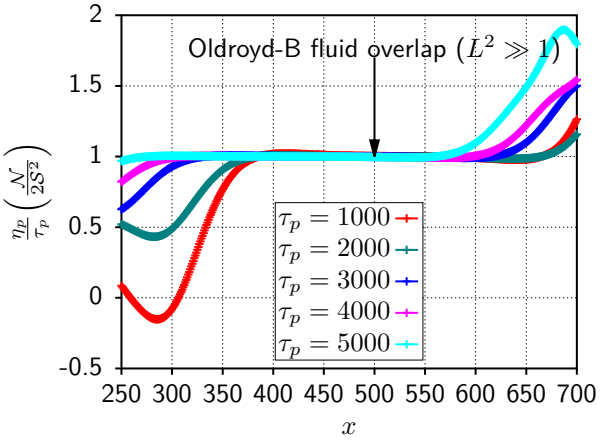

Figure 4.28: The quantity $\frac{\eta_P}{\tau_P}\left(\frac{\mathcal{N}}{2\mathcal{S}^2}\right)$ is plotted for $Ca = 5.25 \times 10^{-3}$ and different polymer relaxation times τ_P. According to Equation (4.53) the ratio is 1.0 for the case of an *Oldroyd-B* fluid. The quantity represented by the y-axis blows up close to the contact lines, and hence, is not plotted here.

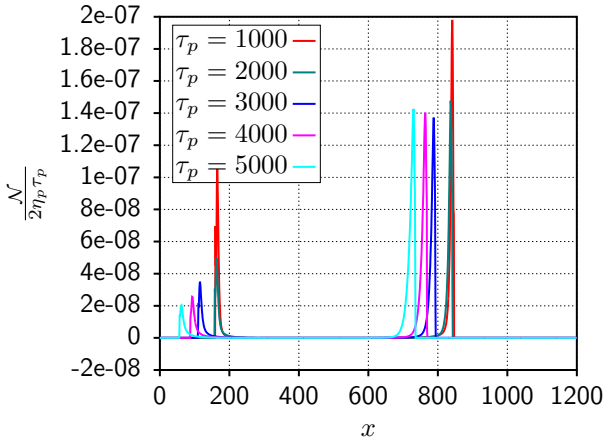

Figure 4.29: Normalized normal stress: $\frac{\mathcal{N}}{2\eta_p\tau_p}$ profile for $Ca = 5.25 \times 10^{-3}$

0.025.

Therefore, we can conclude that the critical wetting is delayed by increasing the Wi, or in other words, the polymer relaxation time τ_P.

4.2.5 Finite size effects

In this final section, we analyze some aspects related to the finite size effects. In the previous section, all the numerical simulations were done using a channel length $L_x = 1200$. However, it is interesting to observe the influence of length of the channel on the shape of the interface, as well as on the shear and normal stresses. Therefore, in this section the channel length is increased to $L_x = 2400$, where the half of the grid points are allocated to the viscoelastic component and the other half to the Newtonian component, and polymer relaxation time $\tau_P = 5000$ and the maximum extensible length square $L^2 = 10^4$. Firstly, the influence of channel length on the shape of the interface is investigated. The results for the receding and the advancing interface is shown in Figure (4.30). It is seen from Figure (4.30a) that for the receding interface the steady state displacement of the contact line is higher for the larger channel $L_x = 2400$. In addition, it is seen that the Newtonian contact lines (N/N in Figure (4.30a)) recede farther back when compared to the viscoelastic case (N/NN). However, qualitatively they are still similar to the observation in Figure (4.24a). Further, the

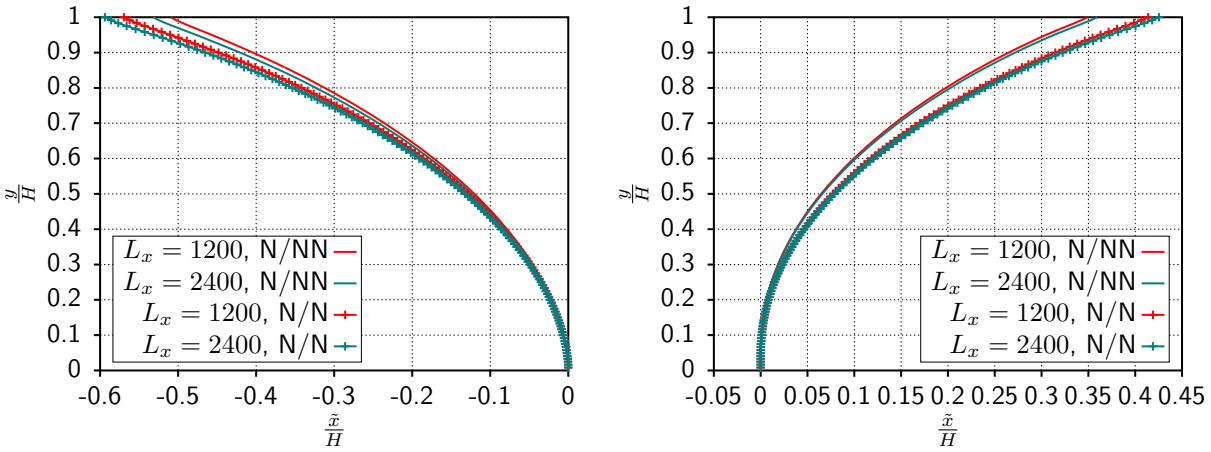

(a) RCL,$Ca = 1.75 \times 10^{-3}$, $\tau_p = 5000,\ L^2 = 10^4$ (b) ACL,$Ca = 1.75 \times 10^{-3}$, $\tau_p = 5000,\ L^2 = 10^4$

Figure 4.30: The interface corresponding to the (a) receding and the (b) advancing contact line is plotted for $L_x = 2400$, $\tau_P = 5000$, $L^2 = 10^4$, and compared against the case of $L_x = 1200$. Here, the N/N corresponds to the case where both Fluid A and Fluid B are Newtonian, and, N/NN corresponds to the case where Fluid A is a viscoelastic component, see Figure (4.23).

slope of the interface is compared as a function of distance from the wall is plotted in Figure (4.31). It is seen that the viscous bending close to the wall for the Newtonian contact line (N/N) for $L_x = 2400$ is more in comparison with $L_x = 1200$. Similarly, the viscous bending in non-Newtonian component (N/NN) for $L_x = 2400$ is more in comparison with $L_x = 1200$. However, the trends previously seen are still retained with minor changes. For the case of the advancing interface Figure (4.24b) a similar trend as seen for the case

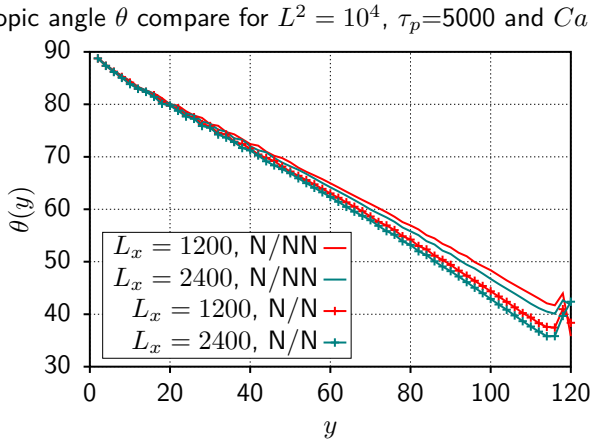

Figure 4.31: The local slope θ at different y positions for the case of $Ca = 1.75 \times 10^{-3}$, $\tau_p = 5000,\ L^2 = 10^4$ is plotted. Here, the N/N corresponds to the case where both Fluid A and Fluid B are Newtonian, and, N/NN corresponds to the case where Fluid A is a viscoelastic component, see Figure (4.23).

of the receding interface is observed. The differences in the position of the contact line are not pronounced when compared to the case of $L_x = 1200$.

Finally, we also check the influence of finite size on the normal and polymeric shear stresses. This is shown in Figure (4.32a). Firstly, it can be seen that the differences in $\mathcal{S}$ and $\mathcal{N}$ for the case of $L_x = 1200$ and $L_x = 2400$ are negligible at the receding contact line. However, at the advancing contact line the magnitude of the $\mathcal{S}$ and $\mathcal{N}$ slightly decrease with the increased channel length.

However, surprisingly, we see that the critical wetting occurs at a much smaller Ca when the size L_x is increased. The case of $L_x = 3600$ was also attempted, however, the $Ca = 1.75 \times 10^{-3}$ had already exceeded the Ca_{cr} and wetting failure had occurred. The reason for this might be the interacting flow

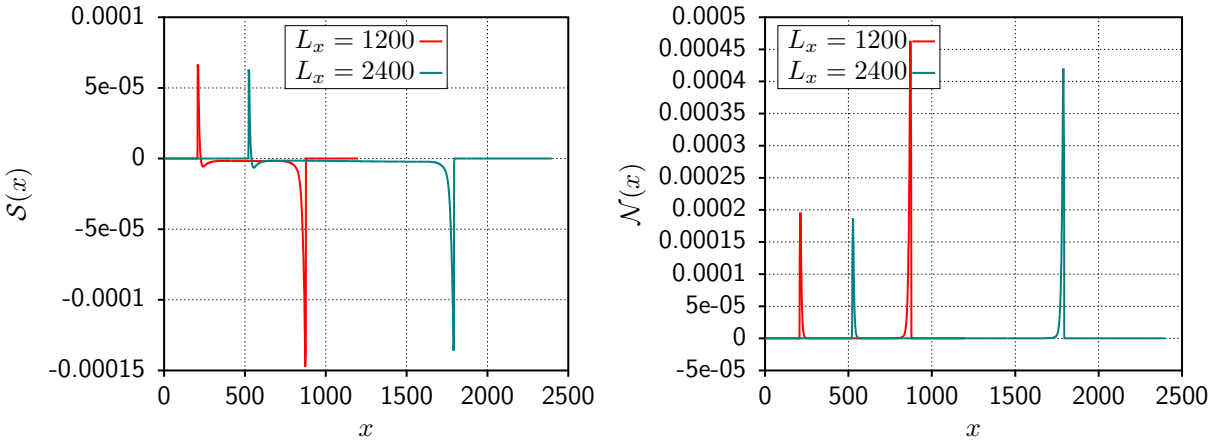

(a) RCL,$Ca = 1.75 \times 10^{-3}$, $\tau_p = 5000,\ L^2 = 10^4$

(b) RCL,$Ca = 1.75 \times 10^{-3}$, $\tau_p = 5000,\ L^2 = 10^4$

Figure 4.32: In this figure the polymeric shear stress $\mathcal{S}$ and the first normal stress difference $\mathcal{N}$ for $\tau_P = 5000$ is plotted for the case of $L_x = 1200$ and $L_x = 2400$.

features present in the channel and is accounted for as hydrodynamic interactions. A workaround to avoid the interference of the finite size effects on the measurements made in the system is to implement a special boundary condition called the rotating boundary condition [28, 60]. However, the rotating boundary conditions has been implemented for the case of opposite wettability and without polymers. The implementation for the case of arbitrary wetting angles with the addition of polymers is non-trivial and requires additional work.

We conclude the results and findings of the non-Newtonian contact lines in next chapter.

Chapter 5

Conclusion and Outlook

In this chapter we conclude by summarizing the main findings in this thesis and also discuss some open questions.

In this thesis we discussed the moving contact line problem for the case of non-Newtonian fluids. In particular, we investigated the effects of viscoelasticity on contact line motion. In order to carry out this investigation we adopted the Couette flow geometry, involving wetting of two fluids, Fluid 1 and Fluid 2, sandwiched between two walls, top and bottom, and separated by an interface. Our findings are as follows:

- We started our investigation by looking at symmetrical wetting of Fluid 1 and Fluid 2, at the top and bottom walls. We observed that there were differences in the shape of the interface as the viscoelasticity of Fluid 1 was increased. However, these differences were weak. Further, the influence of Weissenberg number (Wi) on the critical wetting behavior was also negligible. The reason for this negligible influence of viscoelasticity on the critical wetting behavior of the contact line is because the Newtonian fluid reaches critical wetting before the viscoelastic fluid. Hence, the effects of viscoelasticity are not perceivable.

- To clarify the effects of viscoelasticity on the contact line we introduced an asymmetric wetting condition. We imposed a neutral microscopic wetting angle ($\theta_{m,bottom} = 90$) at the bottom wall, and maintained a smaller wetting angle at the top wall ($\theta_{m,top} \approx 43^o$). This ensured that the critical wetting behavior at the receding contact line is primarily due to the viscoelastic fluid, instead of the Newtonian fluid.

- For the case of asymmetric wetting we studied (a) shape of the interface and (b) the polymeric shear stress ($\mathcal{S}$) and the first normal stress difference ($\mathcal{N}$) near the contact line. For the **shape of the interface**, we observed the following:

  - The displacement of the receding contact line decreased with increasing Wi. Further, we saw that the receding contact line for the Newtonian fluid was displaced the farthest. A similar trend was observed for the advancing contact line.
  - We consistently observed that the viscous bending near the wall decreased with increasing Wi. This was observed for both the receding contact line, and advancing contact line. This seems to suggest that the non-Newtonian effects reduce the effective friction induced by a moving contact line. However, this raises the question of whether shear thinning is responsible for such a behavior? This is currently not addressed in this thesis and is part of an ongoing work.
  - Finally, we also measured the total length of the interface for the receding and advancing contact lines. We observed that the interface length is more sensitive to Wi for the advancing contact line. An increase in the Wi led to a decrease in the length of the interface. However, the variation in length of the interface was negligible for the receding contact line when we increased the Wi. Interestingly, we also found that the interface lengths at $Ca = 0$ did not coincide. This was unexpected since the addition of polymer should not have had any influence on the interface at $Ca = 0$, because the polymeric stresses are all zero. This might be an artifact of the LB method, and has to be probed further.

  For the **polymeric shear stress and the normal stress** we observe the following:

  - The viscoelastic effects were confined to a region close to the contact line. This can be rationalized by considering that the regions of highest shear stresses are the ones closest to the contact line. Therefore, non-Newtonian effects are observed only close to the contact line.
  - Interesting trends appeared for the polymeric shear stress and the normal stress close to the contact line. For the receding contact line we observed that the magnitude of the polymeric shear stress $\mathcal{S}$ decreased with increasing Wi, whereas, at the advancing contact line the magnitude of the polymeric shear stress increased with increasing Wi. On the contrary, we observed that the normal stress $\mathcal{N}$ for the receding contact line did not vary appreciably with increasing Wi. However, at the advancing contact line the normal stresses increased with an increase in Wi.
  - Finally, we compared the ratio $\frac{\eta_P}{\tau_P}\frac{\mathcal{N}}{2\mathcal{S}^2}$ in the *Oldroyd-B* limit, at distances close to and far away from the contact line. We found that the curves for various polymer relaxation times τ_P collapsed into a single curve, indicating that *Oldroyd-B* behavior is achieved only far away from the contact lines. Close to the contact lines the magnitude of the stresses for receding and the advancing contact lines show deviations from *Oldroyd-B* behavior.

- The dependence of the critical wetting behavior characterized by Ca_{cr} was investigated as a function of Weissenberg number Wi. We observed that increasing Wi delayed the onset of critical wetting. However, the changes in the Ca_{cr} was not appreciable. The Ca_{cr} varied from a value of 5.25×10^{-3} to 7×10^{-3} for the Wi_{global} varying from 0.005 to 0.025.

- Finally, we also investigated for any finite size effects and compared it to our previously obtained results. We observed that increasing the length of the channel L_x gave rise to an increase in the displacement of both the receding and advancing contact lines. We find this to be worrisome because in principle we are simulating a channel which is infinite in the x-direction (through the application of a periodic boundary condition). However, practically, the imposition of a periodic boundary condition on an insufficiently finite channel may give rise to hydrodynamic interactions between the flow fields present at the receding and advancing contact lines. On a positive note, the qualitative behaviors of the shear and normal stresses at different channel lengths are similar. Further, even the viscous bending at the receding contact line is qualitatively the same across varying channel lengths.

5.1 Open questions

At the end of this thesis we also present some open questions that require additional probing, and that require further probing. We list them here.

- We consistently observe that the interface shapes for varying polymer relaxation times Wi do not coincide at $Ca = 0$. This is unexpected since τ_P is not a parameter at $Ca = 0$.

- Influence of finite size effects are certainly worrisome if one is interested in investigating accurately the influence of viscoelasticity on the critical wetting behavior. One possible solution is to increase the size of the channel L_x until the features do not change appreciably. However, this also implies that the simulation requires more time to reach steady state. This makes the approach computationally expensive. Alternatively, one could adopt a boundary condition which uses the symmetry of the system to negate finite size effects and reduce computational time. However, this is not an easy exercise and requires further efforts.

Bibliography

[1] Cyril Duez, Christophe Ybert, Christophe Clanet, and Lydéric Bocquet. Making a splash with water repellency. *Nature physics*, 3(3):180–183, 2007.

[2] Jacco H. Snoeijer and Bruno Andreotti. Moving contact lines: Scales, regimes, and dynamical transitions. *Annual Review of Fluid Mechanics*, 45(1):269–292, 2013.

[3] L.D. Landau and B.G. Levich. Dragging of liquid by a plate. *Acta Physicochim. URSS*, 17:42–54, 1942.

[4] Kenneth J. Ruschak. Coating flows. *Annual Review of Fluid Mechanics*, 17(1):65–89, 1985.

[5] David Quéré. Fluid coating on a fiber. *Annual Review of Fluid Mechanics*, 31(1):347–384, 1999.

[6] K.G. Winkels. *Fast contact line motion: fundamentals and applications*. PhD thesis, Enschede, 2013.

[7] KG Winkels, IR Peters, F Evangelista, M Riepen, A Daerr, L Limat, and JH Snoeijer. Receding contact lines: From sliding drops to immersion lithography. *The European Physical Journal-Special Topics*, 192(1):195–205, 2011.

[8] Nathalie Fraysse and George M. Homsy. An experimental study of rivulet instabilities in centrifugal spin coating of viscous newtonian and non newtonian fluids. *Physics of Fluids*, 6(4):1491–1504, 1994.

[9] M.A. Spaid and G.M. Homsy. Viscoelastic free surface flows: spin coating and dynamic contact lines. *Journal of Non-Newtonian Fluid Mechanics*, 55(3):249 – 281, 1994.

[10] M. A. Spaid and G. M. Homsy. Stability of newtonian and viscoelastic dynamic contact lines. *Physics of Fluids*, 8(2):460–478, 1996.

[11] Y Wei, E Rame, L M Walker, and S Garoff. Dynamic wetting with viscous newtonian and non-newtonian fluids. *Journal of Physics: Condensed Matter*, 21(46):464126, 2009.

[12] G. K. Seevaratnam, Y. Suo, E. Ramé, L. M. Walker, and S. Garoff. Dynamic wetting of shear thinning fluids. *Physics of Fluids*, 19(1):012103, 2007.

[13] A. Boudaoud. Non-newtonian thin films with normal stresses: dynamics and spreading. *The European Physical Journal E*, 22(2):107–109, 2007.

[14] SALIMA RAFAÏ, DANIEL BONN, and AREZKI BOUDAOUD. Spreading of non-newtonian fluids on hydrophilic surfaces. *Journal of Fluid Mechanics*, 513:77–85, 2004.

[15] Denis Bartolo, Arezki Boudaoud, Grégoire Narcy, and Daniel Bonn. Dynamics of non-newtonian droplets. *Phys. Rev. Lett.*, 99:174502, Oct 2007.

[16] Chun Huh and LE Scriven. Hydrodynamic model of steady movement of a solid/liquid/fluid contact line. *Journal of Colloid and Interface Science*, 35(1):85–101, 1971.

[17] Elizabeth B. Dussan V. and Stephen H. Davis. On the motion of a fluid-fluid interface along a solid surface. *Journal of Fluid Mechanics*, 65(1):71–95, 1974.

[18] J.S. Rowlinson and B. Widom. *Molecular Theory of Capillarity*. Dover books on chemistry. Dover Publications, 2002.

[19] DAVID JACQMIN. Onset of wetting failure in liquid–liquid systems. *Journal of Fluid Mechanics*, 517:209–228, 2004.

[20] P. Yue and J. J. Feng. Can diffuse-interface models quantitatively describe moving contact lines? *The European Physical Journal Special Topics*, 197(1):37, 2011.

[21] TIEZHENG QIAN, XIAO-PING WANG, and PING SHENG. A variational approach to moving contact line hydrodynamics. *Journal of Fluid Mechanics*, 564:333–360, 2006.

[22] Daniel Bonn, Jens Eggers, Joseph Indekeu, Jacques Meunier, and Etienne Rolley. Wetting and spreading. *Reviews of modern physics*, 81(2):739, 2009.

[23] P. G. de Gennes. Wetting: statics and dynamics. *Rev. Mod. Phys.*, 57:827–863, Jul 1985.

[24] V E B Dussan. On the spreading of liquids on solid surfaces: Static and dynamic contact lines. *Annual Review of Fluid Mechanics*, 11(1):371–400, 1979.

[25] O. V. Voinov. Hydrodynamics of wetting. *Fluid Dynamics*, 11(5):714–721, 1976.

[26] LH Tanner. The spreading of silicone oil drops on horizontal surfaces. *Journal of Physics D: Applied Physics*, 12(9):1473, 1979.

[27] R. G. Cox. The dynamics of the spreading of liquids on a solid surface. part 1. viscous flow. *Journal of Fluid Mechanics*, 168:169–194, 1986.

[28] M. SBRAGAGLIA, K. SUGIYAMA, and L. BIFERALE. Wetting failure and contact line dynamics in a couette flow. *Journal of Fluid Mechanics*, 614:471–493, 2008.

[29] Alexander Oron, Stephen H. Davis, and S. George Bankoff. Long-scale evolution of thin liquid films. *Rev. Mod. Phys.*, 69:931–980, Jul 1997.

[30] David L. Morris, Lawrence Hannon, and Alejandro L. Garcia. Slip length in a dilute gas. *Phys. Rev. A*, 46:5279–5281, Oct 1992.

[31] F.A. Morrison. *Understanding Rheology*. Topics chemical engineering : A series of textbooks and monographs. Oxford University Press, 2001.

[32] M. Doi and S.F. Edwards. *The Theory of Polymer Dynamics*. International series of monographs on physics. Clarendon Press, 1988.

[33] R J Poole. The deborah and weissenberg numbers. pages 32–39, 2012.

[34] R.B. Bird, C.F. Curtiss, R.C. Armstrong, and O. Hassager. *Dynamics of Polymeric Liquids, Volume 2: Kinetic Theory*. Wiley, 1987.

[35] Ronald G Larson. *The structure and rheology of complex fluids*, volume 150. Oxford university press New York, 1999.

[36] D.V. Boger and K. Walters. *Rheological phenomena in focus*. Rheology series. Elsevier, 1993.

[37] R. J. Binnington and D. V. Boger. Constant viscosity elastic liquids. *Journal of Rheology*, 29(6):887–904, 1985.

[38] David F. James. Boger fluids. *Annual Review of Fluid Mechanics*, 41(1):129–142, 2009.

[39] K. Huang. *Statistical mechanics*. Wiley, 1987.

[40] Sauro Succi. The lattice boltzmann equation: for fluid dynamics and beyond, 2001.

[41] Sasidhar Kondaraju, Hassan Farhat, and Joon Sang Lee. Study of aggregational characteristics of emulsions on their rheological properties using the lattice boltzmann approach. *Soft Matter*, 8:1374–1384, 2012.

[42] Xiaoyi He and Li-Shi Luo. Theory of the lattice boltzmann method: From the boltzmann equation to the lattice boltzmann equation. *Phys. Rev. E*, 56:6811–6817, Dec 1997.

[43] S.Srivastava. *Lattice Boltzmann method for contact line dynamics*. PhD thesis, Eindhoven, 2014.

[44] Xiaowen Shan and Hudong Chen. Lattice boltzmann model for simulating flows with multiple phases and components. *Phys. Rev. E*, 47:1815–1819, Mar 1993.

[45] Xiaowen Shan and Hudong Chen. Lattice boltzmann model for simulating flows with multiple phases and components. *Phys. Rev. E*, 47:1815–1819, Mar 1993.

[46] Roberto Benzi, Mauro Sbragaglia, Sauro Succi, Massimo Bernaschi, and Sergio Chibbaro. Mesoscopic lattice boltzmann modeling of soft-glassy systems: theory and simulations. *The Journal of Chemical Physics*, 131(10):104903, 2009.

[47] Haibo Huang, Daniel T. Thorne, Marcel G. Schaap, and Michael C. Sukop. Proposed approximation for contact angles in shan-and-chen-type multicomponent multiphase lattice boltzmann models. *Phys. Rev. E*, 76:066701, Dec 2007.

[48] R.B. Bird and A.J. Giacomin. Polymer fluid dynamics: Continuum and molecular approaches. *Annual Review of Chemical and Biomolecular Engineering*, 7(1):479–507, 2016. PMID: 27276553.

[49] R.B. Bird, P.J. Dotson, and N.L. Johnson. Polymer solution rheology based on a finitely extensible bead—spring chain model. *Journal of Non-Newtonian Fluid Mechanics*, 7(2):213 – 235, 1980.

[50] R.B. Bird and O. Hassager. *Dynamics of Polymeric Liquids: Fluid mechanics*. Dynamics of Polymeric Liquids. Wiley, 1987.

[51] Anupam Gupta, Mauro Sbragaglia, and Andrea Scagliarini. Hybrid lattice boltzmann/finite difference simulations of viscoelastic multicomponent flows in confined geometries. *Journal of Computational Physics*, 291:177–197, 2015.

[52] Silvia Varagnolo, Daniele Filippi, Giampaolo Mistura, Matteo Pierno, and Mauro Sbragaglia. Stretching of viscoelastic drops in steady sliding. *Soft Matter*, 13:3116–3124, 2017.

[53] PENGTAO YUE, JAMES J. FENG, CHUN LIU, and JIE SHEN. Viscoelastic effects on drop deformation in steady shear. *Journal of Fluid Mechanics*, 540:427–437, 2005.

[54] PENGTAO YUE, JAMES J. FENG, CHUN LIU, and JIE SHEN. A diffuse-interface method for simulating two-phase flows of complex fluids. *Journal of Fluid Mechanics*, 515:293–317, 2004.

[55] Mario Minale, Sergio Caserta, and Stefano Guido. Microconfined shear deformation of a droplet in an equiviscous non-newtonian immiscible fluid: Experiments and modeling. *Langmuir*, 26(1):126–132, 2010. PMID: 20038166.

[56] G. I. Taylor. The viscosity of a fluid containing small drops of another fluid. *Proceedings of the Royal Society of London A: Mathematical, Physical and Engineering Sciences*, 138(834):41–48, 1932.

[57] M. Shapira and S. Haber. Low reynolds number motion of a droplet in shear flow including wall effects. *International Journal of Multiphase Flow*, 16(2):305 – 321, 1990.

[58] Mario Minale. Models for the deformation of a single ellipsoidal drop: a review. *Rheologica Acta*, 49(8):789–806, 2010.

[59] AJ Briant, AJ Wagner, and JM Yeomans. Lattice boltzmann simulations of contact line motion. i. liquid-gas systems. *Physical Review E*, 69(3):031602, 2004.

[60] AJ Briant and JM Yeomans. Lattice boltzmann simulations of contact line motion. ii. binary fluids. *Physical Review E*, 69(3):031603, 2004.

[61] Nicos S. Martys and Hudong Chen. Simulation of multicomponent fluids in complex three-dimensional geometries by the lattice boltzmann method. *Phys. Rev. E*, 53:743–750, Jan 1996.

[62] DAVID JACQMIN. Contact-line dynamics of a diffuse fluid interface. *Journal of Fluid Mechanics*, 402:57–88, 2000.

[63] T. Vaithianathan and Lance R. Collins. Numerical approach to simulating turbulent flow of a viscoelastic polymer solution. *Journal of Computational Physics*, 187(1):1 – 21, 2003.

List of Figures